People's Democratic Republic of Algeria

الجمهورية الجزائرية الديمقراطية الشعبية

Ministry of Higher Education and Scientific Research

وزارة التعليم العالي و البحث العلمي

BADJI MOKHTAR-ANNABA UNIVERSITY

جامعة باجي مختار- عنابة

Faculty of Sciences

Department of Physics

Laboratory for the Study and Research of Condensed Matter

Thesis

Presented for the purpose of obtaining the diploma of

Doctorate

Option: Applied Physics and Engineering

Theme

Supercapacitors based on nanostructured materials

By

Mohammed AZZEDDINE

In front of the jury:

Farid GHELDANE	Professor	President	University BM Annaba
Mohammed GUERIOUNE	Professor	Thesis Supervisor	University BM Annaba
Ouanassa GUELLATI	Professor	Co-supervisor	University MCM Souk-Ahras
Mohamed Yacine DEBILI	Professor	Examiner	University BM Annaba
Hamid SATHA	Professor	Examiner	University 08 Mai Guelma

Academic Year 2024/2025

Acknowledgments

All praise and thanks are due to God, without whose blessings this work would not have been possible.

This thesis is the result of a collaborative research effort between the LEREC Laboratory at Badji Mokhtar-Annaba University and the CES Laboratory at Namur University.

My deepest gratitude goes to my thesis supervisor, Professor Mohamed GUERIOUNE, from Badji Mokhtar-Annaba University. His unwavering support, insightful advice, and expertise have been crucial throughout the course of my research. Without his guidance, this thesis would not have reached its completion.

I express my respect, profound gratitude, and sincere thanks to my thesis co-supervisor, Miss Ouanassa GUELLATI, Professor at Mohamed Cherif Messaadia University–Souk Ahras, who graciously took on the role of supervising this thesis, guiding me through each stage of the process with unwavering patience and understanding.

I am immensely grateful to Professor Farid GHELDANE from Université Badji Mokhtar, Annaba for kindly accepting the role of jury president. I am also profoundly thankful to Professor Mohamed Yacine DEBILI from Université Badji Mokhtar, Annaba and Professor Hamid SATHA from University 08 Mai Guelma for honoring me with their time and expertise in examining this work.

My appreciation also goes to the faculty and staff in the Department of Physics, Badji Mokhtar-Annaba University, whose resources and assistance have been invaluable. Special thanks also go to the faculty and staff at the LEREC Laboratory for providing an excellent research environment and the necessary resources to conduct this study.

My sincerest thanks go to the entire Erasmus+ team, especially to Mr. Henrich BRUNKE, the Erasmus+ program coordinator, for his steadfast support and invaluable assistance throughout my time abroad.

I am profoundly grateful to Professor Zineb MEKHALIF, Director of the CES laboratory, and Professor Joseph DELHALLE. Their welcoming environment, invaluable advice, and unwavering support throughout my stay were crucial to my research.

Furthermore, I'd like to acknowledge Mr. Corry CHARLIER for generously imparting his critical knowledge and practical skills in scanning electron microscopy (SEM) and transmission electron microscopy (TEM). My gratitude also goes to Dr. Nikolay TUMANOV for the excellent training provided in X-ray Diffraction (XRD) techniques. My gratitude is also extended to Dr. Sebastien VIVEGNIS for his guidance in the practical use of the XPS machine.

I want to express my appreciation to my fellow researchers and colleagues: Dr. Aicha HARAT, Dr. Arvind Kumar Bhakta, Dr. Amir BOSTILA, and Nassim CHETOUH.

On a more personal note, I would like to thank my dear mother and father, my sisters, and my friends for their unwavering support, patience, and understanding throughout this long and challenging process. Your belief in me has been my constant source of strength.

Finally, I wish to acknowledge all the individuals and institutions who contributed, directly or indirectly, to the success of this work. This thesis is as much yours as it is mine.

Thank you all

Abstract:

Energy conversion and storage have long been critical areas of research aimed at advancing and scaling sustainable, clean energy sources along with their associated technologies. Over the past two decades, supercapacitors have emerged as one of the most extensively researched fields within electrochemical science. Notably, significant efforts have concentrated on the rapid advancement of diverse electrode materials, resulting in remarkable progress and innovation.

The primary aim of this experimental study is to develop high-performance electrodes based on Ni/Mn nanohybrid through a straightforward and validated hydrothermal synthesis method. This approach is cost-effective and easy to implement under carefully optimized thermodynamic conditions, including precursor selection and growth temperature, while also focusing on their nanostructure.

We conducted a comprehensive analysis of the structural, textural, morphological, spectroscopic, and optical properties using various techniques, including X-ray diffraction (XRD), Fourier-transform infrared spectroscopy (FTIR), Raman spectroscopy, Brunauer-Emmett-Teller (BET) surface area analysis, field emission scanning electron microscopy (FESEM), ultraviolet-visible spectroscopy (UV-Vis), and X-ray photoelectron spectroscopy (XPS). Additionally, we performed a series of electrochemical assessments through cyclic voltammetry (CV), charge/discharge (CD) tests, and electrochemical impedance spectroscopy (EIS). The results demonstrate that the $2Ni(HCO3)_2/MnCO3$ nanohybrid achieved an impressive specific capacitance of 2777 F/g at a scan rate of 5 mV/s (equivalent to 320 mAh/g at 1 A/g), showcasing exceptional rate capability. This outstanding electrochemical performance is attributed to the optimized Ni/Mn composition and the unique nanostructured architecture with intercalated ions. These characteristics highlight the significant potential of this novel nanohybrid for providing both high energy density and high-power density in future energy storage applications, particularly in the development of supercapacitors.

Key words: Energy storage, Supercapacitor, nanomaterials, Ni/Mn nanohybrids, Electrochemical properties.

الملخص:

لطالما كان تحويل الطاقة وتخزينها من المجالات البحثية الحرجة التي تهدف إلى تعزيز وتطوير مصادر الطاقة المستدامة والنظيفة جنبًا إلى جنب مع التقنيات المرتبطة بها .على مدى العقدين الماضيين، ظهرت المكثفات الفائقة كواحدة من أكثر المجالات بحثًا في علوم الكيمياء الكهربية .ومن الجدير بالذكر أن جهودًا كبيرة قد تركزت على التقدم السريع لمواد الأقطاب المتنوعة، مما أدى إلى تحقيق تقدم ملحوظ وابتكار .الهدف الرئيسي من هذه الدراسة التجريبية هو تطوير أقطاب عالية الأداء من خلال طريقة تخليق هيدروحراري بسيطة وموثوقة .هذه الطريقة فعالة من حيث التكلفة Ni/Mn تعتمد على نانو هجين وسهلة التنفيذ تحت ظروف حرارية ديناميكية محسّنة بعناية، بما في ذلك اختيار المكونات ودرجة حرارة النمو، مع التركيز أيضًا على هيكلها النانوي .قمنا بإجراء تحليل شامل للخصائص الهيكلية والنسيجية والشكلية والطبقية والبصرية باستخدام (FTIR)، طيف الأشعة تحت الحمراء بواسطة تحويل فورييه ،(XRD) تقنيات متنوعة، بما في ذلك حيود الأشعة السينية مجهر المسح الإلكتروني بتأثير المجال ،(BET) طيف رامان، تحليل مساحة السطح بواسطة برونواير-إيميت-تيلر ،بالإضافة إلى ذلك .(XPS) وطيف الإلكترونات السينية ،(UV-Vis) طيف الأشعة فوق البنفسجية-المرئية ،(FESEM) ،(CD) واختبارات الشحن/التفريغ ،(CV) قمنا بإجراء سلسلة من التقييمات الكهروكيميائية من خلال الفولتامية الدورية حقق سعة مميزة Ni(HCO3)2/MnCO3تُظهر النتائج أن النانو هجين 2 .(EIS) الكهروكيميائي impedence وطيف مما يعكس قدرة استثنائية على ،(A/g عند 1 mAh/g ما يعادل 320) mV/s عند معدل مسح قدره 5 F/g قدرها 2777 والهيكل الفريد النانوي مع أيونات Ni/Mn التفاعل السريع .يُعزى هذا الأداء الكهروكيميائي الرائع إلى التركيب المحسن من متداخلة .هذه الخصائص تبرز الإمكانات الكبيرة لهذا النانو هجين الجديد في توفير كثافة طاقة عالية وكثافة طاقة عالية في تطبيقات تخزين الطاقة المستقبلية، خاصة في تطوير المكثفات الفائقة.

الكلمات المفتاحية :تخزين الطاقة, المكثف الفائق, المواد النانوية, هجائن النانو من النيكل/المنغنيز, الخصائص الكهروكيميائية

Résumé :

La conversion et le stockage de l'énergie ont longtemps été des domaines de recherche critiques visant à faire avancer et à développer des sources d'énergie durables et propres, ainsi que les technologies qui leur sont associées. Au cours des deux dernières décennies, les supercondensateurs sont devenus l'un des domaines les plus largement étudiés dans la science électrochimique. Notamment, des efforts considérables ont été concentrés sur l'avancement rapide de matériaux d'électrode divers, entraînant des progrès et des innovations remarquables.

L'objectif principal de cette étude expérimentale est de développer des électrodes haute performance basées sur un nanohybride Ni/Mn à l'aide d'une méthode de synthèse hydrothermale simple et validée. Cette approche est rentable et facile à mettre en œuvre dans des conditions thermodynamiques soigneusement optimisées, y compris le choix des précurseurs et la température de croissance, tout en se concentrant également sur leur nanostructure.

Nous avons réalisé une analyse complète des propriétés structurales, texturales, morphologiques, spectroscopiques et optiques en utilisant diverses techniques, notamment la diffraction des rayons X (XRD), la spectroscopie infrarouge à transformée de Fourier (FTIR), la spectroscopie Raman, l'analyse de surface par Brunauer-Emmett-Teller (BET), la microscopie électronique à balayage à émission de champ (FESEM), la spectroscopie ultraviolet-visible (UV-Vis) et la spectroscopie photoélectronique par rayons X (XPS). De plus, nous avons effectué une série d'évaluations électrochimiques par voltamétrie cyclique (CV), des tests de charge/décharge (CD) et de spectroscopie d'impédance électrochimique (EIS). Les résultats montrent que le nanohybride $2Ni(HCO3)_2/MnCO3$ a atteint une capacité spécifique impressionnante de 2777 F/g à un taux de balayage de 5 mV/s (équivalent à 320 mAh/g à 1 A/g), démontrant une capacité de taux exceptionnelle. Cette performance électrochimique exceptionnelle est attribuée à la composition optimisée de Ni/Mn et à l'architecture unique en nanostructure avec des ions intercalés. Ces caractéristiques soulignent le potentiel significatif de ce nouveau nanohybride pour fournir à la fois une haute densité d'énergie et une haute densité de puissance dans les futures applications de stockage d'énergie, en particulier dans le développement de supercondensateurs.

Mots clés : stockage d'énergie, supercondensateur, nanomatériaux, Nanohybrides de Ni/Mn, propriétés électrochimiques.

List of abbreviations

SC: Supercapacitor

IHP: Inner Helmholtz plane

OHP: Outer Helmholtz plane

IUPAC: International Union of Pure and Applied Chemistry

AC: Activated carbon

CNTs: Carbon nanotubes, SWCNTs single-walled, MWCNTs multi-walled

PANI: Polyaniline

PEDOT: Poly-(3,4-ethylenedioxythiophene)

SSA: specific surface area

PCs: Pseudocapacitors

HSCs: Hybrid supercapacitors

EDLCs: Electric double-layer capacitors

EES: Electric energy storage

CVD: Chemical Vapor Deposition

CB: carbon black

PVdF: polyvinylidene difluoride

NMP: 1-methyl-2-pyrrolidone

NiF: Nickel foam

XRD: X-ray Diffraction

FTIR: Fourier transform infrared spectroscopy

FE-SEM: high-resolution scanning electron microscopy

TEM: Transmission electron microscopy

BET: Brunauer, Emmett and Teller

BJH: Barret, Joyner and Halenda

UV-Vis: Ultraviolet-visible absorption spectroscopy

XPS: X-ray Photoelectron Spectroscopy

CV: cyclic voltammetry

GCD: galvanostatic charge discharge

EIS: Electrochemical Impedance Spectroscopy

Contents

General Introduction

In today's technology-dependent world, a constant energy supply is essential for the effective operation of electronic systems [1]. The escalating global energy demand, driven by factors such as population growth and economic development, coupled with the depletion of fossil fuels and the urgent need to address climate change, necessitates a transition to renewable energy sources. This shift requires robust energy storage systems to ensure a sustainable and resilient energy future [2]. Supercapacitors excel as energy storage devices due to their high-power density, rapid charge-discharge rates, safety, long cycle life, and environmental compatibility [3]. These attributes position them as promising alternatives to batteries for addressing growing energy demands and mitigating climate change. However, their relatively low energy density compared to batteries limits widespread application [4]. To enhance energy density, researchers have focused on developing electrode materials with increased specific capacitance [5].

A supercapacitor's energy density is directly correlated with both electrode capacitance and cell voltage. Consequently, nanostructured electrode materials have emerged as a promising strategy to improve capacitance by reducing ion diffusion distances and maximizing surface area [6]. These materials often exhibit superior capacitive performance and high-power density compared to their bulk counterparts [7]. Electrode morphology plays a critical role in supercapacitor performance. While traditional supercapacitors employ symmetrically configured activated carbon electrodes with capacitive energy storage, the use of composite electrodes can introduce faradaic contributions. To optimize performance, electrode materials require high surface area, electrical conductivity, and porosity. Consequently, nanomaterials with tailored pore structures and morphologies have been extensively investigated [8].

The manuscript is divided into three chapters:

Chapter one presents a comprehensive literature review on the fundamental principles of electrochemical energy storage, including an overview of diverse systems such as capacitors, batteries, and supercapacitors. The chapter then delves into supercapacitors, exploring their key components, electrode materials (a primary focus of this research), and classifications: capacitive, pseudocapacitive, and hybrid. It will also highlight the

diverse applications of supercapacitors before concluding with a discussion of various nanostructured materials synthesis methods used in the field.

Chapter two is dedicated to the experimental protocols followed in this study to synthesize Ni/Mn binary based nanohybrids using a simple, proven, easily implementable, and cost-effective hydrothermal method. This experimental work was successfully carried out at the LEREC Laboratory at the University of Badji-Mokhtar in Annaba. Subsequently, this chapter illustrates the various characterization techniques employed to identify the synthesized products from a structural, textural, and morphological standpoint. The quantitative and qualitative characterization techniques used include X-ray Diffraction (XRD), Fourier Transform Infrared Spectroscopy (FTIR), Raman Spectroscopy, High-Resolution Scanning Electron Microscopy (FE-SEM), Transmission Electron Microscopy (TEM), the BET method, Ultraviolet-Visible (UV-Vis) absorption spectroscopy, and X-ray Photoelectron Spectroscopy (XPS). The chapter concludes with an overview of the electrochemical study conducted through the following tests: cyclic voltammetry (CV), charge/discharge (CD), and Electrochemical Impedance Spectroscopy (EIS).

Chapter three systematically examines the impact of critical hydrothermal processing variables, namely precursor stoichiometry (Ni:Mn = 0:1, 1:0, 1:1, 1:2 and 2:1), and thermal regime (120 and 180 °C), on the crystalline structure evolution of synthesized Ni:Mn mono- or bi-nanostructures. Subsequently, a comprehensive characterization of the synthesized nanostructures is conducted employing the techniques outlined in Chapter two to elucidate their structural, morphological, and textural properties. Electrochemical investigations are then undertaken to assess the materials' potential as supercapacitor electrodes, with particular emphasis on correlating the impact of synthesis conditions with electrochemical performance.

Chapter 1:

Literature Review

Introduction

A comprehensive understanding of energy storage mechanisms is extremely important for the development and optimization of high-performance energy storage devices. Knowledge of ion storage and transport processes provides a fundamental foundation for advancing these technologies. To this end, this chapter initiates with a foundational exploration of electrical energy storage principles, encompassing electrostatic, Faradaic, pseudocapacitive, and intercalation processes, as well as the core components of energy storage systems. To bridge the technological gap between batteries and capacitors in high-power applications, supercapacitors were introduced. Subsequent sections will delve into the fundamental principles governing supercapacitor operation, including their compositional and material properties. A comparative analysis with other electrochemical energy storage technologies will position supercapacitors within the broader energy storage landscape, and an overview of their diverse applications across various sectors will also be highlighted. This chapter will conclude with a discussion of various nanostructured materials synthesis methods used in the field.

1. Physical principles:

Faradaic and non-faradaic processes are two fundamental ways in which electrical energy can be stored in electrochemistry. The difference between the two processes is clearly discussed in several sources [9, 10].

1.1. Non-Faradaic process:

capacitive or non-Faradic refers to the process in which energy is stored electrostatically through the adsorption of ions at the interface of a solid electronic conductor, such as an electrode, and a liquid ionic conductor, such as an electrolyte, as a result of the transfer of electrons into or out of the electrode [11]. The Helmholtz-Gouy-Chapman-Stern-Grahame model is the commonly accepted theoretical framework that explains the behavior of the EDL in this scenario, assuming a flat and solid electrode surface in contact with a typical electrolyte, such as a salt dissolved in a solvent as shows **Figure 1** [12].

- The Helmholtz model, first described by Hermann von Helmholtz in 1853, laid the foundation for understanding the electric double layer (EDL). It proposed that the potential difference near the electrode surface was caused by the accumulation of ions, and that the potential difference between the electrode and electrolyte was constant in the diffuse layer [13]. However, it has some limitations, such as not considering the finite thickness of the diffuse layer and the ion size. The model also assumes that the density of ions in the diffuse layer is proportional to the concentration of ions in the electrolyte, and the distance "d" is known as the Helmholtz distance which is the distance from the charged surface to the center of the ion. Despite being the first theoretical description of the EDL, the Helmholtz model did not provide adequate explanations **Figure 1 a**.
- The Helmholtz model of the electric double layer (EDL) in **Figure 1 b** was modified by Gouy and Chapman by considering a continuous distribution of electrolyte ions due to thermal motion in the electrolyte solution, referred to as the diffuse layer. This model suggested equal distribution of opposite ionic charges in the liquid surrounding the charged solid and that the ions were not attached rigidly to the surface. However, this model leads to an overestimation of the EDL capacitance as it assumes point charges infinitely close to the interface, leading to a large capacitance value [14]. Gouy introduced the use of Boltzmann statistics to explain the capacitive behavior of the EDL, leading to a volumetric distribution of charges in the electrolyte, known as the diffuse

layer. However, the Gouy-Chapman model still tends to overestimate the ionic concentration close to a charged surface.

- Later, Stern improved Gouy and Chapman's theory by combining the Helmholtz and Gouy-Chapman models, introducing the dimensions of ions and solvent molecules, and dividing the space charge into two distinct regions: Inner Helmholtz Plane (IHP) made up of strongly adsorbed ions and Outer Helmholtz Plane (OHP) consisting of ions with limited approach to the surface, as shown in Fig. ψ, and ψo refers to the potential, and the electrode potential respectivly. This modification is the most accurate model for flat surfaces. The EDL capacitance is a combination of capacitances from these two regions as ilistrate **Figure 1 c** [15].

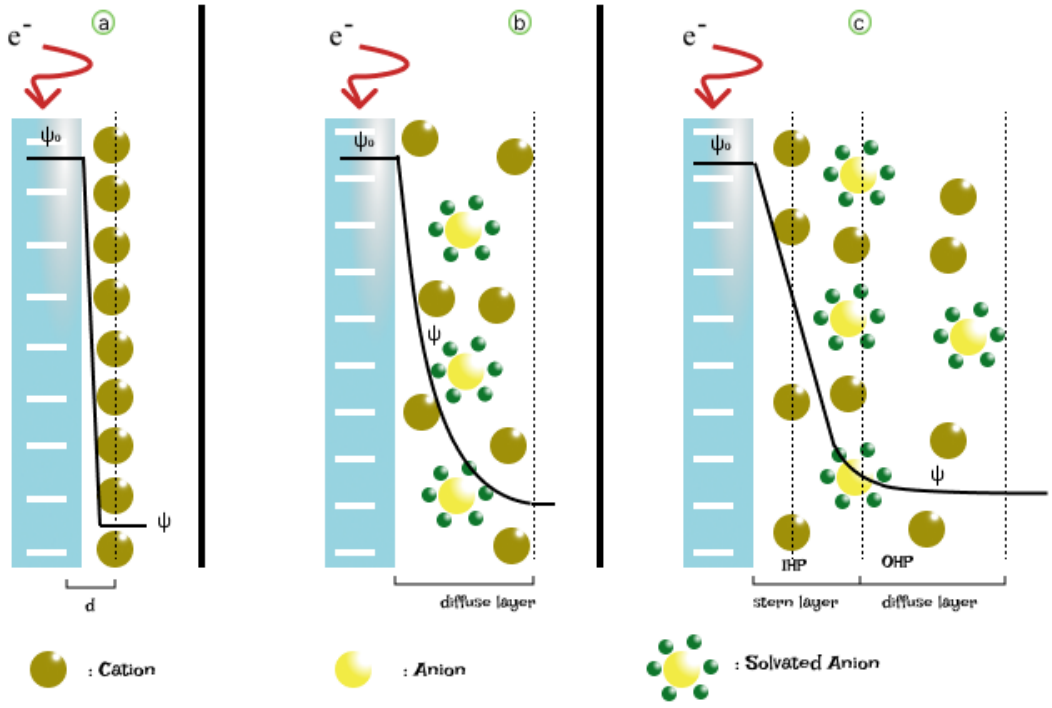

Figure 1. Schematic of a) The Helmholtz model, b) the Gouy-Chapman model, and c) the Stern model, at negatively charged surface. In these models, the symbol ψ represents the potential, while ψo refers to the electrode potential.

This models for double layer formation in electrolytes are limited to traditional systems and cannot be applied to newer systems such as ionic liquids. In ionic liquids, the structure of the double layer is suggested to vary depending on the potential of the surface [16]. Double layer

structures can be formed and modified quickly, allowing for fast charging and discharging of electrodes, but they are not stable over an extended period and will self-discharge relatively fast. Carbon material is commonly used as an electrode due to its high specific surface area, low cost, and high electrical conductivity. The amount of charge that can be stored in double layers is relatively low compared to other charge storage mechanisms, but it can be increased by increasing the surface area of the electrode and the electrolyte potential window [12].

1.2. Faradaic process:

The term "faradaic" is derived from Michael Faraday's name, in recognition of his contributions to the understanding of the nature of electric current and its relationship to chemical reactions. storing electric energy in a material by means of an electrochemical reaction. This process involves the conversion of electrical energy into chemical energy, in these types of reactions, one or more electrons are transferred between an electrode and an electrolyte, resulting in the formation or consumption of one or more chemical species [17].

The fact that the entire volume of the active material participates in the storage of charges during the electrochemical transformations lead to significant specific energies, particularly in the case of batteries, which store energy in the form of chemical bonds between the electrode materials and the electrolyte. However, in this electrochemical systems, dimensional changes can occur due to the insertion or removal of ions into or out of the electrode material. These changes can result in stress on the electrode, which can lead to degradation of the electrode's integrity and performance over time. Phase transitions, such as solid-state phase transformations, can also lead to significant volume changes that can affect the integrity of the electrode. When an electrode material undergoes a phase transition, it can release the stress that was accumulated due to the dimensional changes caused by ion interactions. moreover, phase transitions can also introduce new stresses and can cause the electrode to become more brittle, leading to poor cycling performance. The kinetics of phase transformations can also affect the performance. Displacement-controlled phase transformations, which involve the movement of atoms within a crystal lattice, are typically diffusion-limited, which means that the rate of the transformation is dependent on the rate at which atoms can move through the lattice. This can result in slow transformation kinetics, which can affect the rate at which ions can be inserted or removed from the electrode. Nucleation and growth processes are also important factors to consider when studying phase transformations in electrochemical systems. Nucleation refers to the initial

formation of small clusters of atoms or ions that will grow to form the new phase. The kinetics of nucleation can affect the rate at which the new phase forms, and thus can also affect the rate at which ions can be inserted or removed from the electrode [18].

It is crucial to recognize the importance of the latest developments in research of nanomaterials that employ faradaic processes. These advancements have given rise to new phenomena, such as Intercalation and pseudocapacitance which have a significant impact on energy storage by boosting the capacitance and energy density of materials used in batteries and supercapacitors [19, 20].

Intercalation:

Intercalation/insertion is a process involve the insertion or removal of ions between the layers of a layered material, such as metal oxides. The amount of charge that can be stored is determined by the number of ions inserted into the crystal lattice and the number of active atoms interacting with the electrolyte. The number of potential insertion sites is influenced by the crystal structure of the material and the type of electrolyte used. As the ions are inserted and removed from the electrode material, they alter the metal valence and result in changes in the volume of the material (expanding contracting) limit its lifespan.

The main limitations of intercalation-type materials are typically the slow movement of ions through the electrode. However, there are ways to address these issues and enhance high-power performance. By improving ion diffusion in the material, it is possible to increase the number of ions inserted during high-power operation. This can be accomplished by reducing the size of the active material particles in the electrode, known as nanosizing, which can also increase the fraction of charge stored at surface sites and reduce the impact of structural changes in the material [21].

Pseudo capacitance:

refers to fast charge transfer reactions that occur at the surface of certain materials [22], such as metal oxides and conducting polymers. These reactions are non-diffusion limited and do not cause a crystallographic phase change in the material. However, the resistance of the electrodes can be a significant limitation for pseudocapacitive materials. To overcome this limitation, the active materials can be made in small and thin layers or particles, ideally within a few nanometers, which reduces resistance and increases the surface area and the number of active atoms interacting with the electrolyte, leading to more efficient charge storage [23].

2. Electrochemical energy storage Devices:

The different electrochemical storage mechanisms can be used to create different types of devices. And the common way to compare energy storage devices is by their capability of supplying energy or power. the power density is related to how quickly the device can deliver or accept electrical energy, while the energy density is related to how much energy can be stored in the device per unit mass or volume.

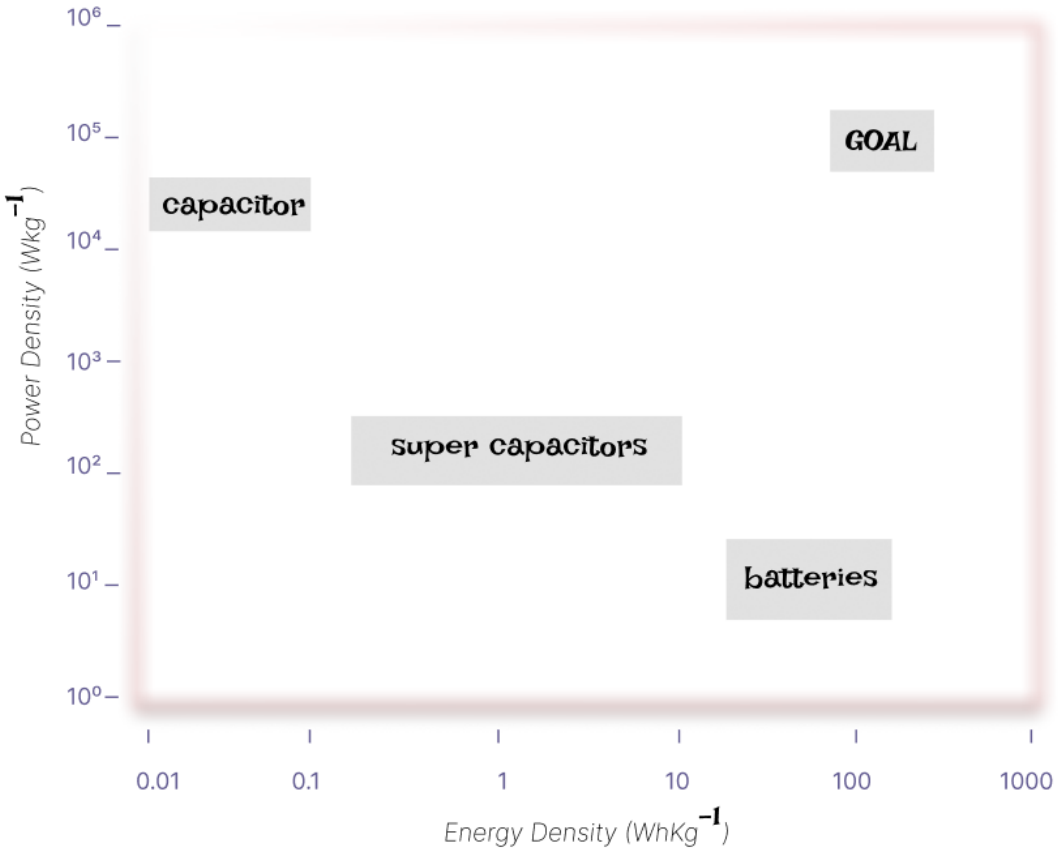

Figure 2. Comparison of the energy and power density of storage devices.

The Ragone chart showing in **Figure 2**. is a graphical representation of the performance of different energy storage devices. It plots the energy density of the device on the y-axis and the power density of the device on the x-axis. This plot explains that the batteries are high-energy systems, whereas conventional capacitors are high-power systems. SCs have intermediary power and energy capabilities. The goal that researchers strive to achieve is the device with the highest energy efficiency closer to the top-right corner of the graph [24].

Some of the most common types include batteries and SCs:

there are two main types of batteries: primary and secondary. Primary batteries, like the Leclanché cell (Zn/MnO2), are designed for single use and rely on active materials in the electrodes to generate an electrical current. Once these materials are consumed, the battery can no longer produce a current and is dead. On the other hand, secondary batteries, such as Lithium-ion batteries, are designed for multiple use and rely on reversible faradaic reactions to generate an electrical current. These batteries can be recharged and used multiple times, making them a more efficient and sustainable power source. Lithium-ion batteries use lithium ions that move between a positive electrode (anode) made of lithium cobalt oxide (LiCoO2) and a negative electrode (cathode) made of carbon. Due to their high energy density, long lifespan compared to other storage devices and re-usability, they are widely used in a variety of applications, including portable devices, electric vehicles and renewable energy systems. lithium-ion batteries have several drawbacks including limited lifespan, temperature sensitivity, safety concerns, high cost, limited resource, and disposal issues. Safety concerns include the risk of fire or explosion due to overcharging, puncture, or physical damage. Disposal of lithium-ion batteries also poses a risk to the environment and human health as they contain toxic materials and should be handled and recycled properly [25].

Capacitors and supercapacitors consist of two conductive plates, called electrodes, separated by a non-conductive material called a dielectric. The dielectric can be a solid, liquid, or gas. The main difference between the two is the amount of energy they can store. Capacitors can store a limited amount of energy, while supercapacitors can store much more. This is achieved by using a porous carbon, metal oxide or conducting polymers as the electrode materials and an electrolyte as the dielectric.

Scientists are actively researching ways to improve the performance of this electrochemical storage devices, by creating new nanostructured materials and combining different storage mechanisms, such as supercapacitors and batteries. These devices, called supercapbattery [26, 27], combines the high-power density of supercapacitors with the high energy density of batteries as showing in **Figure 4**, resulting in a device with a high overall performance. All these research efforts aim to increase energy density, power density, and lifetime, reducing cost, and making them more environmentally friendly.

3. Supercapacitors SCs:

Supercapacitors, also known as ultracapacitors, are energy storage devices that have the unique ability to be composed entirely of non-toxic materials. They are widely used in applications where high-power density and fast charge and discharge rates are required [28].

3.1. Cell design:

Supercapacitor cells consist of two electrodes that store electrical charge, an electrolyte for ionic conductivity, a separator to prevent short circuits, and a current collector to gather current. These components work together to form a functional supercapacitor cell as showing **Figure 3** [29, 30].

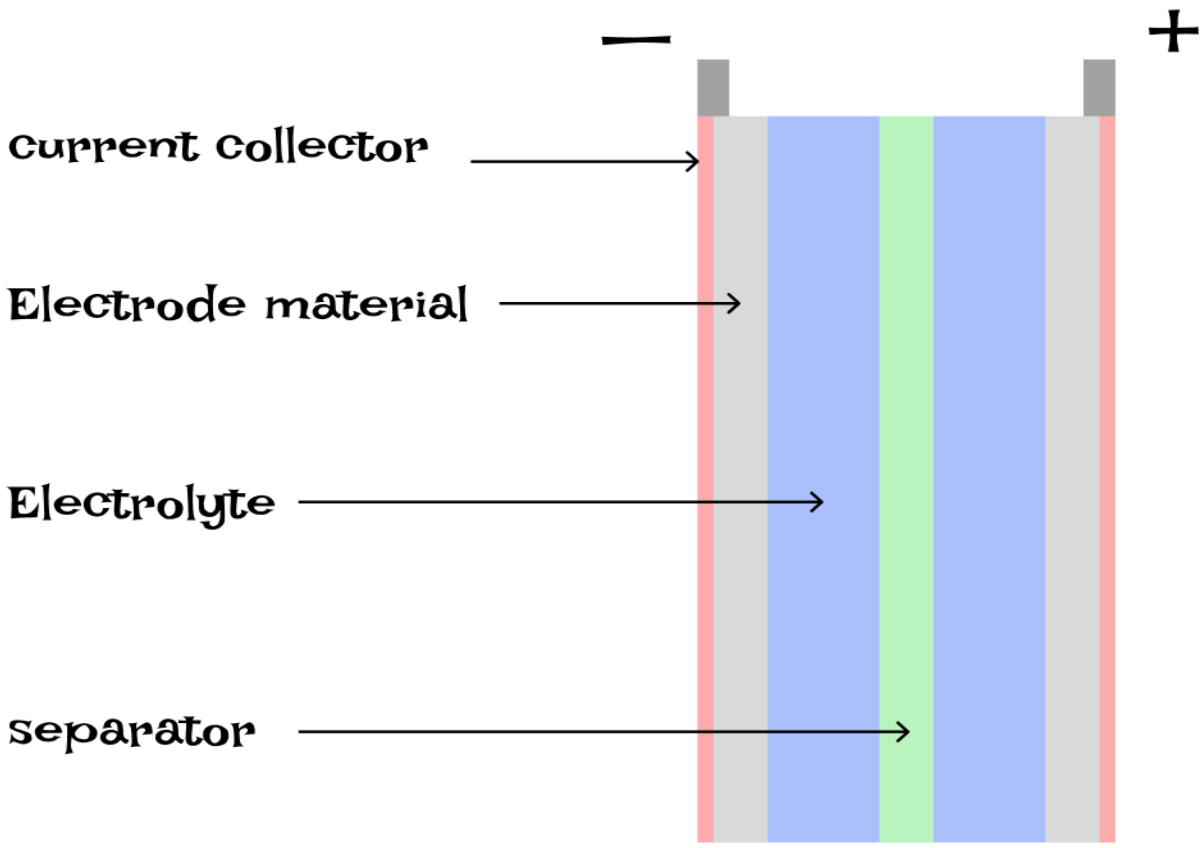

Figure 3. Structure of SC.

3.1.1. Electrode materials:

Supercapacitor (SC) electrodes should provide high energy density without compromising the power density, rate capability, and cyclic stability. And for that the material must feel full a specific criteria like surface properties, electrical conductivity, pore structure, and surface area and other proprieties that play a crucial role in determining the resulting electrochemical

behavior [31]. Pores, being the primary source of surface area, must be considered for their size and accessibility in electrochemical systems. According to the IUPAC classification of pores from 1985, pores with diameters less than 20 Å are classified as micropores, 20-500 Å as mesopores, and greater than 500 Å as macropores (Edlc, n.d.), [32, 33, 34].

Supercapacitor electrodes can be made from a range of materials, including carbon, transition metals, conductive polymers, and composites. The choice of material depends on desired properties for targeted applications [35].

- Carbon material:

Carbon is a popular material in supercapacitors, owing to its properties as a standalone electrode in EDLCs, resistance to corrosion, conductivity, high surface area, affordability, and the abundance of carbon-based options [36].

Different types of carbon electrode materials commonly used in SCs:

Activated carbon are obtained from carbon-rich organic precursors which can be easily derived from natural renewable sources like wood, coconut shells, fossil fuels, or from their derivates like pitch coal. This is achieved using partial controlled oxidation of carbon precursor grains either by physical or chemical activation leading to creates a porous structure and increases its surface area. Depending on the activation methods as well as the carbon precursor used, numerous AC materials with various physicochemical properties have been used as supercapacitor electrodes [37, 38].

The discovery of CNTs has revolutionized the science and engineering of carbon materials. Possessing unique physical properties, such as excellent chemical and mechanical stability, CNTs, including both single-walled (SWCNTs) and multi-walled (MWCNTs), have proven to be highly promising as electrodes in electrochemical energy storage. Furthermore, the mesoporous structure of CNT networks enhances electrolyte diffusion, leading to a higher maximum usable power. This has resulted in the establishment of a production market for CNT-based electrodes [39, 40].

Carbon aerogels (CAs) possess unique characteristics as low density and high porosity, making them an ideal choice for use as supercapacitor electrodes. Produced through sol–gel chemistry, and the freeze-drying of carbon suspensions. the properties of CAs can vary based on the precursor material, gel type, and desired final product features [41, 42].

Graphene is a material that consists of a single layer of carbon atoms arranged in a hexagonal lattice, and there are several ways to produce it such as mechanical exfoliation, chemical vapor deposition, and reduction of graphene oxide. Graphene is known to be incredibly strong, lightweight, and has excellent electrical conductivity, making it a promising material for high-performance energy storage applications. However, the low gravimetric density of exfoliated graphene is still an issue [43, 44].

- Transition metal-based materials:

Transition metal-based materials have garnered significant attention as pseudocapacitive electrode materials for supercapacitors due to their high specific capacitance compared to that of carbon and the variety of valence options they offer. Among these materials, ruthenium compounds with rapid reversible redox processes and high chemical stability have been widely investigated. However, their primary drawback is their high cost, toxicity, and use in small devices limited their applications [45].

Other types of materials, such as those containing iron (Fe), vanadium (V), nickel (Ni), cobalt (Co), and manganese (Mn), are less expensive and have shown promising potential for the development of high-performance SC electrodes. However, the wide application of transition metal oxides is limited by its intrinsically low electric conductivity and chemical stability. Therefore, further research and development are needed to optimize their properties and overcome these limitations to promote their practical use. Of these, manganese and nickel are the most promising materials for supercapacitor electrodes [46, 47].

- conducting polymers:

Conducting polymers have gained significant interest as electrode materials for supercapacitors in recent years, owing to their excellent electrical, mechanical, and chemical properties. Moreover, they are relatively easy to produce and can be processed into various forms, such as films or fibers, which offers greater flexibility in the design of supercapacitor devices. Among the most extensively investigated conducting polymers for supercapacitor electrodes are polyaniline (PANI), polypyrene, and poly-(3,4-ethylenedioxythiophene) (PEDOT). However, they may exhibit limited temperature stability, power density, and cyclability, which can limit their long-term reliability and performance [48, 49].

- Composites:

Many strategies were proposed to boost the overall performance of SCs electrode materials Developing advanced materials is crucial towards high performance SCs. Composites typically consist of two or more materials, with each component possessing its own unique physical, chemical, and mechanical properties. resulting in a combined faradaic and non-faradaic charge storage mechanism within a single electrode. These electrodes provide high specific surface area (SSA) and conductivity using carbon materials, while pseudocapacitive materials further increase the capacitance [45, 50].

3.1.2. Electrolytes:

Developing materials for supercapacitor applications requires careful consideration of their interaction with the electrolyte. The selection of the electrolyte is as important as the choice of electrode material, as it determines the device's voltage-holding capacity, affecting its specific energy and specific power, which vary as the square of the nominal voltage.

Several types of electrolytes are used in supercapacitors, but no single one meets all the requirements, which include electrolyte conductivity, salt effect, solvent effect, electrochemical stability, and thermal stability [51].

Aqueous electrolytes, which use water as the solvent, are commonly used in supercapacitors due to their low cost, high ionic conductivity, and good safety profile. The pH of aqueous electrolytes can range from very acidic to strongly alkaline, depending on the choice of salt used. Common examples of salts used in aqueous electrolytes include potassium hydroxide (KOH), sodium sulfate (Na2SO4), and hydrochloric acid (HCl). However, they have a limited operating voltage window, resulting in lower energy density. This limitation is due to the potential difference of water electrolysis, which stands at 1.23 V [52].

Organic electrolytes can operate at higher voltages, but they are toxic. Ionic liquids, on the other hand, can also operate at elevated potentials. However, using these electrolytes presents a significant challenge since they typically exhibit lower ionic conductivity due to their relatively high viscosity and the limited mobility of ions within the solvent [53].

Overall, the choice of electrolyte for a supercapacitor depends on the specific application requirements, including the desired voltage range, energy density, and safety considerations.

3.1.3. Separator:

The role of a separator is crucial for the efficient functioning and safety of supercapacitors, as it allows ions to pass through while blocking the flow of electrons. Despite its importance, only a few papers have reported on the study of separators for energy storage devices.

Recent research has focused on identifying suitable separator materials that exhibit characteristics such as strong electrolyte wettability, high and robust ionic conductivity, excellent mechanical and electrochemical stability, and cost-effectiveness. Generally, a ceramics or fiberglass are used in an aqueous environment, while polymer or paper is used in an organic environment [31].

3.1.4. Current collector:

The performance of supercapacitors (SCs) is heavily dependent on the function of the current collector. This component plays a critical role in collecting electrons from the electrode material and transporting them to the external circuit. An ideal current collector should possess excellent electrical conductivity, be corrosion-resistant, and have a low cost, while enabling resistance-free transportation of electrons. In addition, the current collector should have sufficient mechanical strength to provide support to the entire cell. Traditionally, copper or aluminum have been used as current collectors. However, recent advancements have introduced alternative options such as nickel mesh, metal foams, and carbon cloth, which can offer increased surface areas for the electrode material. This can lead to uniform dispersion of the electrode and lower contact resistance, further enhancing the performance of SCs [54].

3.2. Classification:

SCs can be classified based on the size and nature of their electrodes into symmetric and asymmetric types. Additionally, they can be manufactured in cylindrical, flat, or rectangular shapes. The most well-known classification is based on their energy storage mechanism, which includes electrical double-layer capacitors, pseudocapacitors, and hybrid capacitors **Figure 4** [55].

3.2.1. EDLCs:

Electric Double-Layer Capacitors (EDLCs) that are commercially available typically use two carbon-based materials as electrodes. This is due to their high specific surface area, low cost, and high electrical conductivity. this type of SCs is commonly used in applications where a long-life cycle and high power are required [56].

When a charging voltage is applied to the electrodes, ions migrate to the pores of the electrode with an opposite charge. Conversely, ions are repelled when discharging a capacitor. The specific capacitance of the EDLC relies on physical adsorption on the surface, and it is directly proportional to the accessible surface area of the electrode and the maximum voltage provided by the electrolyte used as showing in **Figure 4 a**.

There are limitations stemming from the interconnections between specific surface area, porosity, strength, and electrical conductivity. In simple terms, as the carbon's porosity increases, its specific surface area expands, but this comes at the cost of reduced strength and lower conductivity.

Moreover, excessive porosity can lead to issues, as pores that are too small for electrolyte ions will not participate in storing electrical charge. P. Simon and Y. Gogotsi reported that the recognition of the impact of pore size and ion desolvation in micropores is the reason behind the maximum capacitance being obtained when the ion size matches the carbon pore size. In other words, ions enter the micropores without their solvation shell, as confirmed by in-situ studies of ion adsorption in carbon pores in organic and aqueous electrolytes [57].

3.2.2. Pseudocapacitors:

Pseudocapacitors use electrodes made of various materials, including powdered metals (e.g. Ru, Rh, Os, Au, In, W, V, Ni, Mn, Co, and Nb), bromides, chlorides, nitrates, phosphides [55], extensively studied transition metal oxides, and conducting polymers, due to there being cheap, abundant, and offer large game of nano structure [58].

to store energy with high density. They are called "pseudocapacitive supercapacitors" because their electrical behavior resembles that of capacitors, but with faradaic charge storage resulting from the change in the valence state of the electrode material as showing **Figure 4 b, e, h**. This causes electron transfer and electrochemical adsorption of ions on or near the electrode surface.

This mechanism is described in **Figure 4** The cyclic as well as voltammograms of these materials displays broad redox peaks with a quasi-rectangular shape, and a linear relationship between the charge stored and the charging potential within a specific range. Unlike batteries, the redox reactions in pseudocapacitors occur at rates comparable to those of electrical double-layer charge storage, without being limited by semi-infinite diffusion [59]. However, pseudocapacitors have a shorter lifespan and lower power density. To ensure a long cycle life, the redox reactions must be reversible. The capacitance of the pseudocapacitor is proportional to the number of electrons transferred, which depends on the number of active atoms in contact with the electrolyte. Researchers are exploring the nature of the active materials and structural hierarchical nano-design to enhance the power and energy density of pseudocapacitors [60].

3.2.3. Hybrid supercapacitors (HSCs):

They are also known as asymmetric supercapacitors, which differ from previous types that utilized similar electrode mechanisms. These devices rely on dissimilar types of electrodes, combining both electric double-layer capacitors (EDLCs) **Figure a, d, g** and pseudocapacitors (PCs) to achieve higher energy density for the EDLCs, extended life and greater power for PCs **Figure 4 a, b**. They are typically used in applications that require a balance between high power and energy density. It's worth noting that achieving charge balance and peak performance during operation, while considering the distinct storage mechanisms, may also require adjusting the mass ratio of the two electrodes [61].

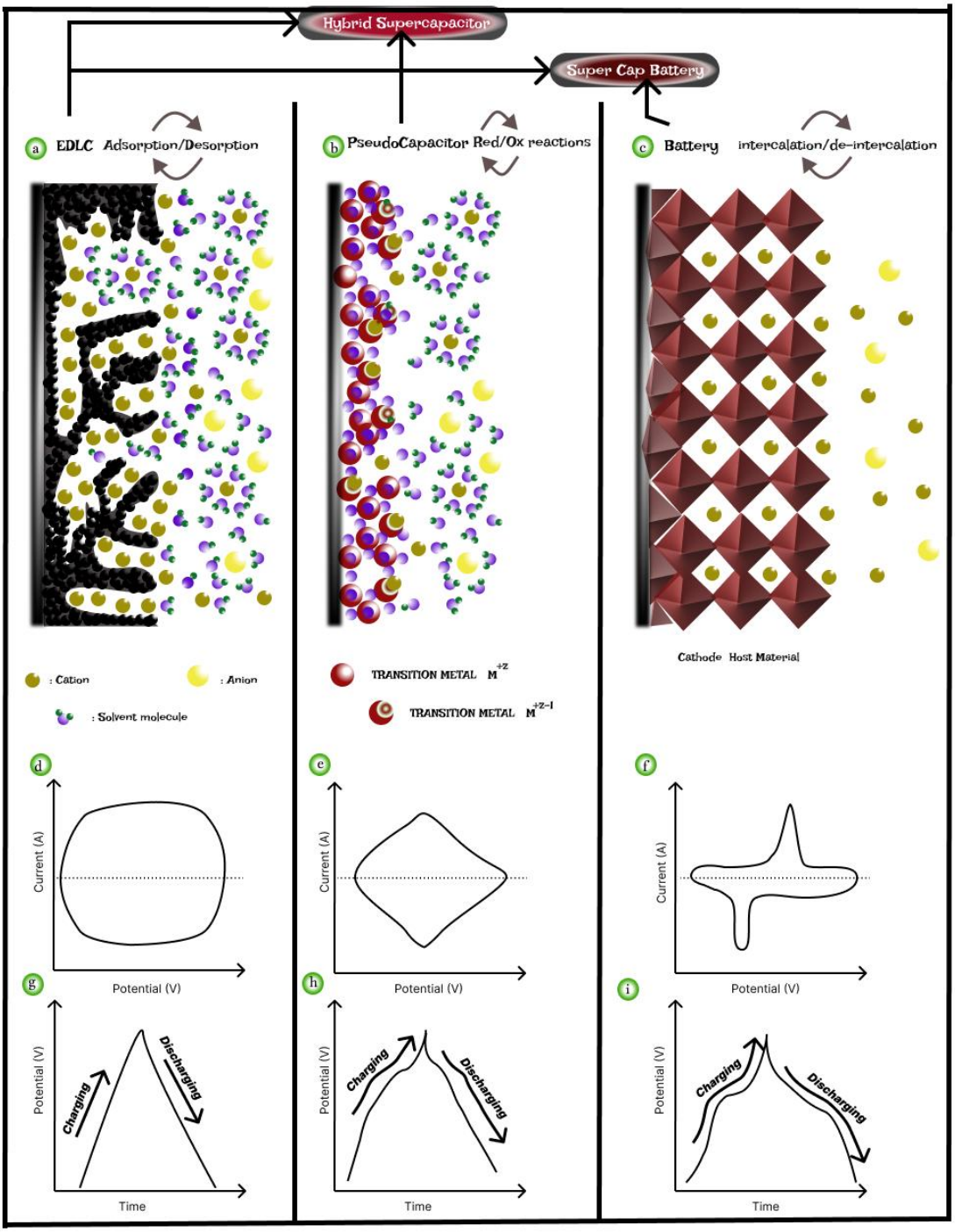

Figure 4. The schematic illustration of the energy storage mechanisms with their corresponding electrochemical signatures (representative shapes of CV and CD curves): (a d g) electrical double layer capacitance, (b e h) surface redox capacitance, (c f i) faradic battery-type

3.3. Application:

Supercapacitors (SCs) have revolutionized energy storage by offering remarkable performance improvements. They possess high power density, long cycle life, and low maintenance requirements, making them an ideal choice for various applications in several sectors like transportation, renewable energy, military, and aerospace.

In the transportation sector, SCs are commonly used as backup energy storage devices in combination with high-energy batteries or fuel cells [62]. They can supply power for engine start, short launch boost, critical functions like brakes in the event of battery malfunction and reduce operational expenses while prolonging the battery's lifespan. SCs have also replaced batteries in tram transportation that involves frequent stops over short distances. For instance, the capacitor buses in China are named after capacitors and benefit from SCs' long lifespan (million charge cycles) and high power, enabling an 80-second recharge at stop stations while passengers are getting on or off from the bus.

In the renewable energy sector, SCs play a crucial role in stabilizing power sources and smoothing out fluctuations from sources like solar cells, wind turbines, and ocean waves. They offer quick response time, the ability to withstand harsh environments, and low maintenance requirements, providing a reliable and stable power source for sustainable energy production.

SCs are used in applications that require high power, such as elevators and. The low weight and volume of energy storage and flexibility. The stored energy can power communication devices or other wearable electronics, eliminating the need for separate power sources, reducing overall weight and providing a sustainable and efficient source of energy [63].

Figure 5: Some examples of SC applications.

Supercapacitors are also widely used in electric utilities such as power tools, flashlights, cranes, elevators, airbag exploitation, and more as showing **Figure 5** [64].

4. Nanostructured material synthesis routes:

Molecules and atoms serve as foundations for all objects. It is essential to comprehend how these fundamental units are assembled, as it greatly influences the properties and interactions of the resulting structures. Controlling the synthetic pathways is a crucial aspect in the preparation of nanostructured building blocks, with diverse sizes and shapes that can lead to the development of innovative devices and technologies with enhanced performances.

In general, there are two main approaches for the synthesis of nanostructured materials, The first is a top-down, involving the miniaturization of components and materials. The second approach is a bottom-up, wherein we construct increasingly complex nanostructures atom by atom or molecule by molecule [65].

4.1. top-down methods:

In the top-down approach (often referred to as a destructive method), bulk materials are divided to produce nanostructured materials. This method has been advanced by Richard Feynman, it is well-suited for achieving structures with long-range order and establishing connections with the macroscopic world. The primary drawback of the Top-down approach lies in the imperfection of the surface structure. For example, the nanoparticles generated through attrition exhibit a relatively wide size distribution and diverse particle shapes or geometries. Additionally, they may contain a significant number of impurities. Some examples of the top-down method are Lithography, ball milling or mechanical milling, sputtering… [66, 67].

Lithography:

This technique utilizes a focused beam of light or electrons, proving to be a valuable tool in constructing nanoarchitectures. Lithography can be categorized into two types: masked and maskless lithography. Within masked nanolithography, nanopatterns are transferred across a considerable surface area using a designated mask or template. Masked lithography includes techniques such as nanoimprint lithography, photolithography, and soft lithography. In maskless lithography, the process involves the arbitrary writing of nanopatterns without the use of a mask. Maskless lithography comprises focused ion beam lithography, scanning probe lithography, and electron beam lithography [68].

mechanical milling:

Mechanical milling is the most widely used top-down method for producing blends of different phases at the nanoscale level, and it is helpful in the production of nanocomposites [69].

The milling takes place within cylindrical containers referred to as vials, which containing balls. The nature of the milling tools varies and can include materials such as steel, agate, tungsten carbide, and more. Typically, the vials are filled under an inert atmosphere to prevent side reactions, this precaution is essential since the particles are fractured during the milling process exposing new highly reactive surfaces that may react with the surrounding gases [70].

This method is extensively employed in the production of nanoalloys based on aluminum, nickel, magnesium, copper, and diverse nanocomposite materials. this technology could be also regarded as a green technique for the manufacturing of innovative nanostructured materials from ecofriendly resources [71].

Sputtering:

sputtering belongs to the category of PVD techniques initially developed for applying thin film materials to surfaces [72]. Sputtering is a physical phenomenon wherein the physical bombardment of a target surface by energetic gaseous ions, such as noble gas cations result in the ejection of surface atoms [73], and a standard vacuum chamber is employed for the deposition of coatings using this process. This method may have important applications such as heterogeneous catalysis, gas sensor technology and microelectronics [74].

4.2. bottom-up methods:

The bottom-up approach, also known as the constructive method, consists of building structures atom by atom or molecule by molecule, or aggregate by aggregate. The assembly of these nano-objects is carried out in a precise control, and good mastery of their structures and architecture. Since nanostructures are formed autonomously during the synthesis of materials using this approach, there is a reduced risk of introducing defects during fabrication, leading to a significant reduction in defects. Although the bottom-up approach allows for precise control, certain properties of the resulting materials may not be optimal for some applications. For example, electrical conductivity or mechanical strength may not be ideal [75].

Chemical Vapor Deposition (CVD):

This technique, also known as film deposition or thin-film coating, involves the formation of a solid material through a reaction activated by an energy source, where reactive gaseous species interact with the surface of a substrate. The most common activation process is thermal, which can be assisted or substituted by a plasma process (PE-CVD), by radiation with particles (electronic EB-CVD or ionic IB-CVD), or photons of sufficient energy (PH-CVD). CVD reactors are divided into two main categories: those with hot walls and those with cold walls, and depositions are typically carried out under vacuum conditions. CVD enables the synthesis of well-ordered thin films and requires high-purity metallic precursors, making it an excellent method for producing high-quality nanomaterials [76].

Sol-gel method:

This process represents one of the chemical pathways for preparing nanostructured materials, typically conducted under hydrolytic conditions and at significantly lower temperatures than those of conventional synthesis routes. The process initiates with basic chemical reactions triggered by the precursors upon contact with water. Initially, hydrolysis of the alkoxy groups occurs, forming reactive species, which then undergo the formation of oxo bridges, followed by the condensation of the resulting hydrolyzed products, leading to gelation within the system. These gels are subsequently converted into amorphous, dry matter either by solvent removal or simple evaporation under atmospheric pressure [77].

One advantage of this process is the wide availability of precursors for numerous metals and non-metals, existing in either liquid or solid states, with most being soluble in common solvents. Simplified implementation is facilitated by the viscosity of sols and gels, enabling the direct elaboration of materials in various forms such as thin films, fibers, fine powders, and bulk materials. Additionally, these conditions allow for the combination of organic and inorganic species to produce new families of organo-mineral hybrid compounds with novel properties [78].

However, it's important to note that the chemical reactions occurring during the material synthesis may vary significantly depending on the type of precursors used, often leading to concerns regarding the homogeneity of solid products [79].

conclusion

This chapter presents a comprehensive literature review on Electric Energy Storage (EES), focusing on its fundamental principles and various storage processes. Emphasis is placed on supercapacitors, exploring their composition (including electrodes, current collectors, separators, and electrolytes), material characteristics (such as carbon, transition metals, and conducting polymers), and operating mechanisms to inform the development of next-generation devices, including pseudocapacitive and hybrid types. The review also discusses supercapacitor applications across diverse fields and concludes with a discussion of various nanostructured materials synthesis methods used in the field.

Chapter 2: Experimental Methodology

Introduction

Transition metal-based nanomaterials, particularly those incorporating nickel, manganese, zinc, cobalt, and iron, have garnered significant attention as promising electrode materials for supercapacitors due to their high capacitance and low environmental impact. This study aims to develop a controlled synthesis strategy for nanomaterials with optimized properties. The hydrothermal method was selected for its simplicity, cost-effectiveness, and potential for producing nanostructures with desired characteristics. To investigate the influence of synthesis parameters on material properties, nickel and manganese-based nanomaterials will be prepared at varying precursor ratios and temperatures (120 and 180 °C). A comprehensive characterization program will be employed to correlate synthesis conditions with structural, morphological, and compositional properties, ultimately enabling the optimization of these materials for energy storage applications.

1. Synthesis of Ni/Mn Nanohybrids

Hydrothermal methods:

Although significant technological progress has been made and advancements in understanding this experimental method have been achieved, defining hydrothermal synthesis remains a challenge. From its first usage around 1840 to the present day, the scientific community remains divided on a single definition. Over the course of these centuries, several definitions have been proposed, including those by Murchison, Morey, Niggli, and Rabenau.

Given the considerable number of works conducted under so-called moderate hydrothermal conditions, in 2001, Mr. Byrappa and Mr. Yoshimura proposed a definition of hydrothermal synthesis: "all heterogeneous chemical reactions occurring in the presence of a solvent (aqueous or non-aqueous), above ambient temperature and at a pressure higher than 1 atmosphere, within a closed chamber." This term derives from "hydro" for water and "thermal" for heat, indicating the involvement of both elements. Notably, these reactions can occur regardless of the solvent employed, be it aqueous or non-aqueous.

The principle of this method consists of introducing the reactants and a solvent into an "autoclave" digestion bomb and then heating it to increase the pressure inside the chamber, which corresponds to the vapor pressure above the solution. It depends on its composition, temperature, and the filling rate of the autoclave.

Since this definition has not yet gained consensus within the scientific community, the synthesis method is termed solvothermal, which means that water, but also other solvents, are used, in accordance with the general process principle. Additionally, terms like "glycothermal," "alcoholthermal," or "ammonothermal" have arisen based on the solvent used in the syntheses [80].

Furthermore, hydrothermal synthesis offers the advantage of achieving precise control over the chemical composition, phase purity, size, and morphology of the products by adjusting growth parameters such as chamber pressure, the nature of the reactants, reaction duration, initial pH, and temperature. Another advantage is the ability to synthesize low-cost mixed oxides for producing various nano-geometries of materials, such as nanowires, nanorods, nanosheets, and nanospheres [81, 82, 83, 84, 85].

Hydrothermal synthesis appears to be a promising alternative that addresses these issues in material production. The disadvantages of hydrothermal synthesis are mainly related to the large number of variables involved.

This thesis study conducted at the LEREC laboratory, Badji-Mokhtar University of Annaba, employed an experimental protocol utilizing hydrothermal synthesis as follows:

Dissolving 0.1 M Nickel (II) chloride hexahydrate (NiCl2.6H2O) (Sigma-Aldrich, purity≥99.99%), 0.1 M Manganese (II) chloride tetrahydrate (MnCl2.4H2O) (Reachem Chemicals, purity ≥ 90%), and Urea as surfactant (0.5 M) (Merck, purity ≥ 98%) in In a beaker containing 40 ml deionized water. The solution was subjected to sonication at room temperature until it became homogeneous, after which it was transferred into a 20 ml Teflon-lined autoclaves, consisting primarily of a stainless-steel body and a Teflon liner capable of withstanding hydrothermal conditions **Figure 6 a.** Following this, the autoclave was tightly sealed and placed in an electric oven where it was maintained at two growth temperatures, 120°C and 180°C, for a duration of 6 hours. by varying the molarity of Ni and Mn precursors (e.g., Ni/Mn = 1/0, 0/1, 1/1, 1/2, and 2/1), while maintaining consistent growth conditions such as temperature and duration. a range of mono- and bimetallic nanostructures consisting of Ni or Mn carbonate or hydroxide nanohybrids were synthesized. Subsequently, the autoclave was left to cool naturally to room temperature, and the resulting products were filtered and washed multiple times with distilled water prior to being dried overnight at 80°C **Figure 6 b**.

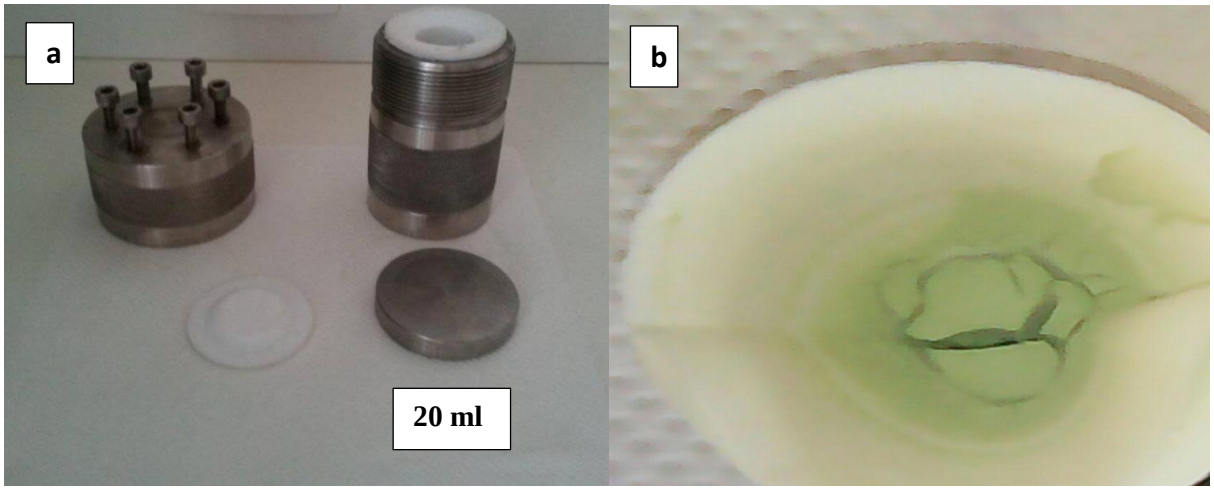

Figure 6: a. Autoclave (20 ml), b. Filtered powder.

The primary reactions involved in the urea homogeneous hydrolysis method for synthesizing NiMn carbonate and/or hydroxide are outlined as follows [86]:

Urea hydrolysis:

$$CO(NH2)_2 + H_2O \rightarrow 2NH_3 + CO_2 \quad \text{(Eq. 1)}$$

Ammonia ionization:

$$NH_3 + H_2O \rightarrow NH_4 + OH \quad \text{(Eq. 2)}$$

Precipitation reaction of $Ni(OH)_2$:

$$\text{Ni(OH)}_2 : Ni_2+ + 2HO^- \rightarrow Ni(OH)_2 \quad \text{(Eq. 3)}$$

Carbon dioxide ionization:

$$CO_2 + H_2O \rightarrow HCO^{3-} + H + or\ CO_2 + H2O \rightarrow CO_3^{2-} + 2H^+ \quad \text{(Eq. 4)}$$

Precipitation reaction of $Ni(HCO_3)_2$:

$$Ni(OH)_2 + 2HCO3^- \rightarrow Ni(HCO_3)_2 + 2OH^- \quad \text{(Eq. 5)}$$

Electrode's fabrication:

To assess the electrochemical performance of the mono- and biphasic nanohybrids based on Ni/Mn carbonate and/or hydroxide, electrodes **Figure 7** were prepared using the following method:

The freshly synthesized electroactive nanomaterials were combined with a conducting agent, carbon black (CB), and a polyvinylidene difluoride (PVdF) binder, along with a few drops of 1-methyl-2-pyrrolidone (NMP) solvent in an agate mortar. This mixture yielded a paste with a weight ratio of 80:10:10 (with an approximate active material mass of 1.5 mg). The resulting paste was then evenly spread onto a 1 × 1 cm2 area of pre-treated Nickel foam (NiF), which acted as the current collector. Subsequently, the assembly was dried at 80°C in an oven for 24 hours to ensure complete evaporation of the NMP solvent.

Figure 7: electrode.

2. Technical characterization

2.1. X-ray diffraction (XRD):

XRD is a versatile non-destructive technique used to study the structure of materials, enabling the extraction of extensive information such as phase composition, crystalline structure, and orientation of samples in powder, solid, and liquid forms.

The principle behind XRD is:

X-rays emitted by the source illuminate the sample, then they are diffracted by the sample's phase. These beams interfere with each other, producing intense signals in specific regions of space. These signals are captured by the XRD detector, resulting in a trace with distinct peaks known as diffraction peaks. The positions of these peaks serve as a unique signature of the atomic arrangement within a crystal. By moving the tube or the sample and detector to alter the diffraction angle (2θ, the angle between incident and diffracted beams), the intensity is measured, and diffraction data are recorded. Depending on the diffractometer geometry and the sample type, the angle between the incident beam and the sample can be fixed or variable and is typically associated with the angle of the diffracted beam.

The diffraction condition is described by Bragg's law, which establishes a relationship between the incident angle (2θ) and the spacing of lattice planes (d_hkl) as per the following equation:

$2d(kll) \sin \theta = n\lambda$ (Eq. 6)

Where:

d_hkl: Interplanar distance (the distance between crystal planes with indices "hkl").

θ: Incident angle of X-rays on the surface of the material under study.

n: Order of diffraction.

λ: Wavelength of the X-ray beam.

When a powder contains a specific crystalline phase, it consistently exhibits diffraction peaks in fixed directions, maintaining relatively uniform heights. Consequently, this diffraction pattern serves as an authentic identifier of the crystalline phase. Consequently, it's feasible to discern the characteristics of each crystalline phase within a mixture (whether it's a powder

blend or a polyphasic bulk sample), provided that the distinctive features of each phase have been previously identified [87].

The chemical composition and structural type of these crystals are referred to as their "phases." Materials can be mixtures composed of one or more phases and may contain both crystalline and non-crystalline components. In an X-ray diffractometer, different crystalline phases produce distinct diffraction patterns.

Phase identification can be accomplished by comparing X-ray diffraction patterns obtained from unknown samples to those in reference databases. This process is akin to comparing fingerprints in a crime scene investigation. The most comprehensive compound database is managed by the ICDD (International Center of Diffraction Data) [88].

Powder X-ray diffraction (XRD) analysis was conducted using a BRUKER AXS D8 ADVANCE diffractometer, equipped with a copper anode tube providing Cu Kα radiation (λ = 1.5406 Å) and a graphite monochromator. The instrument operated at 40 kV and 40 mA with a scanning speed of 0.2° per second. XRD patterns for all samples were recorded within the 2θ range of [10°-90°].

2.2. Fourier-transform infrared spectroscopy (FTIR):

FTIR, is a non-destructive method used to obtain the absorption spectrum of solid, liquid, or gas samples. Due to historical conventions, infrared light in spectroscopy is often described in terms of wavenumbers rather than wavelengths. Wavenumbers indicate the number of wavelengths per unit distance and are expressed in cm^{-1}. Infrared radiation (IR) falls within the frequencies range of (4000 - 400 cm^-1), corresponding to the molecular vibration energy domain.

Infrared light can be categorized into three regions: near-infrared (NIR), mid-infrared (MIR), and far-infrared (FIR). NIR exhibits the shortest wavelength with higher wavenumbers, whereas FIR possesses the longest wavelength with lower wavenumbers. As molecules absorb photons of infrared radiation, they undergo internal vibrational movements, such as stretching and bending. This absorption allows us to identify characteristic atomic groupings.

This method has replaced traditional infrared spectroscopy due to its ability to simultaneously analyze all wavelengths of IR light using an interferometer, resulting in faster measurements

and enhanced accuracy with a superior signal-to-noise ratio. Despite producing a distinct dataset, FTIR data can be converted into the familiar IR spectrum through a mathematical operation known as Fourier transform.

The Infrared Spectrum expresses absorbance (or transmittance) relative to the frequency of the incident ray. This spectrum is specific to the molecules present in the sample, acting as a distinctive fingerprint. The characteristic peaks in this spectrum allow for comparison with a database [89, 90].

Fourier-Transform Infrared (FTIR) spectra were obtained using a Bruker Vertex 77v spectrometer, covering the wavenumber range from 400 to 4000 cm^{-1} with a resolution of 4 cm^{-1}. The spectra were analyzed using Opus software.

2.3. Raman spectroscopy:

Raman spectroscopy is a non-destructive technique employed in analyzing molecular structures and serves as a complementary method to infrared spectroscopy. The term "Raman" originates from the Indian physicist Chandrasekhara Venkata Raman, who is credited with its discovery.

The Raman technique involves focusing a monochromatic light beam onto the sample under study and analyzing the scattered light. This light is collected using lens and analyzed by a spectrometer.

The process of Raman scattering is initiated when photons interact with a molecule, leading to a virtual elevation in its energy potential. This heightened energy level can manifest in various ways. A large portion of the scattered photons do not change wavelength; they maintain the same energy. In this scenario, there is no exchange of energy between the photons and the atoms in the medium. This phenomenon is referred to as elastic scattering or Rayleigh scattering.

The phenomenon involves a small portion of the photons, 1/1000000, which are scattered with a different wavelength. In this case, the photons exchange energy with the electrons of the sample's atoms. This is the Raman effect. It is also referred to as inelastic scattering.

The results of Raman spectroscopy measurements are graphically represented in the form of Raman spectra. The y-axis represents the intensity of scattered light, while the x-axis represents the energy (frequency) of light. Since the focus is on the frequency shift of the scattered light

by Raman, the frequencies on the x-axis are represented relative to those of the laser. The x-axis thus corresponds to the Raman shift (expressed in cm^{-1}) [91, 92].

Raman spectra were recorded at room temperature using a Horiba Jobin Yvon LabRAM Aramis confocal Raman spectrometer, which is equipped with a cooled CCD camera and an automated XYZ stage. The samples were exposed to laser excitation at 532 nm with a D2 filter, delivering a laser power of 0.33 mW to the surface.

2.4. X-ray photoelectron spectroscopy (XPS):

XPS is now the most widely applied method of surface analysis, providing both qualitative and quantitative information about the chemical composition of surfaces and the nature of chemical bonds. All elements except hydrogen and helium are detectable using this method. It is a non-destructive analysis technique conducted under ultra-high vacuum conditions, allowing for the probing of the first few nanometers of the sample's surface. XPS primarily yields information on the relative proportions of elements present in the outermost atomic layers and their oxidation states [93].

Photoelectron spectroscopy is based on the principle of the photoelectric effect. When a material is irradiated with a monochromatic X-ray source, core electrons are ejected from the atom and traverse the material. By measuring the kinetic energy of the emitted photoelectrons, one can deduce the binding energy of the electron before photoemission. Additionally, this energy is characteristic of the energy levels of the electronic layers of the elements and can provide valuable insights into the electronic properties of the surface.

The resulting spectra are obtained through Survey XPS analysis, serving as a tool for identifying and quantifying the elements present on a surface. Moreover, high-resolution XPS analysis is conducted to obtain more detailed chemical state information from peak position and peak shape. It is typically necessary to first confirm which elements are present by conducting a survey XPS analysis, as XPS utilizes narrow energy ranges scanned under high-energy resolution conditions [94].

To determine the chemical composition and valence states of each element in the prepared samples, a Thermo Scientific K-Alpha X-ray photoelectron spectrometer (XPS) equipped with a hemispherical analyzer and monochromatized Al Kα radiation (1486.6 eV) was employed. The binding energies were calibrated by setting the C1s peak to 284.6 ± 0.2 eV relative to the

Fermi energy level. Peak fitting and asymmetric deconvolutions were carried out using the Advantage software, utilizing a Shirley background and fixing the Lorentzian-Gaussian (L/G) ratio at 30%.

2.5. BET method:

The specific surface area can be determined via the model developed by Brunauer, Emmett, and Teller in the 1940s, or the BET method, based on the adsorption and desorption properties of gases on the surface of a solid. Adsorption is a surface phenomenon whereby gas molecules (adsorbate) can reversibly attach to the surface of a solid through weak or secondary interactions, typically Van der Waals forces (physisorption) or chemical bonds (chemisorption) mainly at low temperatures. The reverse phenomenon, desorption, results notably from an increase in temperature and a decrease in pressure [95].

The specific surface area denotes the total surface area per unit mass of the product accessible to atoms and molecules, encompassing the entire surface of each particle, including open porosity [96].

Formation of a monomolecular layer on the surface is used to determine the specific surface area, while capillary condensation can be used to assess pore volume and pore size distribution. Prior to analysis, the sample is pretreated at high temperature under vacuum or under circulating gas to eliminate any contaminants [97].

Brunauer-Emmett-Teller (BET) analysis was conducted to assess the physical adsorption and desorption of gas molecules on the solid surfaces of our products. The measurements were performed using a Tristar system (Micromeritics, ASAP 2420) with nitrogen gas as the adsorbate at its liquid temperature. Prior to analysis, the samples were degassed overnight under vacuum at room temperature to eliminate impurities and prevent any transformation of the products. The specific surface area (SSA) and pore size distribution were determined from the nitrogen sorption isotherms and calculated using the Barrett-Joyner-Halenda (BJH) method, respectively.

2.6. UV, visible spectroscopy:

UV-visible absorption spectroscopy is a widely utilized technique in laboratory settings. It relies on the fundamental property of molecules to absorb light radiation at distinct wavelengths. When monochromatic light traverses through an absorbing solution of concentration C confined within a cuvette of thickness l, a fraction of this radiation is absorbed by the sample while the remainder is transmitted. Bouguer, Lambert, and Beer extensively investigated the correlations between I_0 and I: the intensity of monochromatic light passing through a medium where it is absorbed decreases exponentially:

$$I = I_0 e^{-k\,L\,C} \qquad \text{(Eq. 7)}$$

- I_0 is the intensity of incident light
- I is the intensity after passing through the cuvette containing the solution (transmitted intensity)
- l is the distance traveled by light (cuvette thickness) (in cm)
- C is the concentration of absorbing species
- k is a constant characteristic of the sample.

This equation can be rewritten as $\log(I_0/I) = k\,l\,C/2.3 = \varepsilon\,l\,C$ (Eq. 8)

- $\log(I_0/I)$ is called absorbance (A)
- $I/I_0 = T$ is the transmission
- T % is the transmittance
- ε is the molar extinction coefficient; it is a characteristic of the substance studied at a given wavelength. If C is the molarity, ε is in $L.mol^{-1}.cm^{-1}$.

Then we obtain the relation known as Beer-Lambert's law:

$$A = -\log T = \varepsilon l C \qquad \text{(Eq. 9)}$$

The absorption band, observed in the UV-visible domain, is characterized by its position in wavelength λmax, nm (or in wavenumber, cm-1).

The position of the maximum absorption corresponds to the wavelength of the radiation that induces the electronic transition. As for the intensity, it can be shown that it is related to the dipole moment. Its value allows us to determine whether the transition is allowed or forbidden [98].

Optical band gap energy (Eg):

The energy separating the valence band Ev from the conduction band Ec is precisely defined by the energy (Ec - Ev) which corresponds to the energy of the bandgap (Eg). Generally, determining the type of transition of the bandgap in synthesized nanomaterials can be obtained by using the Tauc formula which is expressed as

$$(\alpha h\nu)^n = B\,(h\nu - Eg) \qquad \text{(Eq. 10)}$$

where

α is the absorption coefficient, B is a constant, Eg is the optical band gap and hν is the photon energy. This absorption coefficient value α (ν) is determined from the following expression (α(ν) = 2.303A/t); where A is obtained from the UV-Vis spectra (Fig. 9 a,b).

By plotting Tauc's graphs, correlating $(\alpha\hbar\nu)^2$ against the photon energy ($\hbar\nu$), and extrapolating the linear section of these plots, one can determine the optical band gap (Eg) values at

$(\alpha\hbar\nu)^2 = 0$ [99].

The optical absorbance properties were measured using a GENESYS™ 10S UV–Vis spectrophotometer, covering a spectral range of 190 to 1100 nm at room temperature with a wavelength precision of 1 nm. This analysis was conducted to determine the band gap energies of the products dispersed in deionized water (DI).

2.7. Scanning electron microscopy (SEM):

SEM is a microscopy technique based on the principle of electron-matter interactions. A beam of electrons scans the surface of the sample to be analyzed, which in turn emits certain particles in response. Various detectors are used to analyze these particles and reconstruct an image of the surface.

In conventional optical microscopy, visible light interacts with the sample, and the reflected photons are analyzed by detectors or by the human eye. In electron microscopy, the light beam is replaced by a beam of primary electrons that strikes the surface of the sample, and the re-emitted photons are replaced by a spectrum of particles or radiations: secondary electrons, backscattered electrons, Auger electrons, or X-rays. These different particles or radiations provide various types of information about the material composing the sample [100].

A scanning electron microscope is essentially composed of an electron gun and an electron column, which function to generate a fine electron probe on the sample, a specimen stage allowing movement of the sample in three directions, and detectors for detecting and analyzing radiations emitted by the sample. Additionally, the apparatus must necessarily be equipped with a vacuum pump system.

A fine electron probe is projected onto the sample for analysis. The interaction between the electron probe and the sample generates low-energy secondary electrons, which are accelerated towards a secondary electron detector that amplifies the signal. At each point of impact, an electrical signal is thus produced. The intensity of this electrical signal depends on both the nature of the sample at the point of impact, which determines the yield of secondary electrons, and the topography of the sample at the point in question. By scanning the beam over the sample, it is possible to obtain a map of the scanned area.

In 1960, the invention of a new detector by Thomas Eugene Everhart and RFM Thornley accelerated the development of the scanning electron microscope: the Everhart-Thornley detector. Highly efficient in collecting secondary electrons as well as backscattered electrons, this detector became very popular and found its way into nearly every SEM [101, 102].

The morphology of the products was examined using a Field Emission Scanning Electron Microscope (FE-SEM), specifically the JEOL 6700-FEG and JEOL 7500F models, which operated at varying voltages (3-15 kV) and a current of 20 µA. The microscope was equipped with an Energy Dispersive X-ray spectroscopy (EDX) system, enabling both qualitative and quantitative analyses. This setup was employed to assess the quality, purity, selectivity, and shape-dimension of the multi-structures formed under different synthesis conditions. For the FE-SEM analysis, the products were directly affixed to the sample holder using graphite paste.

2.8. Transmission electron microscopy (TEM):

TEM is a powerful imaging technique that utilizes a high-energy electron beam to examine ultrathin specimens. Electron-sample interactions generate signals that are converted into images capable of sub-nanometer resolution. The ability to combine high-resolution imaging with diffraction and elemental analysis makes TEM a versatile tool for materials science, nanotechnology, and biology.

TEM was pioneered by Max Knoll and Ernst Ruska in 1931, with Ruska subsequently awarded the Nobel Prize in Physics for this groundbreaking work. TEM involves transmitting a high-energy electron beam through an ultrathin specimen. Electromagnetic lenses focus the transmitted electrons onto a detector, generating an image. For crystalline samples, diffraction patterns can be obtained. TEM's applications span across various fields, from biological structures to materials analysis [103].

There are two main modes of operation for a transmission electron microscope. Imaging mode: The electron beam interacts with the sample based on its thickness, density, or chemical composition, resulting in a contrast-rich image in the image plane. By placing the detector in the image plane, a transmission image of the observed area can be obtained [104].

Diffraction mode capitalizes on the wave-like behavior of electrons. Upon interacting with a crystalline sample, the electron beam undergoes diffraction, dispersing its intensity into multiple beams oriented in specific directions due to constructive interference. These diffracted beams are subsequently recombined using magnetic lenses to form the final image [105].

The high-resolution transmission electron microscopy (HRTEM) analyses were conducted using a Philips Tecnai 10 microscope, operating with an emission current of 5 µA and an accelerating voltage of 80 kV. To prepare the samples, the nanomaterial was dispersed in ethanol, and the resulting suspension was deposited onto a carbon-coated copper grid.

2.9. Electrochemical investigation:

Electrochemical methods allow for the acquisition of thermodynamic and kinetic information regarding the insertion or absorption reactions involved in electrochemical processes. Numerous parameters can be accessed, such as working potential, equilibrium potential, entropy variation, specific capacity, electrochemical reversibility, diffusion kinetics, ionic conductivity, cycle life, and the impact of current density.

An electrochemical system consists of an electronic conductor and an ionic conductor. The electronic conductor is often referred to as an electrode, and the ionic conductor is often called an electrolyte. The interface between the two conductors is known as the electrode-electrolyte interface.

An electrochemical reaction is a heterogeneous charge transfer reaction that occurs at the interface of two conductors. It involves molecules, atoms, ions, and electrons and corresponds to a change in conduction mode [106].

Electrochemical characterization was conducted in a three-electrode cell using a 6 M KOH aqueous electrolyte at ambient temperature. A platinum counter electrode and a saturated calomel reference electrode (SCE) were employed. Cyclic voltammetry was performed within a potential window of 0 to 0.6 V at scan rates ranging from 5 to 100 mV/s to evaluate electrochemical reversibility and assess potential applications in energy storage. Galvanostatic charge-discharge measurements were carried out at current densities between 1 and 100 A/g to determine specific capacity and rate capability. Electrochemical impedance spectroscopy was conducted over a frequency range of 1 Hz to 100 kHz at open circuit potential to analyze the electrochemical behavior, including charge transfer resistance and internal resistance, of the Ni/Mn nanomaterials. Gravimetric specific capacitance (Cs, F/g) and specific capacity (Qs, mAh/g) values were determined for the prepared electrodes through analysis of cyclic voltammetry (CV) and galvanostatic charge-discharge (GCD) curves, respectively, using established equations:

(From **CV curves**): $Cs = \frac{\int IdV}{m\nu\Delta V}$ …… (Eq. 11)

Where m represents the mass of the electroactive material (g), ν denotes the scan rate (mV/s), ΔV corresponds to the potential window (Vc - Va), and ∫IdV signifies the integrated cathodic current of the cyclic voltammogram (mA·V).

(From **CP curves**): $Qs = \frac{I\Delta t_D}{3.6\,\Delta V}$ …… (Eq. 12)

Where $i = \frac{I}{m}$ represents the current and m denotes the mass of the active material, while Δt_D signifies the discharge time.

To assess the electrochemical surface area of the synthesized Ni/Mn materials with varying compositions, structures, and morphologies, cyclic voltammetry (CV) was employed using a 1 mM $K_4Fe(CN)_6$ solution in 6 M KOH. The oxidation of ferrocyanide at the working electrode surface (bare nickel foam and nickel foam coated with nanomaterials) was investigated:

$[Fe(CN)_6]^{-4} \xrightarrow{oxidation} [Fe(CN)_6]^{-3}$ …….. (Eq. 113) [107]

Conclusion

This chapter outlined the experimental methodology used to synthesize Ni/Mn-based nanomaterials in various ratios (0/1, 1/0, 1/1, 1/2, and 2/1) using a cost-effective and straightforward hydrothermal technique. These nanomaterials were subsequently evaluated as potential electroactive components for electrochemical energy storage applications, with a focus on supercapacitors.

We began by describing the synthesis process for the nanohybrids, including the specific operating conditions. This was followed by a detailed account of the characterization techniques employed to identify the synthesized nanomaterials. The study examined how several experimental parameters such as precursor ratios and hydrothermal growth temperature, affected the structural, textural, and morphological properties of the resulting nanohybrids. The characterization techniques included X-ray diffraction (XRD), Fourier Transform Infrared spectroscopy (FTIR), Raman spectroscopy, high-resolution field emission scanning electron microscopy (FE-SEM), transmission electron microscopy (TEM) and textural analysis using BET surface area and porosity measurements. Additionally, UV-Vis absorption spectroscopy and X-ray photoelectron spectroscopy (XPS) were used to further analyze the materials. Finally, we discussed the core principles of electrochemical (EC) measurements, which were performed using a three-electrode system with a basic aqueous electrolyte. These measurements were aimed at exploring potential applications in electrochemical energy storage, particularly supercapacitors. The techniques employed included Cyclic Voltammetry (CV), Galvanostatic Charge/Discharge (CD), and Electrochemical Impedance Spectroscopy (EIS).

Chapter 3: Findings and discussion

Introduction

In this chapter, we present the outcomes of our successful experimental study carried out at the Laboratory for the Study and Research of Condensed States (LEREC). In this work, we synthesized nanohybrids of transition metal bimetallic (Ni, Mn) with varying precursor ratios at different synthesis temperatures. This synthesis was performed using a straightforward, cost-effective, and easy-to-implement hydrothermal method. The resulting biphasic nanohybrids were systematically characterized through various analytical techniques to investigate how the optimized experimental parameters of the hydrothermal synthesis process affected their structural, morphological, textural, spectroscopic, and elemental characteristics, as well as their optical properties, which in turn directly influence their subsequent electrochemical performance.

1. Structural properties:

1.1. Identification using X-ray diffraction (XRD):

Employing XRD techniques, we successfully identified the crystal structures of our synthesized products. This study further investigates how two key factors, growth temperature and the stoichiometry of the Ni/Mn precursors, influence the resulting nanostructure. The identification of the synthesized nanostructure was guided by findings reported in the literature [108, 109, 110, 111].

Figure 8 displays the distinctive X-ray diffraction patterns for Ni/Mn-based materials. These materials are produced through a template-free hydrothermal process and feature either single or dual nanostructures. The investigation focuses on materials made up of hydroxyl or carbonate compounds. The X-ray diffraction analysis revealed the presence of three distinct crystalline phases in the synthesized mono- or bi-nanostructures. These phases can be attributed to configurations resembling transition metal hydrotalcite or brucite. Notably, the findings consistently demonstrate the stability of a manganese carbonate ($MnCO_3$) phase across all synthesis conditions that employed manganese-based precursors. This is evidenced by the presence of dominant diffraction peaks corresponding to (012), (104), and (018) indices. These peaks are characteristic of the rhombohedral crystal structure of rhodochrosite (D-$MnCO_3$), with an interlayer spacing of approximately 15 angstroms, consistent with JCPDS card no. [01-0981] [112, 113].

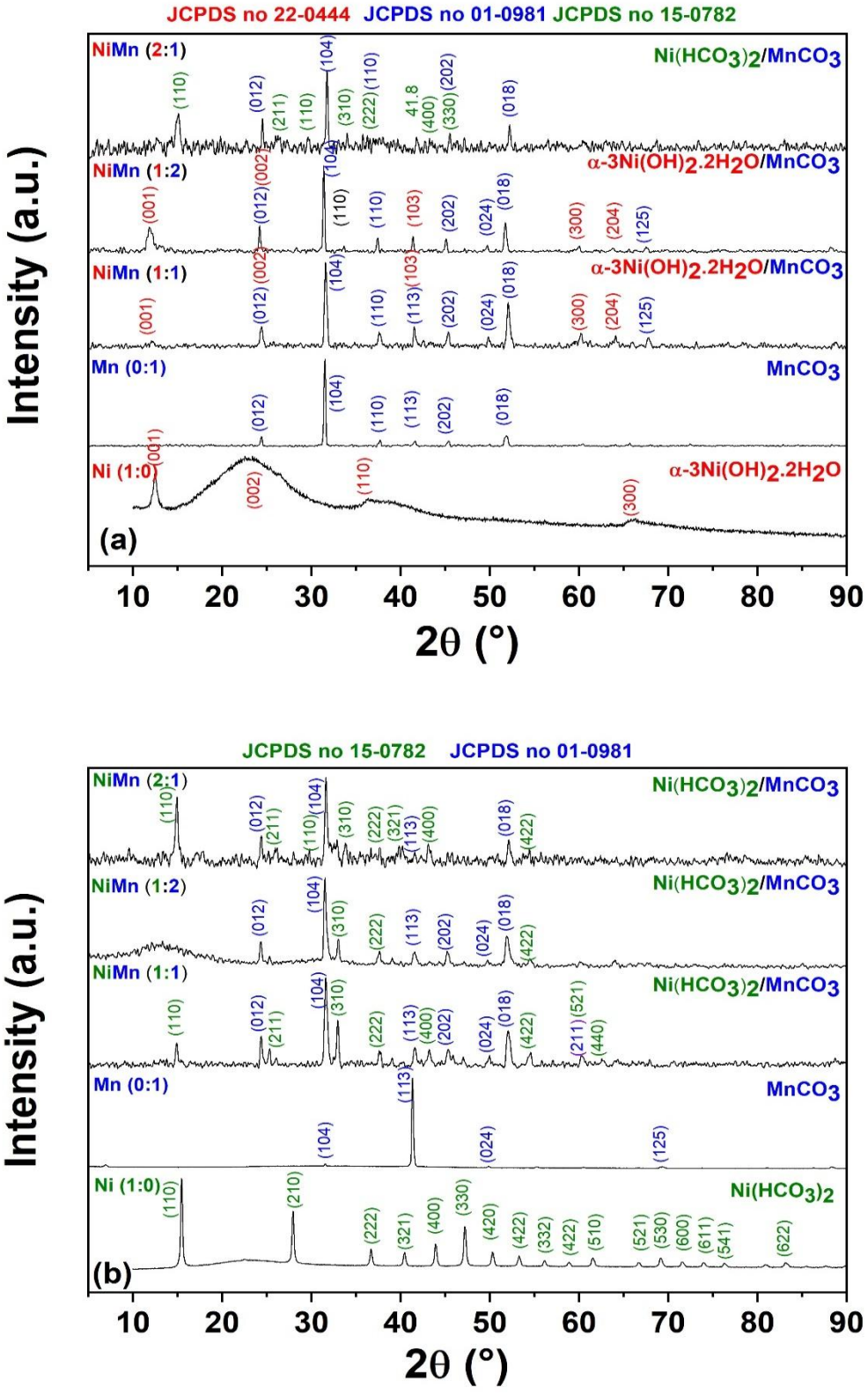

Figure 8: X-ray diffraction (XRD) patterns of nickel-manganese (Ni/Mn) carbonate and/or hydroxide-based nanohybrids synthesized using a template-free hydrothermal process with varying Ni/Mn precursor ratios at two different growth temperatures: (a) 120°C and (b) 180°C.

XRD analysis revealed the presence of two distinct Ni phases in the synthesized products. At a 1:1 (Ni/Mn precursor ratio) and 120°C growth temperature, the characteristic diffraction peaks corresponded to the hexagonal α-3Ni(OH)2·2H2O phase, with an interlayer spacing of approximately 7.5 Å (JCPDS card no. [22-0444]) [114]. Interestingly, for a higher Ni precursor ratio (2:1) and at both 120°C and 180°C growth temperatures, the observed diffraction peaks matched a cubic Ni(HCO3)2 phase with an interlayer distance around 8.38 Å (JCPDS card no. [15-0782]) [115, 116]. Notably, increasing the reaction temperature to 180°C resulted in the complete disappearance of α-3Ni(OH)2 diffraction peaks, accompanied by a rise in Ni(HCO3)2 peaks. This suggests a complete transformation of α-3Ni(OH)2 to the Ni(HCO3)2 phase at the higher temperature.

Our findings suggest that the urea-based synthesis process promotes a phase-transfer reaction between nickel ions and either hydroxide (OH^-) or bicarbonate (HCO_3^-) ions, leading to the formation of two-dimensional nickel-based nanomaterials. During the initial stages at lower temperatures (120°C), the decomposition of urea generates hydroxide ions (OH^-) that react with Ni^{2+} ions to form $Ni(OH)_2$ nanosheets. However, at higher temperatures or with increased Ni^{2+} concentration, bicarbonate ions (HCO_3^-) – produced through the more challenging hydrolysis of CO_2 compared to NH_3 – become more prevalent. These HCO_3^- ions then react with the pre-existing Ni(OH)2 nanosheets, driving a complete transformation into $Ni(HCO_3)_2$ nanosheets. Interestingly, the observed increase in the reaction solution's pH with increasing hydrothermal temperature aligns with this proposed phase transition.

Our calculations based on the Scherrer formula [117] revealed average crystallite sizes of [23–44 nm], [14–28 nm], and [22–27 nm] for MnCO3, α-3Ni(OH)2.H2O, and Ni(HCO3)2 phases, respectively (detailed data in Table 1). These X-ray diffraction (XRD) results suggest the formation of hierarchical NiMn layered double hydroxide (LDH) bistructures. This indicates a successful synthesis of high-purity materials with a desired combination of Ni and Mn, along with well-defined interlayers. **Table 1** provides a summary of the calculated crystalline parameters for these Ni/Mn nanostructures. Notably, the obtained values closely match those reported in reference data and previous literature, signifying good agreement.

Table 1: presents the calculated unit cell parameters for the synthesized Ni/Mn nanohybrids.

Ni/Mn Ratio	Phase/Reference carde	Crystallinity Degree (%)	Crystalline Parameters 'Å' (Calculated)
6h / 120 °C			
(2.1)	[01-0981] $MnCO_3$ [15-0782] $Ni(HCO_3)_2$	**18**	a = 4.71, c = 15.49 a = 8.27
(1.2)	[01-0981] $MnCO_3$ [22-0444] α-$3Ni(OH)_2 \cdot 2H_2O$	**34**	a = 4.88, c = 15.49 a = 5.00, c = 7.58
(1.1)	[01-0981] $MnCO_3$ [22-0444] α-$3Ni(OH)_2 \cdot 2H_2O$	**33**	a = 4.79, c = 15.49 a = 5.54, c = 7.35
(0.1)	[01-0981] $MnCO_3$	**31**	a = 4.79, c = 15.53
(1.0)	[22-0444] α-$3Ni(OH)_2 \cdot 2H_2O$	**08**	a = 5.28, c = 7.19
6h / 180 °C			
(2.1)	[01-0981] $MnCO_3$ [15-0782] $Ni(HCO_3)_2$	**17**	a= 4.81, c = 15.42 a = 8.43
(1.2)	[01-0981] $MnCO_3$ [15-0782] $Ni(HCO_3)_2$	**27**	a = 4.75, c = 15.57 a = 8.55
(1.1)	[01-0981] $MnCO_3$ [15-0782] $Ni(HCO_3)_2$	**35**	a = 4.75, c = 15.57 a = 8.43
(0.1)	[01-0981] $MnCO_3$	**53**	a = 4.82, c = 15.37
(1.0)	[15-0782] $Ni(HCO_3)_2$	**42**	a = 8.13

[01-0981] $MnCO_3$ (a= 4.688 Å, c = 15.524 Å); [22-0444] α-$3Ni(OH)_2 \cdot 2H_2O$ (a = 5.34 Å, c = 7.5 Å); [15-0782] $Ni(HCO_3)_2$ (a = 8.383 Å)

1.2. Identification using Fourier Transform Infrared (FTIR) spectroscopy:

FTIR analysis was employed to further characterize the synthesized products and confirm their crystalline identity. The resulting spectra, presented in **Figure 9**, reveal several characteristic vibration bands. Common peaks observed in the ranges [1367-1398 cm^{-1}], [1068-1074 cm^{-1}], [821-862 cm^{-1}], and at 723 cm^{-1} can be attributed to the ν_3, ν_1, ν_2, and ν_4 vibrational modes of CO_3^{2-} carbonate ions, respectively. These bands likely correspond to carbonate species residing within the interlayer spaces of the LDH structure in the as-synthesized materials [118, 119, 120]. An additional minor peak at 1795 cm^{-1} is tentatively assigned to the C–O group within $MnCO_3$ [119, 121] or potentially a combination band involving carbonate groups and divalent metal cations [118]. Supporting the observed interlayer spacing, previous studies have shown that CO_3^{2-} intercalated LDHs exhibit stronger interlayer interactions compared to those intercalated with other anions [109]. This enhanced interaction can lead to a decrease in the interlayer distance.

The peak observed around 2245 cm^{-1} can be attributed to a residual cyanate vibration mode, likely arising from incomplete urea decomposition during synthesis. This band is absent in the

spectra of samples prepared at 180 °C, suggesting that higher temperature promotes more effective urea decomposition [122].

FTIR analysis further supports the XRD findings. The weak peak observed at 1627 cm^{-1} in samples synthesized at 120 °C with Ni/Mn precursor ratios of 1/0, 1/1, and 1/2 suggests the presence of hydroxyl groups (–OH) from both the brucite-like layers and interlayer water molecules [108, 123, 124]. Additionally, the band at 3645 cm^{-1} in some samples might indicate the O–H stretching vibration within the interlayer of bi-phasic structures, further supporting the formation of α-3Ni(OH)2·2H2O [110, 124]. The broad band observed in the range of [3376–3452 cm^{-1}] can be attributed to OH/H2O present within the brucite-like structure, which is absent in samples prepared at 180 °C [108, 110, 125, 126]. Notably, the peak at the lower wavenumber range of [632–638 cm^{-1}] can be assigned to the vibration mode of metal hydroxides (M-OH/M-O/O-M-O/M-O-M), potentially involving Ni–OH or Mn–O, as reported previously [108, 123–126]. These observations, particularly the presence of abundant hydrophilic hydroxyl groups and carbonate ions, corroborate the XRD results and likely contribute to enhanced wettability between the nanohybrids and the electrolyte.

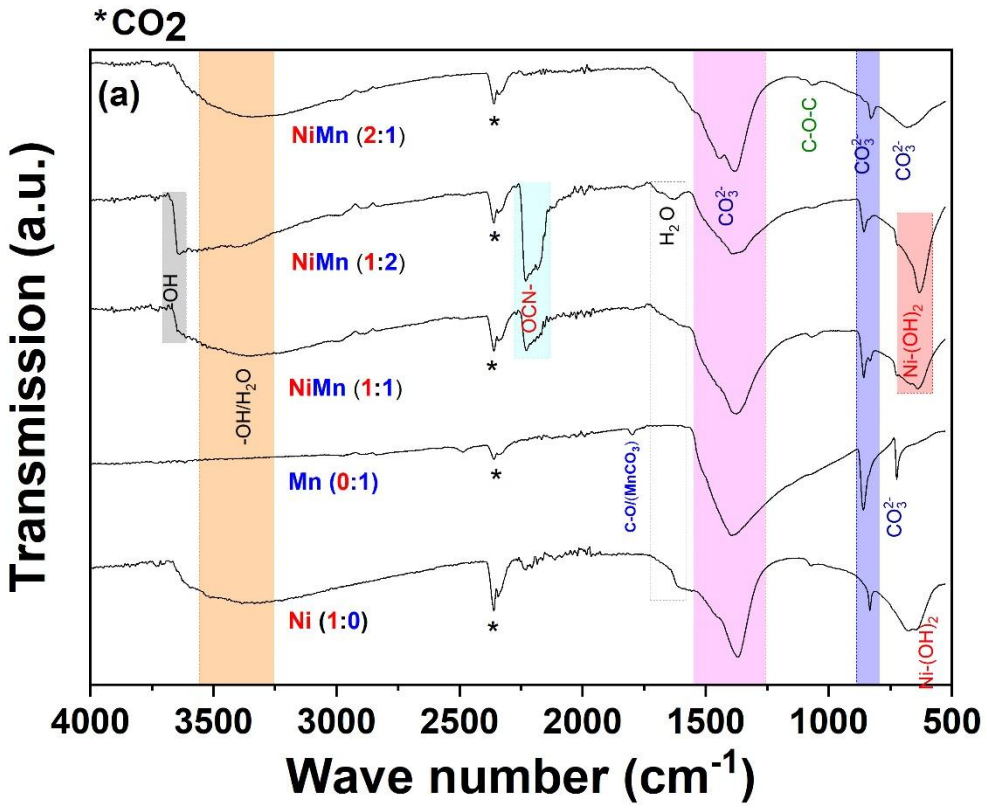

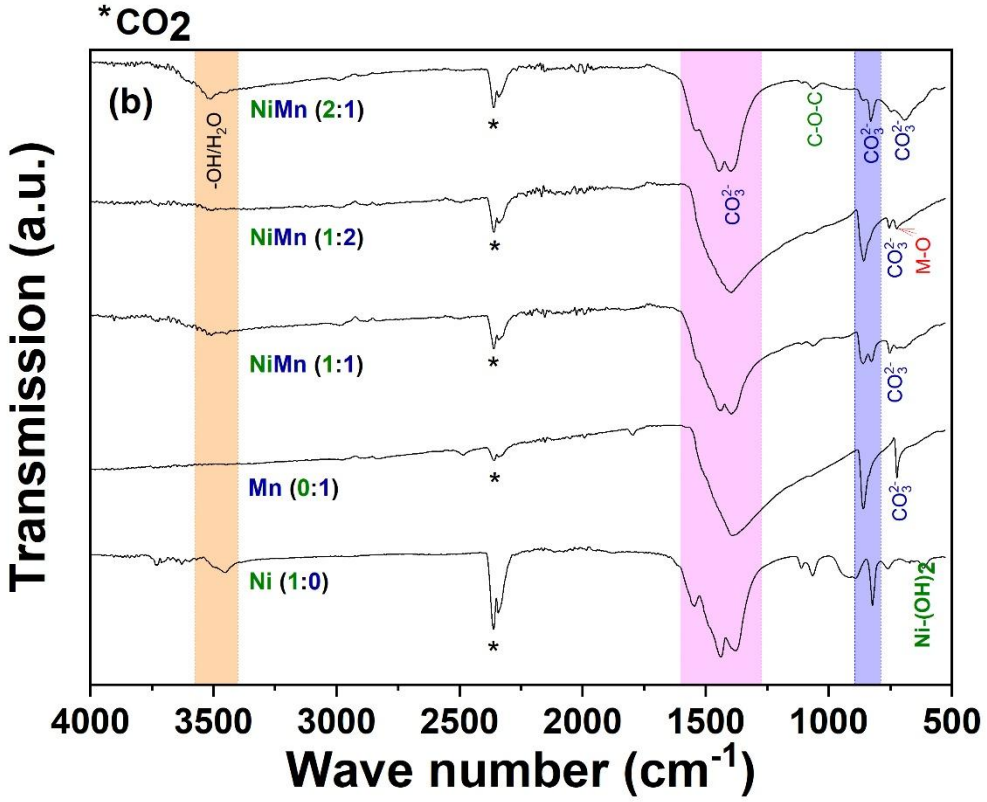

Figure 9: FTIR spectra of Ni/Mn-based nanohybrids synthesized at (a) 120 °C and (b) 180 °C with varying precursor ratios.

1.3. Identification using Raman spectroscopy:

Raman spectroscopy was employed to complement the FTIR analysis and further validate the findings. As illustrated in **Figure 10 a**, the spectra of pure Ni (1/0), Mn (0/1), and Ni/Mn (1/1) precursors exhibit prominent bands around 1085, 717, and 285 cm^{-1}. These bands can be assigned to various vibrational modes of carbonate anions, consistent with previous literature [118, 127]. Additionally, the band observed at approximately 657 cm^{-1} in the spectrum of pure Mn carbonate corresponds to the A1g active mode associated with a symmetric Mn-O stretching vibration [128–131]. Interestingly, a slight shift of this peak towards lower wavenumbers is evident with increasing Ni precursor content. This shift suggests the incorporation of Ni into the crystal lattice.

Furthermore, Raman spectroscopy corroborates the presence of intercalated water molecules and hydroxides in the synthesized nanohybrids. Bands observed around 448, 539, and 445 cm^{-1}, respectively, for the 1/0, 1/1, and 1/2 precursor ratios support this finding [108, 132]. Notably, these bands are absent in the spectra of samples prepared at 180 °C, suggesting the absence of

intercalated water molecules at this higher temperature. Interestingly, the Raman peak positions for the Ni/Mn-based nanohybrids exhibit a systematic deviation from those of pure Ni or Mn precursors. This deviation suggests a potential distortion of the crystal structure and the presence of microscopic stress within the lattice, which could influence the physical and redox properties of the materials. Overall, these Raman spectroscopy results align with the findings from FTIR and XRD, supporting the conclusion that the as-prepared nanohybrids consist solely of mixed phases of $MnCO_3$/α-$Ni(OH)_2$ or $MnCO_3$/$Ni(HCO_3)_2$ without any detectable impurities.

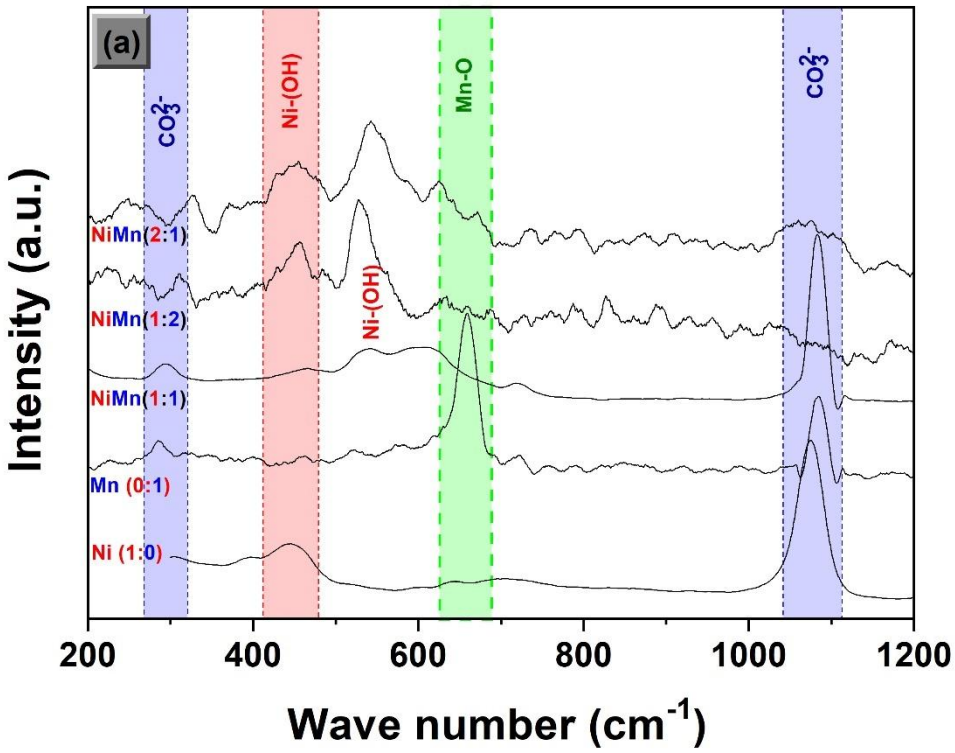

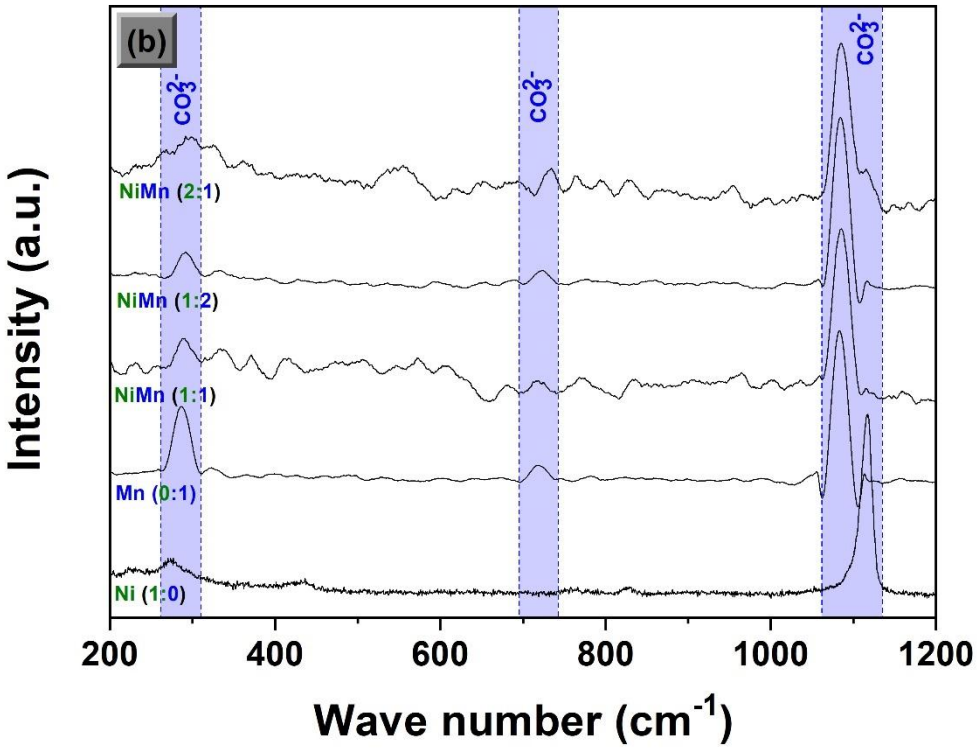

Figure 10: Raman spectra of Ni/Mn-based nanohybrids synthesized at (a) 120 °C and (b) 180 °C with varying precursor ratios.

2. Surface texture and microstructure:

2.1. Surface texture:

FESEM and HRTEM microscopy were employed to characterize the morphology of the synthesized nanohybrids, as shown in **Figure 11**. The images reveal how the morphology varies depending on the initial Ni/Mn precursor ratio and the hydrothermal growth temperature.

FESEM micrographs **Figure 11 a** reveal that $Ni(OH)_2$ nanoprecipitates synthesized with a Ni precursor (1/0) at 120 °C exhibit a flower-like morphology with a diameter of approximately 2 µm. These flower-like structures appear to be composed of centrally arranged nanoneedles. In contrast, samples prepared at 180 °C **Figure 11 a'** display micron and sub-micron sized spherical particles. These particles appear to be agglomerates of various nano shapes, including nano-spheres, nano-cubes, and polyhedral-like structures, with an average size of around 150 nm.

Interestingly, FESEM images **Figure 11 b** and **b'** reveal no significant difference in morphology between pure $MnCO_3$ samples prepared at 120 °C and 180 °C. In both cases, the Mn^{2+} ions appear to readily react with CO_3^{2-} ions, leading to the formation of well-crystallized micro-parallelepiped particles with a near-perfect micro-cubic-like structure. The side lengths of these particles range from 2 to 10 μm, which aligns with the observations reported by Sekhar et al. [121].

Our experiments using an equimolar ratio of Ni to Mn (1:1) at 120°C revealed the formation of layered double hydroxide (LDH) nanosheets. These nanosheets exhibited a high degree of self-aggregation, forming micro/mesoporous structures with a rough surface composed of self-assembled nanopetals. The resulting micro-flower-like morphologies reached sizes of approximately 20 microns, as observed in **Figure 11 c**. Interestingly, at 180°C with Ni/Mn ratios of 1:1 and 1:2, a novel Ni-Mn carbonate structure emerges. This structure consists of uniform, perfect microcubes (1-2 μm) assembled into submicron-sized spheres. These spheres are decorated with nanoneedles approximately 12 nm in diameter, as confirmed by HRTEM **Figure 11 c'** and **e**. The primary composition of these bi-phasic materials appears to be Ni-Mn carbonate. We hypothesize that the rapid nucleation and growth upon precursor mixing might be responsible for the observed particle agglomeration.

Increasing the manganese concentration to a 2:1 ratio (Mn/Ni) at 120°C resulted in the formation of uniformly interconnected, self-assembled nanofilaments. These nanofilaments are densely packed, creating a highly porous network within a micro-quasi-spherical system. Slight aggregation is observed, with an average particle size of 3 μm and an irregular shape **Figure 11 d**.

Increasing the nickel precursor content in the nanohybrid significantly affected the resulting material's structure. At 120°C, for instance, the morphology transitioned from interconnected ultrathin nanoflates (confirmed by HRTEM in **Figure 11 e** for the 2/1 Ni/Mn ratio) to highly mesoporous microspheres (average size ~2 μm) lacking distinct boundaries. This suggests a novel pore arrangement within these clustered microspheres. Interestingly, the addition of more nickel appears to enhance the driving force for nanoflate aggregation. This leads to faster assembly and a decrease in the average thickness of the individual nanoflates within the final material.

These observed morphologies support the presence of a more extensively hydroxylated bi-structural material, aligning well with the previously reported crystalline characteristics

obtained through XRD and FTIR analyses. Interestingly, the product synthesized at 180°C with a Ni/Mn ratio of 2/1 displays a unique sea anemone-like structure. This structure features a hollow core and an outer crust composed of perpendicularly arranged, well-ordered nanoneedles, creating intricate channels and pores. [108].

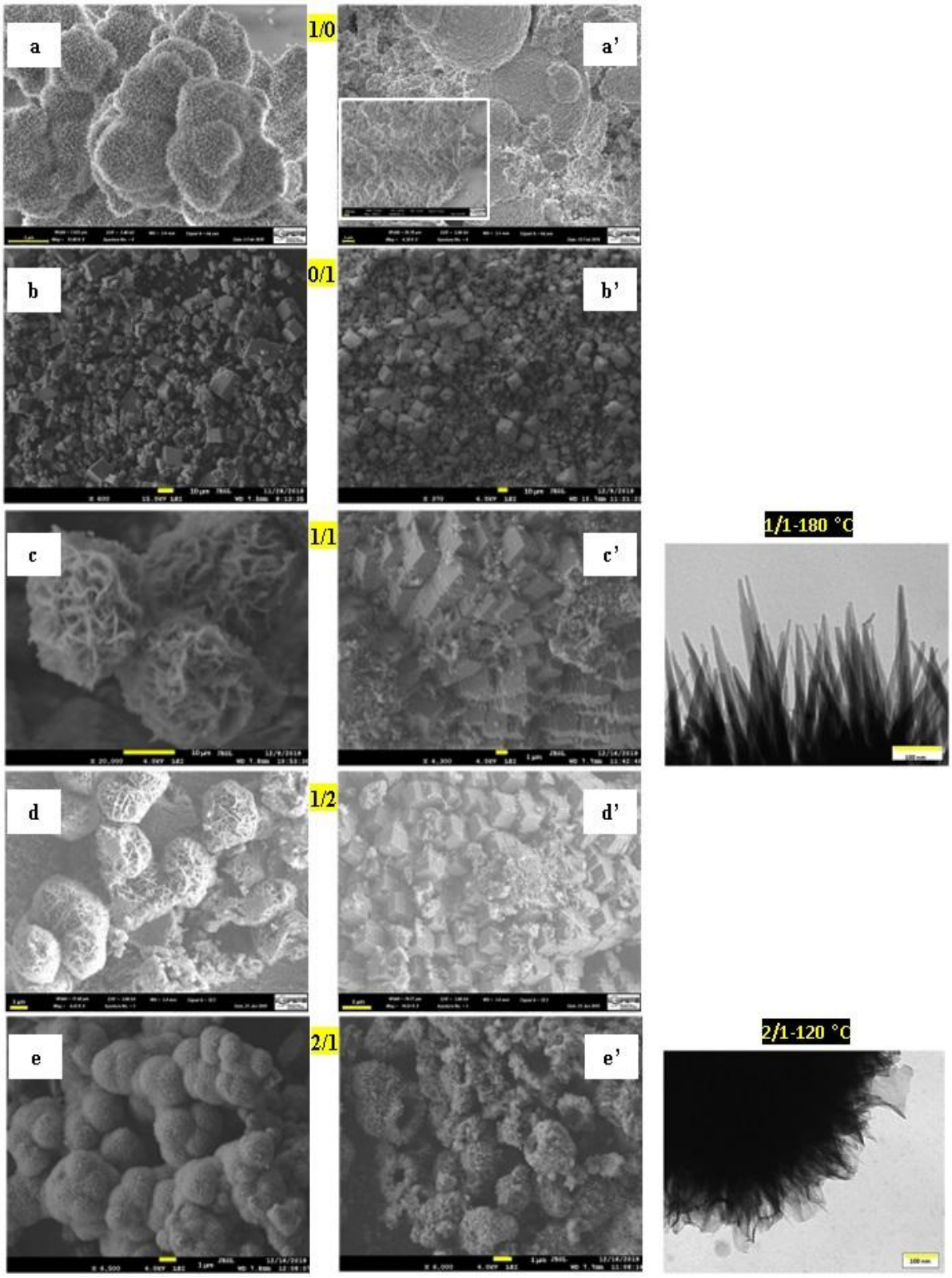

Figure 11: Field-Emission Scanning Electron Microscopy (FESEM) of the synthesized Ni and/or Mn based nanohybrids at different growth conditions (left at 120 ◦C and right at 180 ◦C), with different Ni/Mn precursors ratio, and High-Resolution Transmission Electron Microscopy (HRTEM) Images for two exemplary cases.

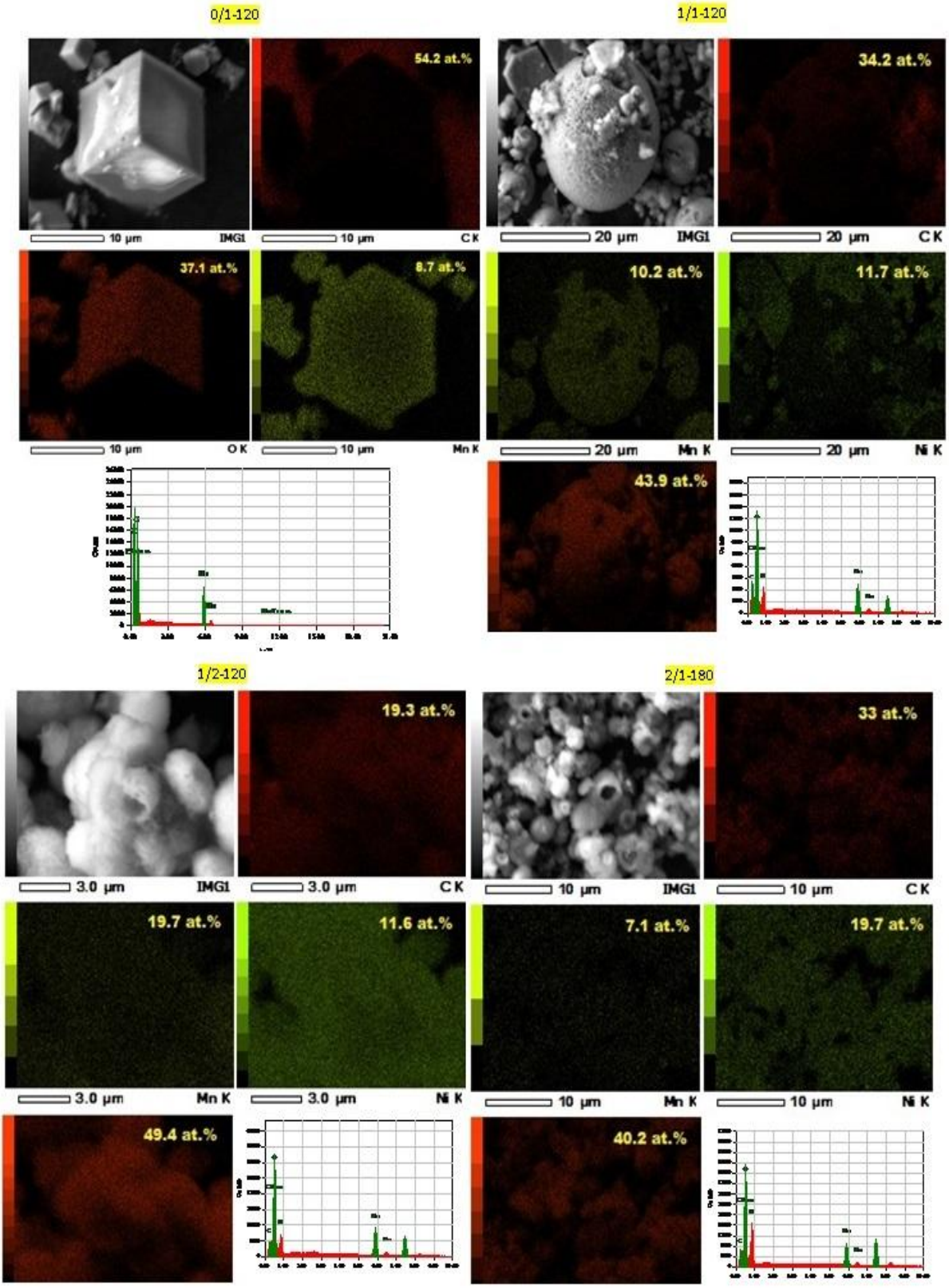

Figure 12: Presents elemental mapping of Material Composition images for four different samples.

As exemplified by the corresponding elemental mapping figures **Figure 12**, the nanohybrid products exhibit a homogeneous distribution of nickel (Ni), manganese (Mn), carbon (C), and oxygen (O) throughout the material.

Advantages of the Novel Ni and/or Mn-Based Micro-Nanosystems:

This work presents a breakthrough in the synthesis of unique micro-nanosystems composed of nickel (Ni) and/or manganese (Mn). These materials, previously unreported, are created through a precisely controlled urea-based hydrothermal synthesis process. This process utilizes optimized parameters, including low temperatures and specific precursor ratios such as 2:1 Ni/Mn or 1:2 Mn/Ni. The resulting materials possess several key advantages that make them highly attractive for various applications (as demonstrated in studies referenced elsewhere, e.g., electrocatalysis [133, 134], energy storage [135, 136], and biosensing [137, 138]).

One significant benefit is the presence of a reduced "dead surface." This refers to a minimized area of the material's surface that remains inactive. By achieving this effect, the overall surface area of the material is significantly enhanced. This increased surface area is particularly advantageous as it allows for a more efficient utilization of the active materials within the system.

Secondly, the three-dimensional structure characteristic of these micro-nanosystems facilitates the transport of charge carriers. These charge carriers travel from the active materials to the current collector, which is crucial for optimal performance in electrochemical applications. Furthermore, the specific structure allows for easier diffusion of ions. These ions travel along shorter pathways to reach the contact area between the electrolyte and the electrode. This improved accessibility of ions further contributes to efficient electrochemical processes.

Thirdly, the presence of a unique nanowire structure is expected to offer several additional benefits. One such benefit is an enhanced electron transport rate, which is essential for efficient electrochemical reactions. Additionally, the nanowire structure is expected to maximize the utilization of the active materials within the system. Ultimately, these factors are expected to significantly improve the overall power performance of devices that utilize these materials.

Finally, the optimized microstructure of these materials likely contributes to a reduction in impedance. This decrease in impedance further enhances the overall electrochemical performance of the system.

2.2. Textural aspect of the resulting products:

The specific surface area (SSA) plays a critical role in the performance of electroactive nanomaterials used for electrochemical energy storage devices [139]. A large surface area with suitable pore size and volume is essential for accommodating a high number of accessible electrochemical active sites that participate in Faradaic redox reactions. To assess the presence of interconnected pores and their potential impact on performance, N2 sorption measurements were conducted [140].

The results presented in **Figure 13** reveal characteristic type-IV isotherms with H3/H2 hysteresis loops at relative pressures (P/P0) ranging from 0.45 to 1 for the optimal Ni/Mn products synthesized at (1/1) 180°C, (2/1) 120°C, and (2/1) 180°C. According to IUPAC classification [84, 141], these features indicate a mesoporous texture, which is beneficial for ion diffusion [136].

Complementary pore size distribution studies performed using the BJH method inset, **Figure 13** confirm the mesoporous nature of the materials. Most pores fall within the 2-50 nm range, further supporting this finding. These results suggest that the hydrothermal synthesis conditions significantly influence the materials' SSA, which ranges from 15 to 85 m2 g-1.

Impact of Morphology on Porosity:

The morphology of the synthesized materials significantly influences their porosity, which plays a crucial role in electrochemical energy storage performance [115, 116, 142]. For instance, the Ni/Mn (2/1) 180°C product exhibits a micro/mesoporous system morphology. This morphology features a ripple-shaped porous network and randomly attached curly nanosheets, as observed through FESEM analysis (refer to earlier Figure). This structure results in a high overall pore volume of approximately 0.14 cm3 g-1 and an average pore diameter of around 10 nm. These pores act as reservoirs for electrolyte ions, significantly reducing the diffusion length for ions within the material. This reduction in diffusion length helps overcome kinetic limitations commonly faced by energy storage materials during Faradaic redox reactions, especially at high rates [143].

In contrast, materials with a nanocube morphology exhibit a significantly lower specific surface area (around 15 m2 g-1) and smaller pore characteristics (volume: 0.1 cm3 g-1, diameter: 13 nm) compared to the optimal morphologies observed in the best performing samples [136].

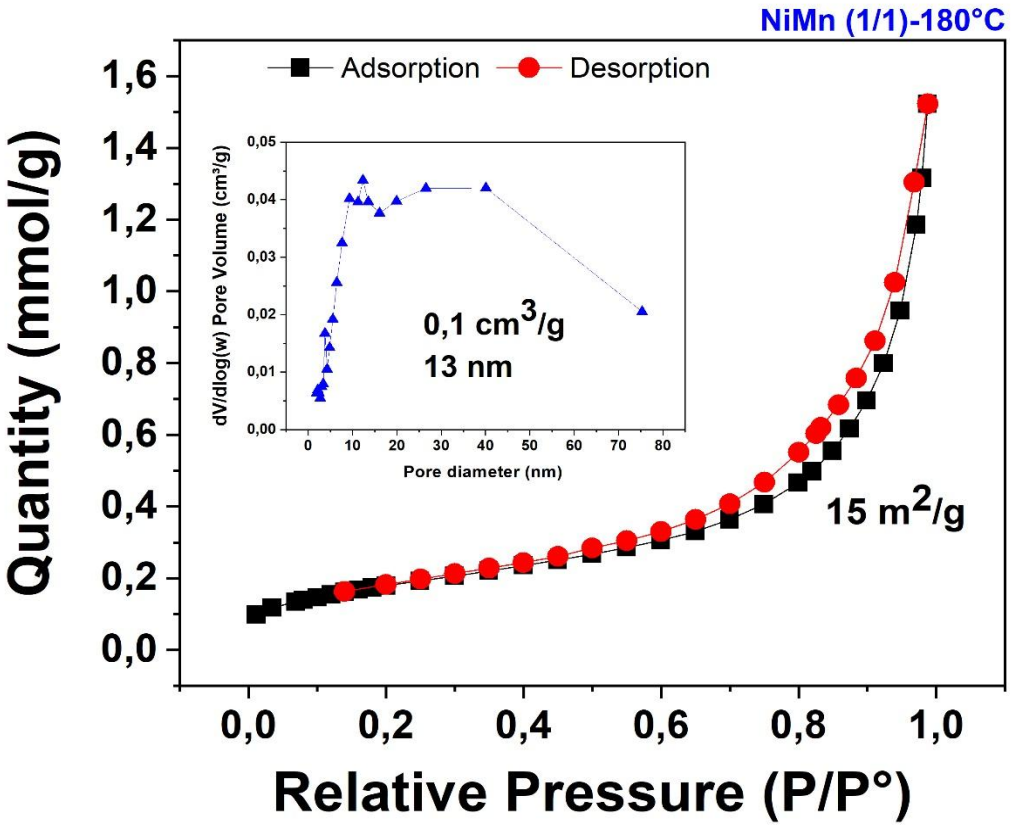
NiMn (1/1)-180°C
Adsorption
Desorption
Quantity (mmol/g)
Relative Pressure (P/P°)
dV/dlog(w) Pore Volume (cm³/g)
Pore diameter (nm)
0,1 cm³/g
13 nm
15 m²/g

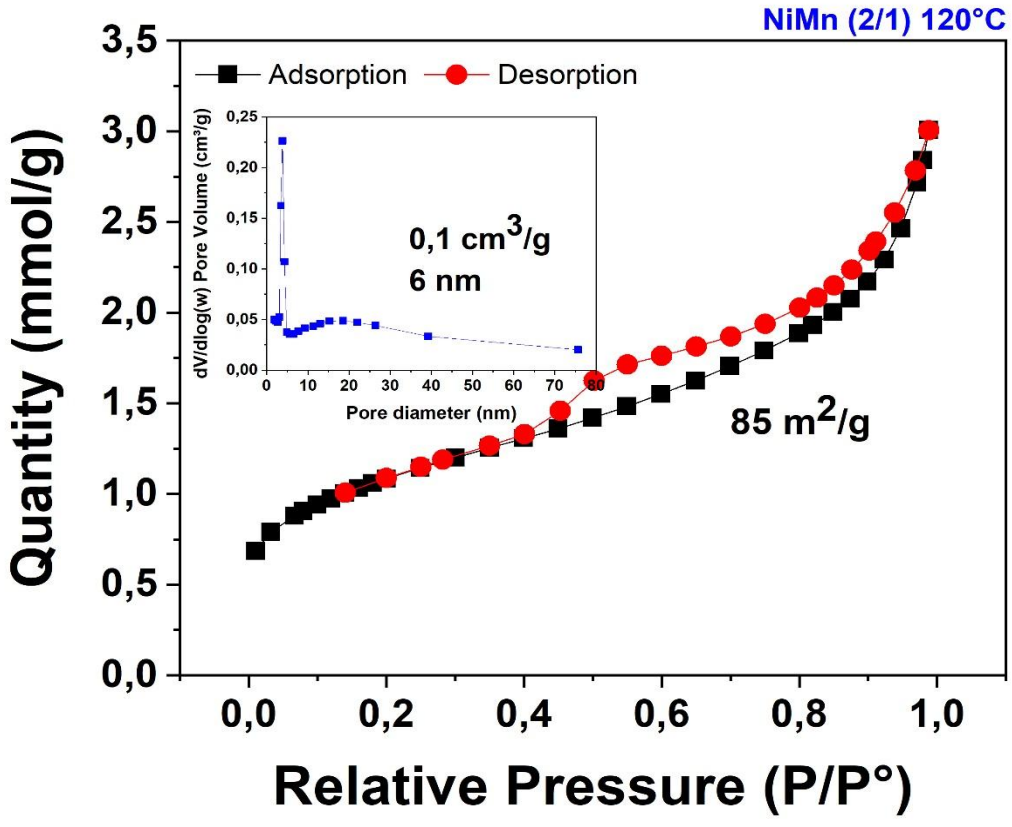
NiMn (2/1) 120°C
Adsorption
Desorption
Quantity (mmol/g)
Relative Pressure (P/P°)
dV/dlog(w) Pore Volume (cm³/g)
Pore diameter (nm)
0,1 cm³/g
6 nm
85 m²/g

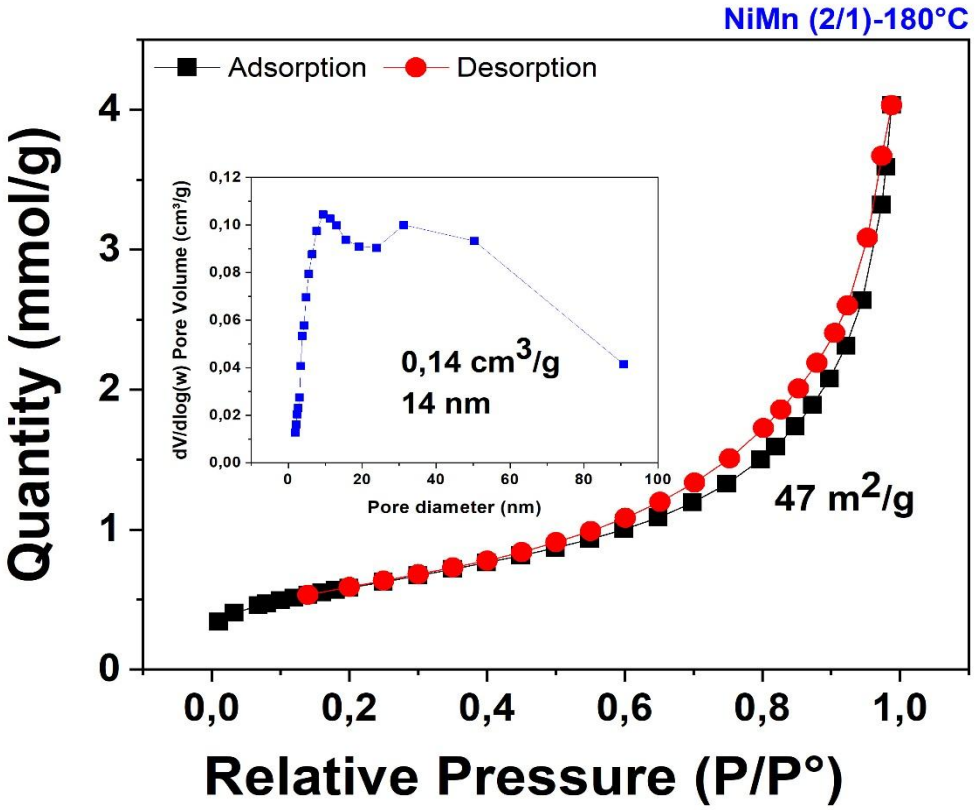

Figure 13: Nitrogen Adsorption-Desorption Isotherms and Pore Size Distribution.

2.3. Identification using XPS Spectroscopic:

To gain deeper insights into the chemical composition and oxidation states of the synthesized Ni/Mn-based nanohybrids, X-ray photoelectron spectroscopy (XPS) analysis was performed. **Figures 14-15-16** present the results for materials prepared under two different growth temperatures and with varying precursor ratios. The full survey scan XPS spectra **Figure 14** reveal the presence of key elements in the nanohybrids, including nickel (Ni 2p), manganese (Mn 2p3/2, 2p1/2, 3p, 3s), carbon (C 1s), and oxygen (O 1s). The relative intensities of these peaks vary slightly across different synthesis conditions, suggesting potential variations in elemental composition. The figures also report the quantified percentages of each element for each synthesis condition.

The presence of new peaks in the XPS spectra, particularly those corresponding to Ni 2p as expected based on prior literature [125, 144], confirms the successful incorporation of nickel into the MnCO3 structure, resulting in the formation of Ni/Mn nanohybrids.

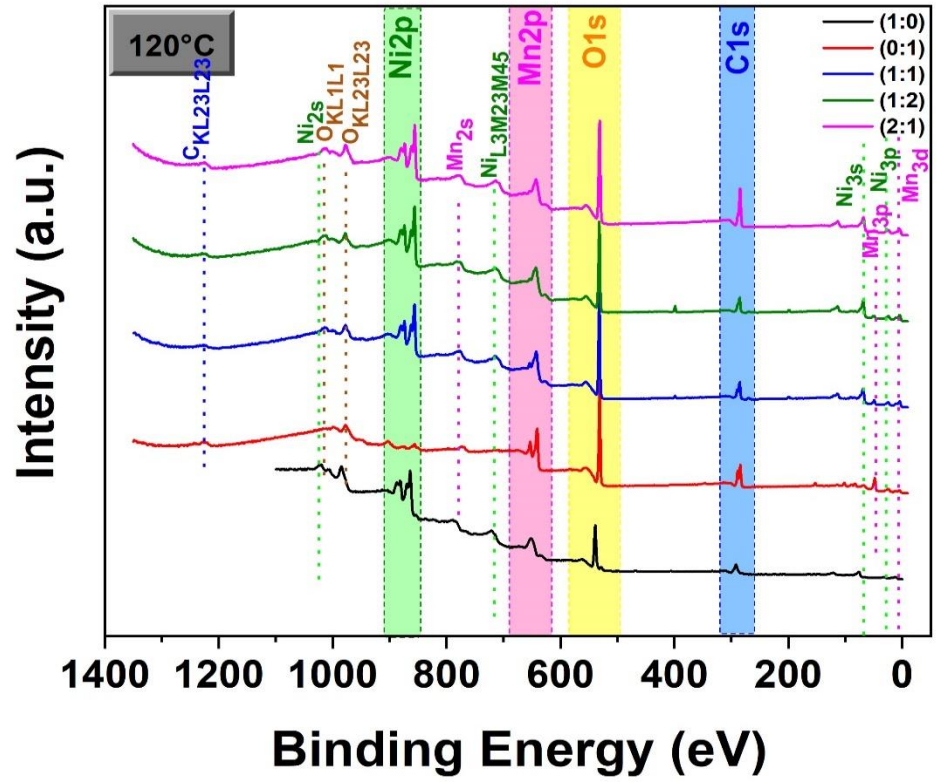
120°C
Ni2p
Mn2p
O1s
C1s
(1:0)
(0:1)
(1:1)
(1:2)
(2:1)
Intensity (a.u.)
1400 1200 1000 800 600 400 200 0
Binding Energy (eV)

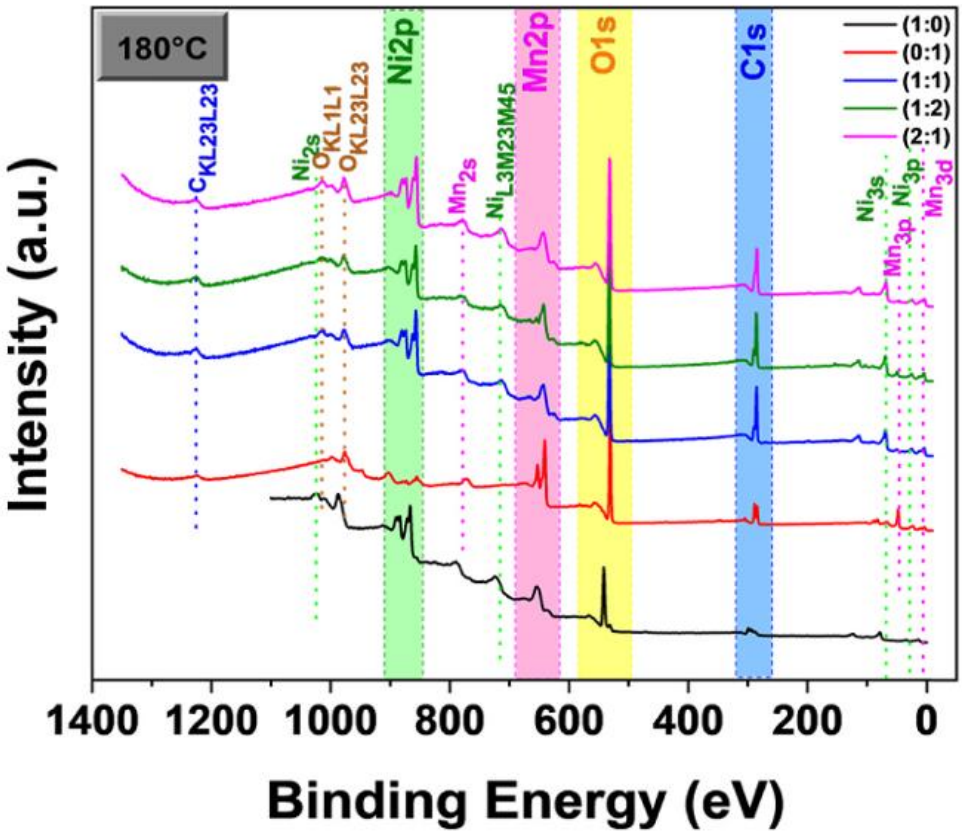
180°C
Ni2p
Mn2p
O1s
C1s
(1:0)
(0:1)
(1:1)
(1:2)
(2:1)
Intensity (a.u.)
1400 1200 1000 800 600 400 200 0
Binding Energy (eV)

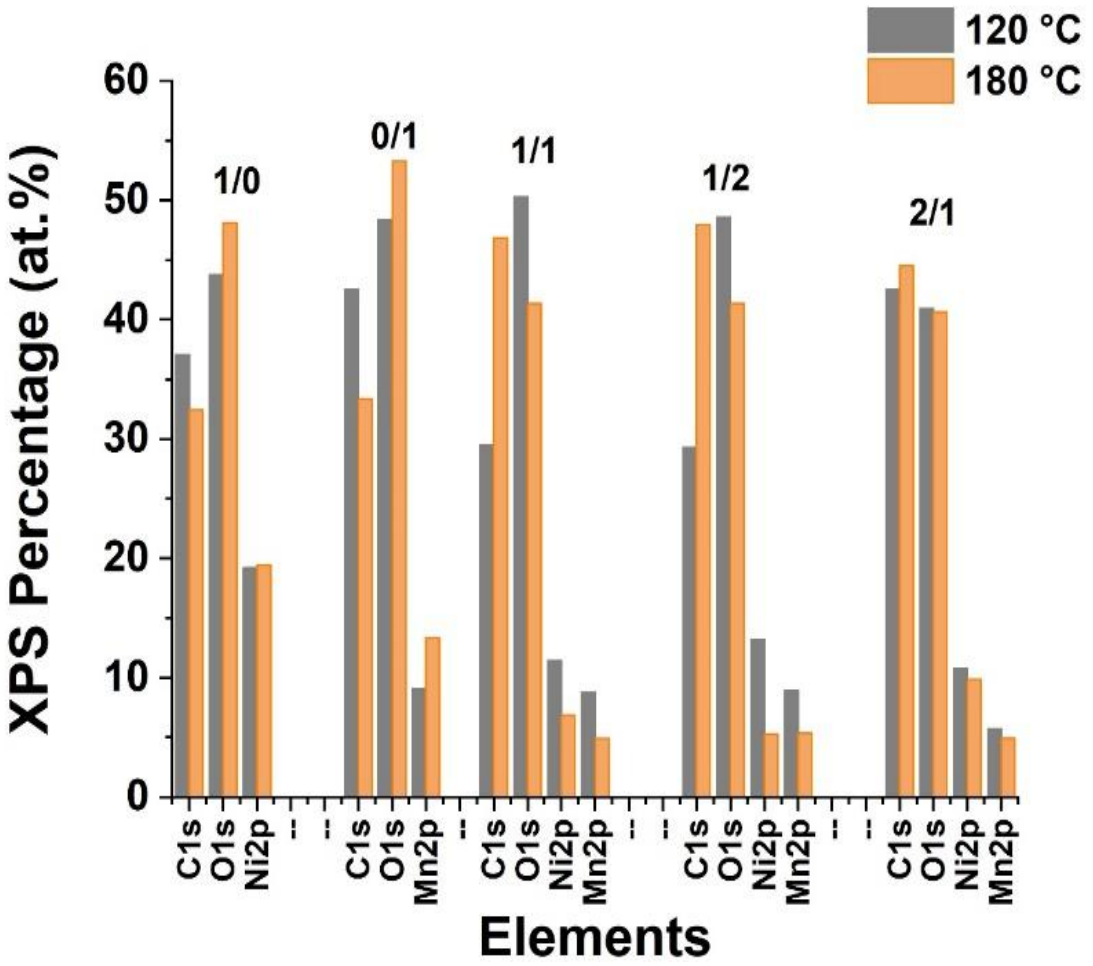

Figure 14: XPS survey scan spectra of the synthesized materials. The spectra were acquired for samples prepared under different conditions, including variations in synthesis temperature and precursor ratio. The data reveals the percentages of elements present.

To gain a deeper understanding of the oxidation states of the elements within the nanohybrids, high-resolution XPS spectra were employed **Figure 15** and **16**. These spectra exhibit asymmetric peaks that require fitting and deconvolution to identify the specific electronic states present in the materials.

For MnCO3-based samples (without nickel, Ni/Mn = 0/1) the C 1s XPS peak analysis shows three different peaks, usually about 284.6 eV, 286.6 eV, and 288.7/289 eV. These peaks provide information on the different chemical environments that the carbon atoms in the material are situated in. The peak C-Mn/C=C (around 284.6 eV) indicates that there are carbon atoms in the structure that are directly linked to manganese atoms or other carbon atoms. The peak C-O/CO_3^{2-} (about 286.6 eV) represents carbon atoms bound to oxygen atoms in carbonate groups

(CO_3^{2-}). The C=O/O-C=O peak, located at around 288.7/289 eV, indicates the existence of carbon linked to oxygen in other functional groups [115, 121, 145].

The C 1s XPS spectra for samples synthesized with just nickel precursors (Ni/Mn = 1/0) reveal variations depending on the growth temperature. At 120°C The presence of a prominent peak at around 290 eV suggests a high concentration (around 80%) of carbon bonded to water molecules, likely from the support material used in the analysis. This indicates the formation of α-Ni(OH)2. However, at 180°C The spectra exhibit strong peaks centered around 289 eV, 291 eV, and 293 eV, along with a peak at 284.6 eV. These peaks collectively suggest the presence of carbon bonded within carbonate groups (C-OO/O-C=O/O=C-O-M) and directly to nickel atoms (C-Ni). This is consistent with the expected formation of Ni(HCO3)2 at this temperature.

When bimetallic precursors with varying Ni/Mn ratios (1/1, 1/2, and 2/1) were used at 120°C, a slight shift in the C 1s peak position was observed to around 287.8 eV. This shift indicates a stronger presence of O-CO bands, suggesting a higher concentration of carbonate anions. Additionally, the relative abundance of these carbonate groups increased with a higher Ni precursor concentration (2/1 ratio, with ~29% at Mn).

For the 2/1 Ni/Mn precursor ratio at 120°C and all products obtained at 180°C, the C 1s spectra revealed two distinct peaks at 286.3 eV and 288.5 eV. These peaks correspond to C-OH/C-O and C=O/O-C=O bonding environments, respectively, likely originating from a combination of Ni(HCO3)2 and MnCO3 contributions [121]. The specific percentages of these bonding types varied depending on the initial precursor content. This finding supports the presence of both hydroxyl and carbonate groups in the final products, consistent with the use of Ni(HCO3)2 and MnCO3 precursors [110].

Furthermore, the intensity of the peak at 284.6 eV, assigned to C-M bonding (where M represents either nickel or manganese), increased with higher metal precursor concentrations. This suggests a greater abundance of carbon directly bonded to the metal atoms in samples prepared with higher metal content.

The O 1s XPS spectra reveal four main peaks, typically positioned around 529 eV, 530.3 eV, 532 eV, and 533/534 eV, with slight variations (±0.5 eV) depending on the sample composition. These peaks provide information about the different bonding environments for oxygen atoms in the material. First M-O (around 529 eV), This peak signifies oxygen bonded directly to the metal atoms (M) within the lattice structure. Second M-CO/C-O/C=O (around 530.3 eV), This peak indicates oxygen bonded to carbon in various functional groups, potentially including

carbonate ($CO3^{2-}$). Third M-OH (around 532 eV), This peak corresponds to oxygen bonded to hydrogen atoms in surface hydroxyl groups (M-O-H) [115, 121, 144].

Chemisorbed Oxygen (around 533/534 eV): This peak can originate from several sources, including oxygen chemisorbed on the surface due to oxide defects, oxygen within crystal water molecules of hydrated hydroxides, or even physically adsorbed water molecules (H-O-H) [144].

For the α-Ni(OH)2 product (Ni/Mn = 1/0), the dominant peak at around 532.3 eV suggests a high concentration (~92%) of oxygen in surface hydroxyl groups (M-O-H). When manganese is introduced (Ni/Mn = 1/1), this peak intensity increases slightly to around 93.2%, potentially due to contributions from hydroxide ions (M-O-H) associated with MnCO3/M-HCO3/M-CO or physically adsorbed water molecules.

In products containing more manganese carbonate or bimetallic carbonate phases, the M-O peak shifts to around 530 eV, indicating a stronger presence of oxygen within carbonate groups (M-CO/C-O/C=O/$CO3^{2-}$). This observation aligns with the findings from the C 1s analysis. Additionally, the O 1s spectra of Ni-Mn nanocomposites reveal a new peak at around 533.5 eV, which is attributed to oxygen-hydrogen (O-H) or carbon-oxygen (C-O) bonding environments [145].

The Ni 2p XPS spectra reveal two main peaks at around 855.5 eV and 873.5 eV, corresponding to the Ni 2p3/2 and Ni 2p1/2 doublets, respectively [144, 146, 147]. Slight variations in these peak positions (±0.5 eV) can occur depending on the element nickel is bonded to (oxygen, carbon, or hydroxyl) in different phases like carbonates or hydrated hydroxides, influenced by the growth temperature. Additionally, two less prominent peaks are observed at around 861 eV and 879 eV, which are attributed to "shake-up satellite" features associated with the main nickel peaks [144]. However, for Ni-Mn based nanohybrids synthesized using bimetallic precursors, new peaks appear at higher nickel concentrations (around 7%). These new peaks, located around 857.3 eV, 865-866 eV, and 875 eV, suggest the presence of Ni^{3+} cations. The concentration of these cations is higher in samples prepared at 120°C with Ni/Mn ratios of 1/2 (around 19% Ni^{3+}/Ni^{2+}) and 2/1 (around 30% Ni^{3+}/Ni^{2+}) [146]. Furthermore, the main Ni 2p doublet and their satellite peaks exhibit slight shifts depending on the Ni/Mn ratio. As the ratio increases from 1/1 to 2/1 and 1/2, the doublet peaks shift slightly higher, and the satellite peaks shift slightly lower in binding energy.

Interestingly, all products prepared at 120°C show a nearly constant spin-orbit energy separation between the Ni 2p1/2 and Ni 2p3/2 peaks (around 18 eV). However, products

obtained at 180°C exhibit a slightly smaller separation (around 17.5 eV). This suggests the presence of dominant Ni^{2+} but also some Ni^{3+} in these samples, as supported by other studies [148]. Analysis of the Mn 2p XPS spectra involved fitting them with multiple peaks. Two main peaks are typically observed at around 641 eV and 652 eV, along with satellite lines centered at approximately 643 eV and 657 eV [115, 121, 149]. These main peaks correspond to the Mn 2p3/2 and Mn 2p1/2 doublets for manganese in the MnCO3 phase, as observed in samples prepared using solely manganese precursors at both growth temperatures. The energy separation between these peaks (around 11.63 eV to 12.08 eV) further indicates the predominant presence of Mn^{2+} in the MnCO3 structure, consistent with previous findings [121, 146]. In some cases, additional peaks are observed around 643 eV and 656 eV, which can be attributed to Mn^{3+} in the 2p3/2 and 2p1/2 states. The presence of these peaks suggests the existence of a small fraction of Mn^{3+} alongside the dominant Mn^{2+} in the MnCO3 phase. The X-ray photoelectron spectroscopy (XPS) analysis of the product obtained at 180°C with a Ni/Mn precursor ratio of 2/1 reveals a fascinating characteristic. The material exhibits a combination of multiple oxidation states for both nickel and manganese [145].

Nickel: The presence of Ni^{3+} cations alongside the expected Ni^{2+} is evident. The analysis suggests that approximately 30% of the nickel atoms exist in the 3+ oxidation state.

Manganese: Similarly, the XPS data indicates the presence of a small fraction of Mn^{4+} cations in addition to the dominant Mn^{3+}. The estimated abundance of Mn^{4+} is around 19%.

This observation suggests a more complex and interesting electronic structure within the Ni (HCO3)/MnCO3 composite material prepared at these specific synthesis conditions (2/1 Ni/Mn precursor ratio and 180°C growth temperature).

Impact of Nickel Incorporation on Manganese Oxidation States:

The Mn 2p XPS spectra show interesting changes upon introducing nickel (Ni^{2+}) into the material, as evident in the figures. A new peak appears around 642/643 eV alongside the main Mn 2p peaks (previously assigned to Mn^{2+} in MnCO3) [125, 137, 150, 151]. This new peak suggests the presence of an additional manganese oxidation state, possibly Mn^{4+} at a higher binding energy (around 644/645 eV).

Our analysis reveals a pattern where the concentration of Mn^{3+} increases with a higher concentration of manganese precursors (at both growth temperatures). However, this increase in Mn^{3+} appears to be counterbalanced by the emergence of Mn^{4+}, especially in samples with a

higher Ni precursor ratio (2/1). This suggests that the incorporation of Ni^{2+} might influence the oxidation state of manganese in the composite material.

Multiple Manganese Oxidation States Revealed by Mn 2p XPS:

Analysis of the Mn 2p XPS spectra indicates the presence of multiple manganese oxidation states within the material. The deconvoluted Mn 2p peaks can be separated into three main components, centered around 641 eV, 642 eV, and 644 eV [115, 146, 151]. These binding energies correspond to Mn^{2+}, Mn^{3+}, and Mn^{4+}, respectively. This observation suggests a relationship where the populations of Mn^{3+} and Mn^{4+} species increase, while the population of Mn^{2+} decreases. This trend is particularly evident in the product obtained at 180°C with a Ni/Mn precursor ratio of 2/1, which exhibits a more complex oxidation state distribution for manganese [145].

XPS Analysis Supports Diverse Oxidation States and Electrochemical Activity:

The X-ray photoelectron spectroscopy (XPS) results align well with the structural findings, confirming the presence of mixed Ni and Mn phases in the synthesized materials. The observed variations in these phases depend on the hydrothermal growth conditions used. Notably, the MnCO3 component exhibits a rich variety of manganese oxidation states (Mn^{2+}, Mn^{3+}, and Mn^{4+}) for both product series. These XPS findings suggest the presence of numerous electroactive sites within the nanohybrids due to the different nickel and manganese oxidation states. This variety of oxidation states is expected to promote strong electronic interactions at the interface between the electrode and the electrolyte during future electrochemical tests (EC tests). These strong interactions can potentially lead to enhanced conductivity within the materials. Furthermore, the presence of these electroactive sites might favor the adsorption of ions and the transfer of electrons at the electrode surface, ultimately improving the overall electrochemical performance of the Ni-Mn based nanohybrids.

The XPS analysis, therefore, highlights the importance of the chosen hydrothermal growth parameters in tailoring the electronic structure (doping and oxidation states) of these Ni-Mn products. This control over the electronic structure is likely to influence their performance in electrochemical applications.

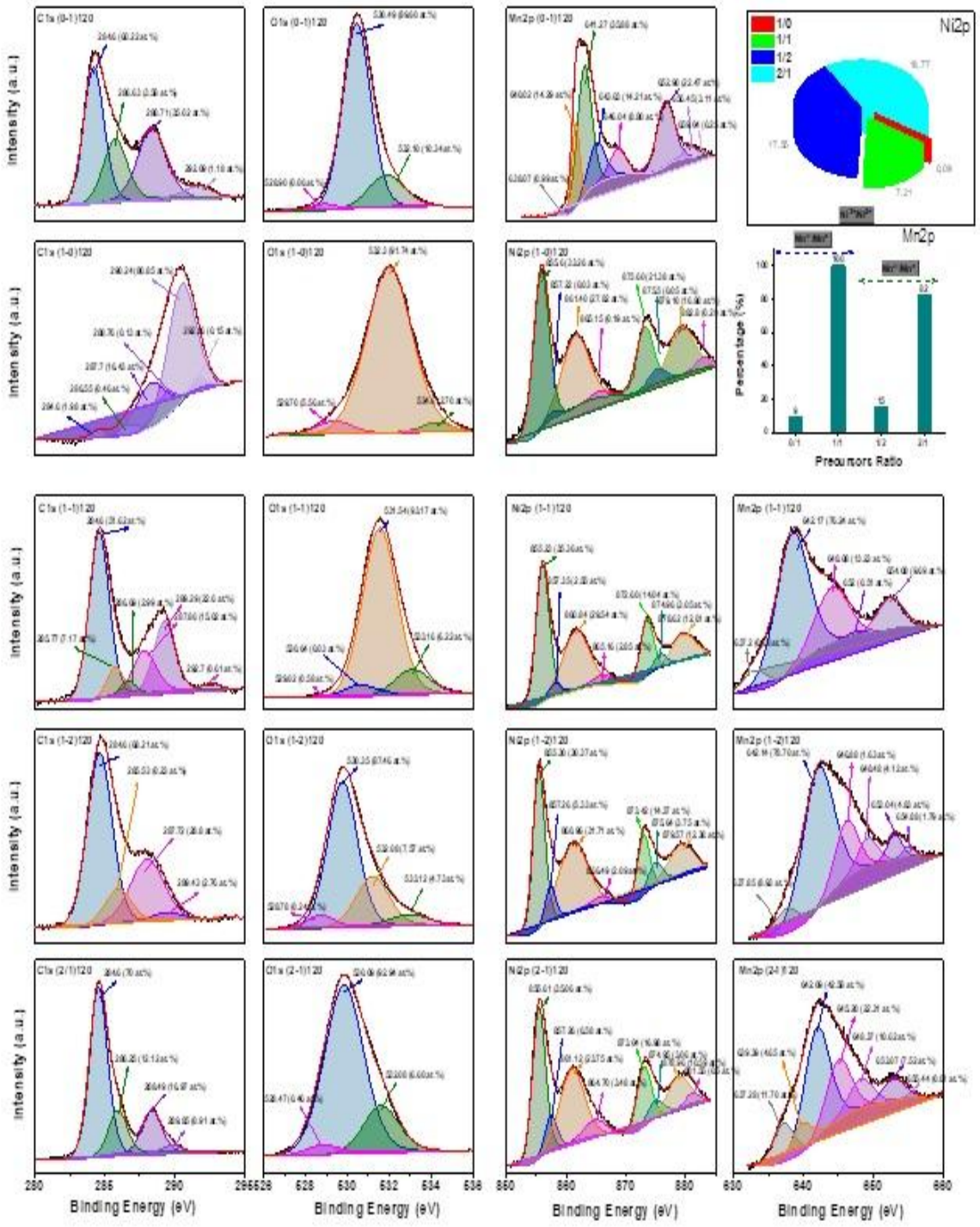

Figure 15: High-Resolution XPS Analysis of Ni-Mn Nanohybrids, prepared at a growth temperature of 120°C, with varying nickel (Ni) to manganese (Mn) precursor ratios. in the Ni2p, Mn2p, C1s, and O1s energy regions.

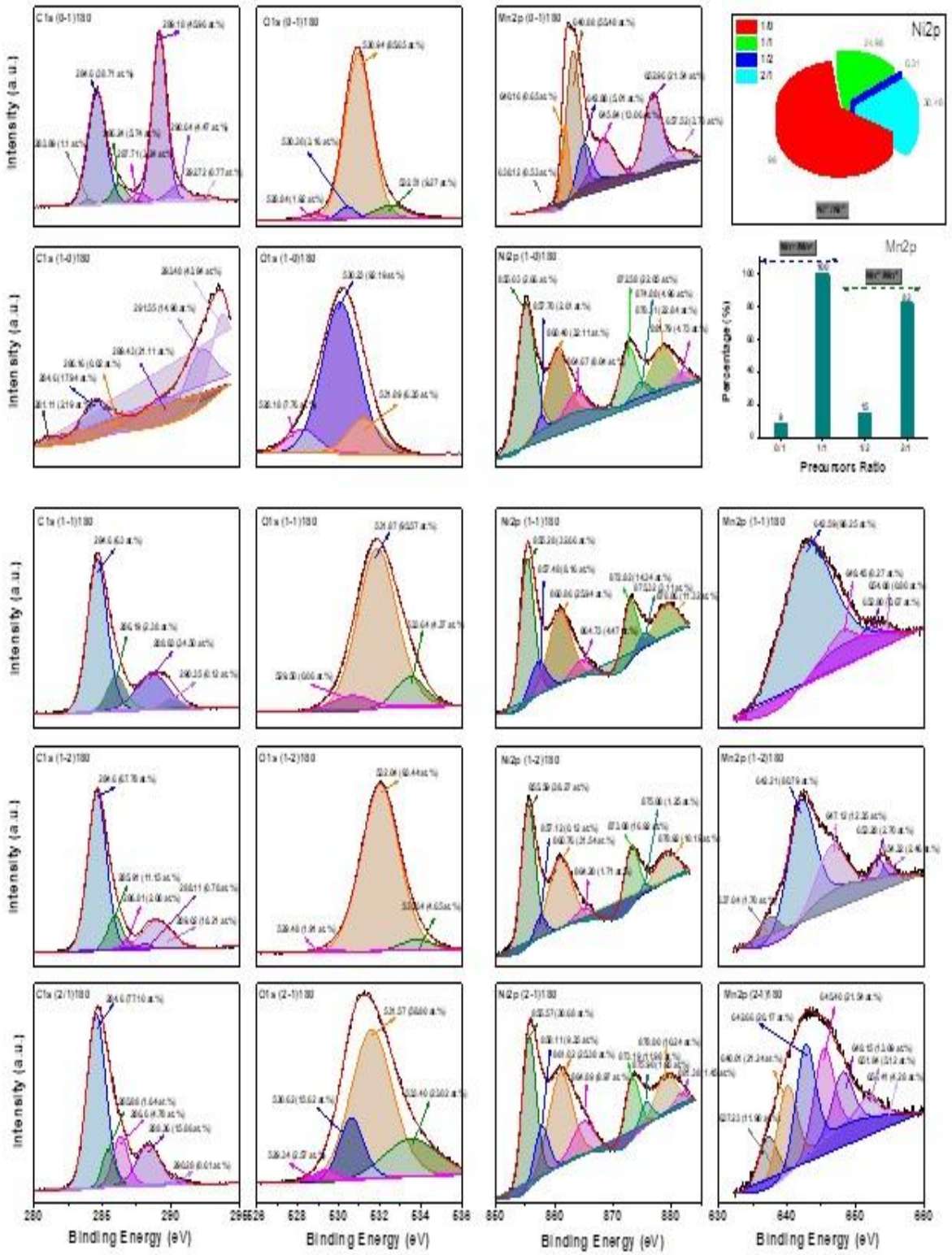

Figure 16: high-resolution XPS spectra of the synthesized Ni-Mn nanohybrids in the Ni2p, Mn2p, C1s, and O1s energy regions, prepared at a growth temperature of 180°C, with varying nickel (Ni) to manganese (Mn) precursor ratios.

2.4. Optical properties:

Figure 17 illustrates the light absorption characteristics of Ni-Mn based nanomaterials, including both single and double nanostructures composed of either hydroxide or carbonate phases. These nanohybrids exhibit a strong tendency to absorb light in the ultraviolet (UV) region, with a peak centered around 200 nm. Following this peak, their absorption rapidly drops to near zero for wavelengths above 250 nm. This behavior indicates minimal light absorption in the visible range, suggesting limited potential for visible light-driven applications like photocatalysis [138].

Extracting the Optical Band Gap using Tauc Plots:

The optical band gap (Eg) of a material signifies the minimum energy required to excite an electron from the valence band to the conduction band. Researchers employed a common technique called Tauc plots to estimate this Eg value for the synthesized Ni-Mn nanohybrids [05, 152, 153].

The Tauc plot method relies on the absorption coefficient (α) of the material, which can be calculated from the measured absorbance (A) obtained using UV-Vis spectroscopy (refer to **Figure 17a** and **17b**). A conversion factor and the sample thickness are also factored into the calculation using the equation $\alpha(\nu) = 2.303A/t$.

Tauc plots involve plotting a specific function of the absorption coefficient (α) versus the photon energy (hν) on a particular scale. The chosen exponent in this function depends on the type of electronic transitions occurring within the material [05, 152, 153]. Figures 10c and 10d depict Tauc plots for the synthesized nanohybrids. In these plots, the square of the product of α and the reduced Planck constant ($\hbar$) is plotted against the photon energy ($\hbar\nu$).

A crucial step involves extrapolating the linear portion of these plots to the point where this function $(\alpha\hbar\nu)^2$ equals zero. This point of intersection on the photon energy axis is considered the estimated Eg value, specifically for direct band gap semiconductors where the exponent n is typically set to 2 [05, 152, 153].

The band gap values obtained for different Ni-Mn nanohybrid compositions, determined using the Tauc plots analysis, are presented in **Figure 17 e.** By analyzing these Eg values, researchers can gain insights into the electronic structure and potential optoelectronic properties of the synthesized materials

Impact of Synthesis Temperature and Oxidation States on Band Gap:

The research suggests a fascinating trend: the optical band gap (Eg) of the Ni-Mn nanohybrids generally decreases with increasing synthesis temperature. This observation applies to materials synthesized using single precursors and to nanocomposites containing nickel hydroxide or carbonate combined with manganese carbonate. Interestingly, the effect is particularly pronounced for samples prepared with a higher nickel precursor ratio (2:1).

XPS analysis (mentioned earlier) revealed a dominance of Ni^{2+} and Mn^{4+} cations in these materials, especially at the higher synthesis temperature (180°C). This dominance of higher oxidation states might be a key factor influencing the band gap. The measured band gap values for direct transitions are around 2.18 eV and 4.34 eV at 120°C and 180°C, respectively. These values represent the minimum energy required for an absorbed photon to excite an electron from the valence band to the conduction band, creating a free electron-hole pair.

The observed decrease in band gap with increasing temperature and higher nickel precursor ratio suggests potentially improved conductivity in these materials. This enhanced conductivity is promising for future studies exploring their electrical properties.

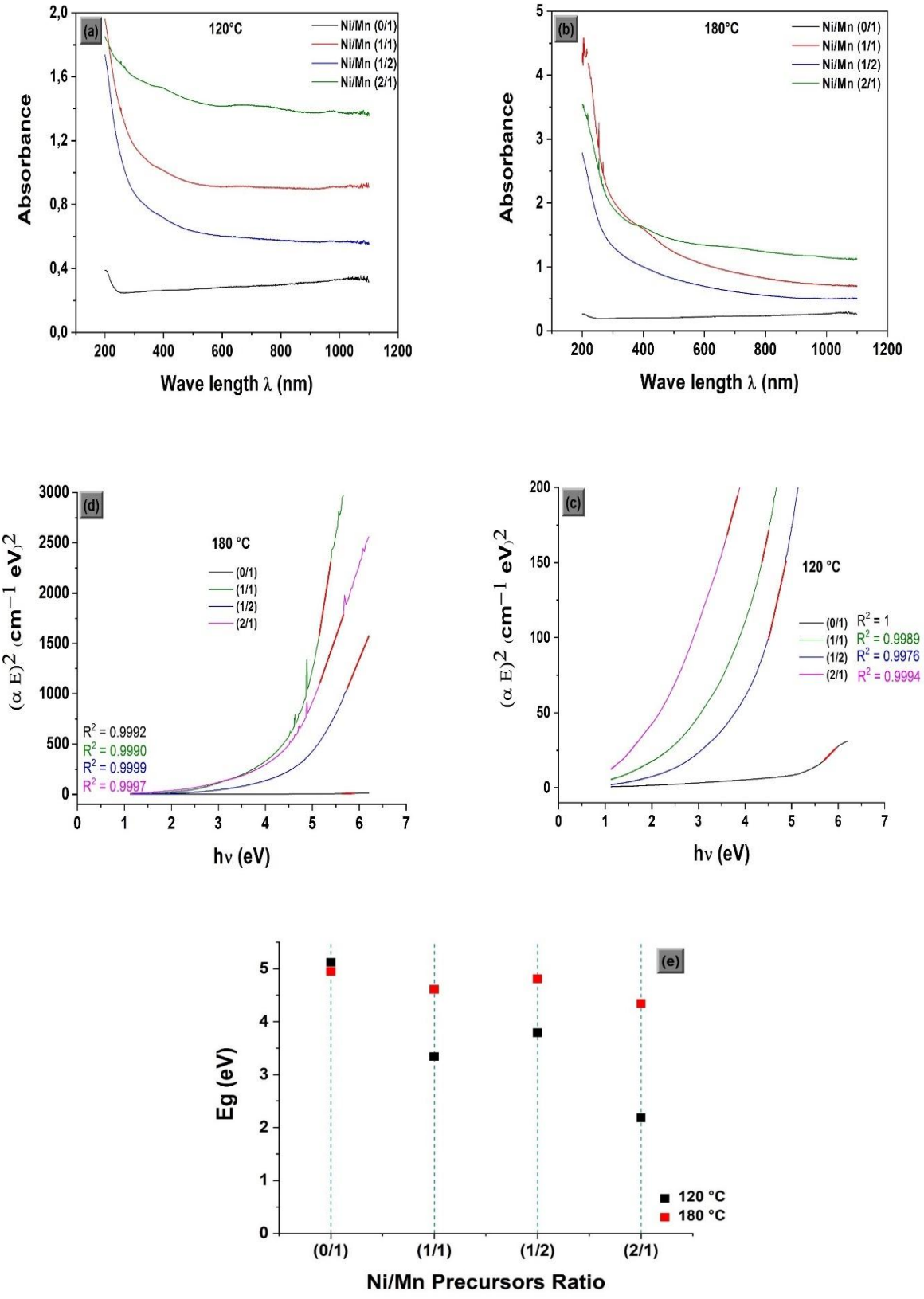

Figure 17: Light Absorption Properties of Ni-Mn Nanohybrids under various optimized synthesis conditions include variations in the precursor ratio between nickel and manganese and the growth temperature.

3. Electrochemical properties:

3.1. Electroactive Surface Area:

Researchers employed cyclic voltammetry (CV) to determine the electroactive surface area of the Ni-Mn nanohybrids. This technique analyzes the oxidation reaction of ferrocyanide ions ($[Fe(CN)_6]^{4-}$ to $[Fe(CN)_6]^{3-}$) occurring at the working electrode, which is composed of the Ni-Mn nanohybrids deposited on nickel foam (NiF). Moreover, Ferrocyanide is a popular choice for such measurements due to its well-established reversible electrochemical behavior on Ni foam surfaces [154–157]. This reversibility allows for accurate calculations of the Area for the Ni-Mn nanohybrids using the Randles-Sevcik equation.

The Randles-Sevcik equation relates the peak current (Ip) observed in the CV plots to the Aea. Other factors influencing the peak current include the number of electrons transferred in the reaction (n), the diffusion coefficient (D) of the ferrocyanide ions in the electrolyte, and the scan rate (ν) used during the CV measurement [157, 158]. In this study, n is assumed to be 1, representing the transfer of a single electron during the ferrocyanide oxidation reaction. The diffusion coefficient (D) of the potassium ferrocyanide ($K_4[Fe(CN)_6]$) was experimentally determined to be 6.56 x 10^-6 cm^2/s using a NiF electrode with a 1 cm^2 electrolyte exposure surface. This value aligns well with theoretical estimates of D for ferrocyanide (around 6 x 10^-6 cm^2/s) [154, 156, 157]. By applying the Randles-Sevcik equation with the measured or established values for n, D, and ν, researchers can calculate the Aea of the Ni-Mn nanohybrids from the corresponding CV data. This approach allows for comparing the Aea of the bare NiF electrode with those of the Ni-Mn nanohybrid modified NiF electrodes. This comparison provides insights into potential diffusion limitations within each synthesized nanomaterial system.

Electroactive Surface Area and Morphology:

The data presented in **Figure 18** reveals a trend where Ni-Mn nanohybrids primarily composed of manganese carbonate exhibit lower electroactive surface areas compared to those with an equal molar ratio of Ni and Mn or with a dominant nickel content. This observation suggests a correlation between the Area and the type of nanohybrid formed.

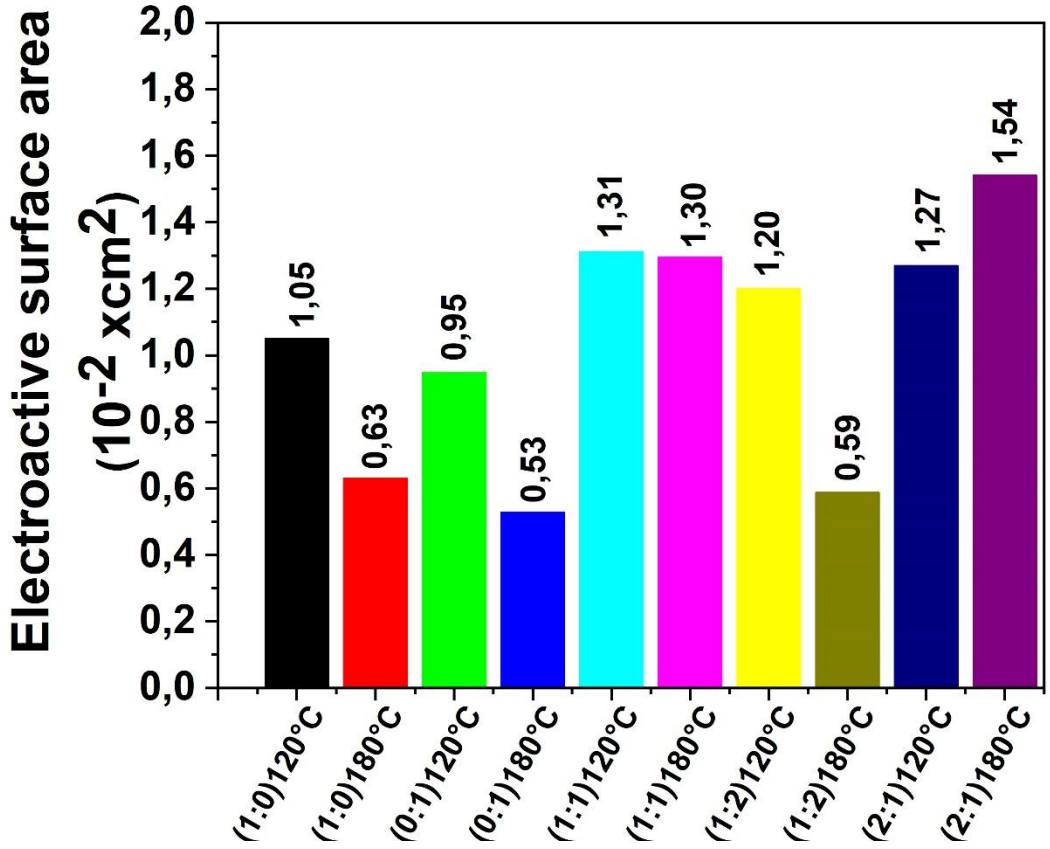

Figure 18: Electroactive Surface Area of Ni-Mn Nanohybrids.

A higher Area value generally translates to a larger surface area accessible for electrochemical reactions. This, in turn, can benefit the overall capacitive performance of the material. The higher Area values observed for Ni-rich or equi-molar Ni-Mn nanohybrids might be attributed to their specific micro/nanoscale morphology. This morphology likely favors a reduction in the diffusion path length for both electrons and electrolyte ions within the material. Consequently, improved accessibility of these species to the active sites might contribute to enhanced capacitive behavior.

Additionally, to achieve superior electrochemical performance, our research focuses on utilizing Ni foams as a scaffold, supported by Ni/Mn-based electroactive nanohybrids. We investigated the improvement of interface contact with the electrolyte to enhance efficient and rapid ion-electron transport, thereby contributing to high-performance supercapacitors. Given the favorable characteristics of Ni/Mn nanohybrids for energy storage applications (such as supercapacitors), as demonstrated in previous studies, their physicochemical properties include

a three-dimensional mesoporous nanohybrid structure, abundant electrochemically active sites from combined metal ion states (Ni2+/Ni3+ and Mn2+/Mn3+/Mn4+), and a low energy gap (Eg) which results in excellent electrical conductivity [159].

3.2. Cyclic voltammetry (CV):

To explore the electrochemical storage mechanism in greater detail, we began with cyclic voltammetry (CV) measurements at different scan rates ranging from 5 to 100 mV/s within a potential range of 0 to 0.6 V. The typical cyclic voltammograms recorded at the slow scan rate of 5 mV/s are shown in **Figure 19 (a, b)**.

As depicted in the figure, at a slow scan rate, one or two pairs of prominent redox (oxidation/reduction) peaks, depending on the nanohybrid composition, are clearly visible. This indicates the presence of a reversible redox or faradaic reaction in the 6 M KOH aqueous electrolyte, facilitated by OH^- and K^+ ions. Consequently, the strong pseudocapacitive behavior of these Ni/Mn-based electroactive nanoproducts [159, 160, 161] is markedly different from the EDLCs mechanism, which typically exhibits CV curves that are close to an ideal rectangular shape [162, 163].

Influence of Composition and Temperature on Redox Behavior:

The cyclic voltammograms presented in **Figure 19** demonstrate that the positions and intensities of the redox peaks are significantly affected by both the Ni/Mn molar ratio and the hydrothermal growth temperature used during synthesis. This relationship suggests a potential connection between the redox behavior and the material's composition and crystal structure. These findings align with previous studies [04, 164, 165, 166], which have similarly highlighted the impact of these factors on the electrochemical properties of transition metal-based nanohybrids.

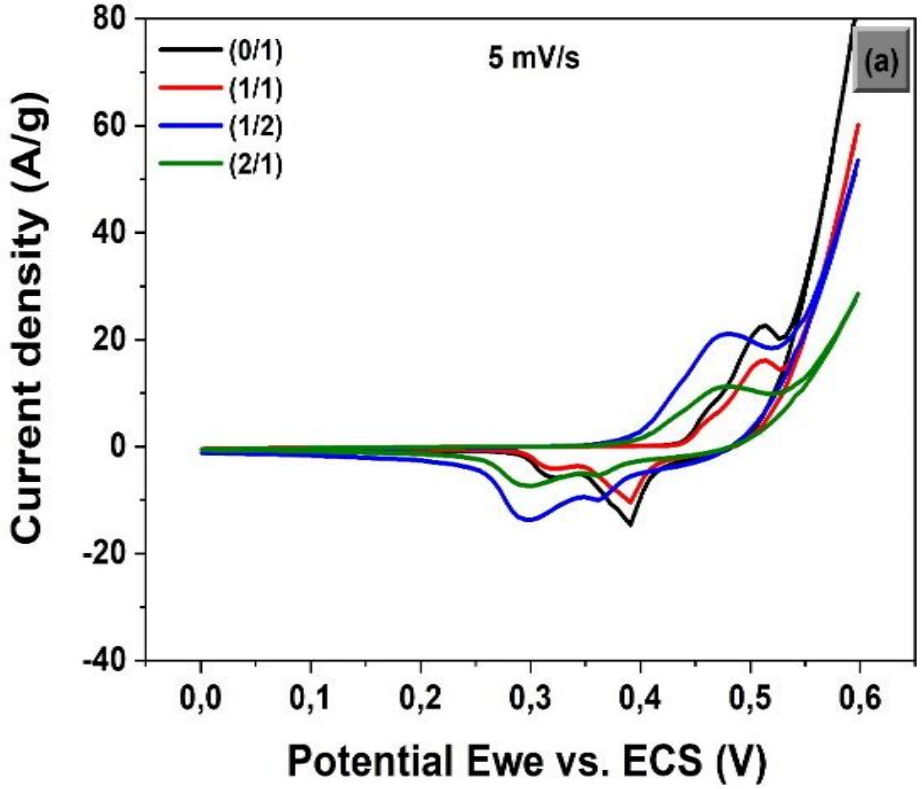
(0/1)
(1/1)
(1/2)
(2/1)
5 mV/s
(a)
Current density (A/g)
Potential Ewe vs. ECS (V)

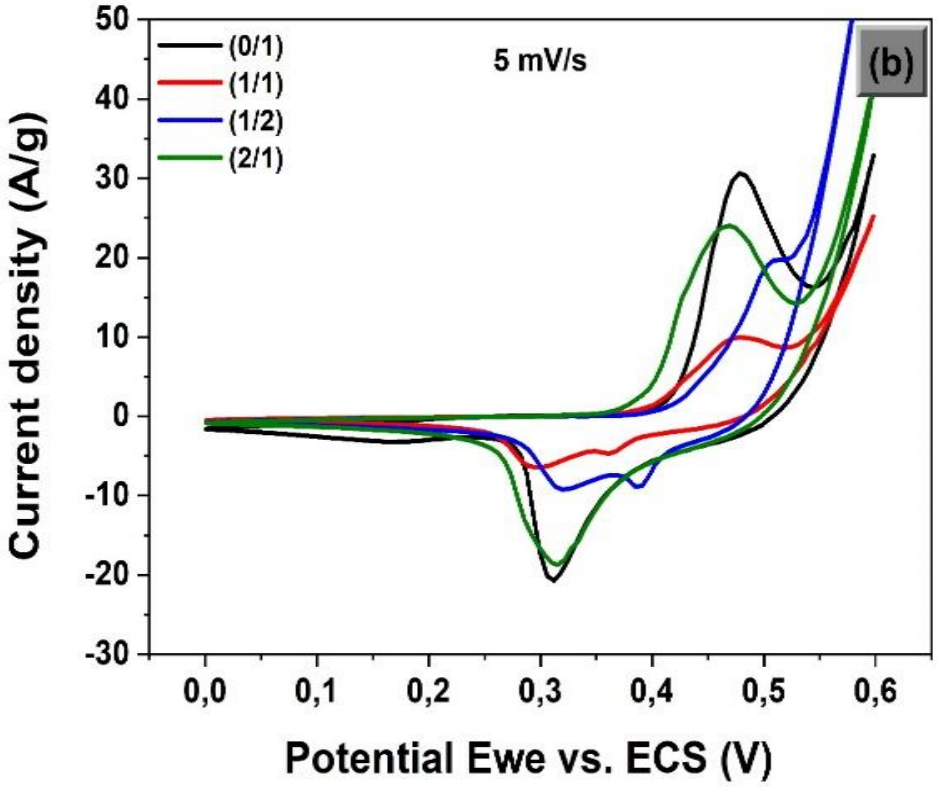
(0/1)
(1/1)
(1/2)
(2/1)
5 mV/s
(b)
Current density (A/g)
Potential Ewe vs. ECS (V)

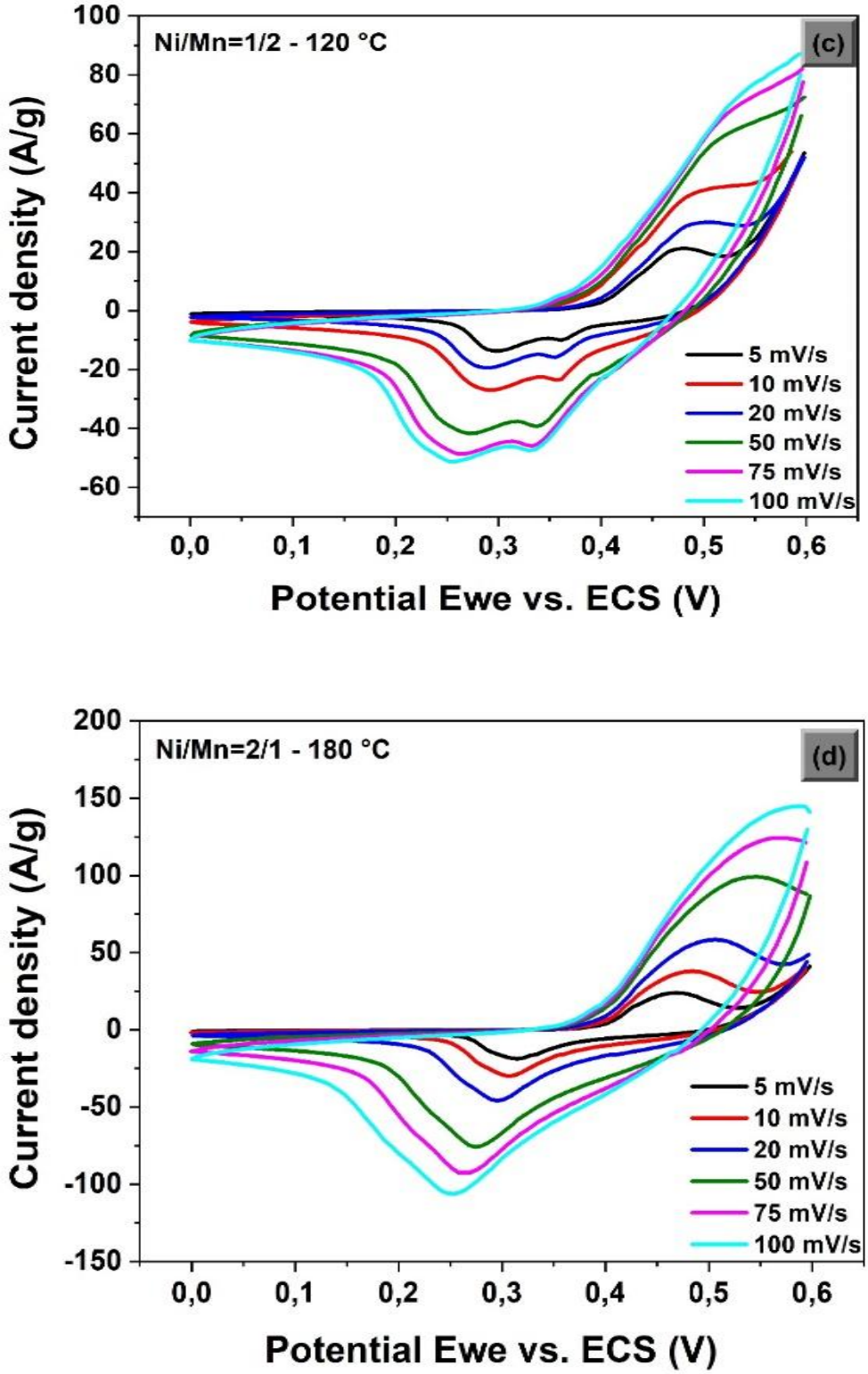

Figure 19. Cyclic voltammograms of the synthesized Ni/Mn-based nanohybrids at two different growth temperatures: 120°C (a) and 180°C (b). CVs at varying scan rates for the two optimal products (c, d).

The distinct redox peaks likely arise from surface Faradaic reactions involving the various metal species present in the Ni-Mn nanohybrids. These reactions might involve quasi-reversible redox processes of electroactive transition metal products. Depending on the specific composition, these products could include α-Ni(OH)2, Ni(HCO3)2, or MnCO3. The following equations provide examples of potential redox reactions that could be occurring [115, 116, 119, 126, 127, 136, 144, 167, 168, 169, 170]:

$$Ni(OH)_2 + OH^- \Leftrightarrow NiOOH + H_2O + e^- \quad \text{(Eq. 114)}$$

$$Ni(HCO_3)_2 + 3OH^- \Leftrightarrow NiOOH + 2HCO_3^- + H_2O + e^- \quad \text{(Eq. 115)}$$

$$3MnCO_3 + 3H_2O \Leftrightarrow 3Mn^{2+} + 3HCO_3 + 3OH \quad \text{(Eq. 116)}$$

By analyzing these equations alongside the observed CV data and the known properties of the constituent materials, researchers can gain further insights into the specific redox processes contributing to the charge storage mechanism in the Ni-Mn nanohybrids.

Impact of Scan Rate on Redox Behavior:

Figure 19 c and **d** illustrates the CV curves obtained at higher scan rates (100 mV s^{-1}). Interestingly, as the scan rate increases from 5 mV s^{-1} to 100 mV s^{-1}, a slight shift in the redox peaks is observed. The oxidation peaks move towards more positive potentials, while the reduction peaks shift slightly negative. This phenomenon can be attributed to two main factors:

Polarization effects: At faster scan rates, the rate of ion diffusion within the electrolyte and electron transfer within the electrode material can become limited. This limitation can lead to a shift in the peak potentials as the system struggles to keep up with the rapid changes in the applied voltage.

Ohmic resistance: As the scan rate increases, the ohmic resistance of the electrolyte and the electrode material can play a more significant role. This increased resistance can also contribute to the observed peak shift.

Despite these peak shifts, the CV curves at higher scan rates (like those in Figure 12c and 12d) still exhibit distinct redox peaks. This persistence of redox features even at faster scan rates suggests good rate performance and high reversibility of the Ni-Mn nanohybrids. These

characteristics are desirable for supercapacitor applications, where fast charge and discharge cycles are crucial.

Influence of Material Composition on Electrochemical Behavior:

The cyclic voltammetry (CV) data presented in **Figure 19** reveals a clear distinction in the electrochemical performance of the synthesized materials. Notably, electrodes composed of single-phase nickel hydroxide or manganese carbonate exhibit significantly lower performance and stability compared to those containing a bi-phase structure based on $Ni(HCO3)_2$ and MnCO3.

This difference can be attributed to the unique properties of the bi-phase Ni(HCO3)2/MnCO3 nanohybrids. XRD analysis confirms that these materials possess a larger interlayer spacing (around 15.5 Å) compared to their single-phase counterparts. This increased spacing provides more space for efficient contact between the electrolyte and the electroactive sites within the material. Consequently, it facilitates faster electron transfer and smoother intercalation/deintercalation of ions during charge and discharge cycles.

These observations from the CV measurements support the notion that the presence of MnCO3 alongside $Ni(HCO3)_2$ plays a crucial role in enhancing the pseudocapacitive performance of the nanohybrids [115, 116, 119]. The combination likely optimizes the material's ability to store and release charge through Faradaic reactions.

In contrast, incorporating Ni^{2+} into the composition appears to influence the material's microstructure and transport properties. This incorporation might lead to improvements in these aspects, potentially reducing mass transport resistance and accelerating electron transport within the nanohybrids. Such improvements can significantly enhance the overall capacitance output of the material.

Enhanced Performance of the (1/2) Ni/Mn Nanohybrid:

Among the various Ni/Mn nanohybrids investigated, the one prepared with a 1:2 Ni/Mn molar ratio and synthesized at 180°C for 6 hours (refer to **Figure 19**) exhibits particularly interesting behavior in its cyclic voltammogram (CV) curve. This specific electrode showcases two distinct pairs of redox peaks with a larger combined area compared to other samples. This larger integrated area suggests a higher degree of electrochemically active species within the material, potentially leading to superior specific capacitance (Cs) as determined by averaging the CV curve area.

Several factors might contribute to this enhanced performance:

Unique Morphology: Field-emission scanning electron microscopy (FESEM) images likely reveal a unique product morphology with interconnected mesoporous structures within quasi-microspheres. This arrangement could provide a larger accessible surface area and facilitate electrolyte penetration, promoting efficient electrochemical reactions.

Multi-Oxidation State Composition: X-ray photoelectron spectroscopy (XPS) analysis [124] might confirm the presence of Ni^{2+} ions alongside Mn^{2+}, Mn^{3+}, and Mn^{4+} ions, indicating the coexistence of multiple oxidation states within the material. This combination of oxidation states could create more active sites for Faradaic reactions, enhancing the overall charge storage capacity.

These observations align well with previous and recent studies on similar materials [132, 171], highlighting the importance of morphology and compositional factors in optimizing the electrochemical performance of Ni-Mn nanohybrids.

Synergistic Effect of Composition and Morphology:

The cyclic voltammetry (CV) data in **Figure 19** provide strong evidence for a beneficial synergistic effect between nickel (Ni) and manganese (Mn) ions in the Ni-Mn nanohybrids. This combined effect surpasses the performance of electrodes containing single metal ions and even those solely composed of their hydroxides or carbonates. This synergy likely arises from a unique interplay between the material's composition and morphology:

Compositional Advantages: Combining Ni and Mn offers several advantages. The presence of both elements might create a more favorable chemical environment for Faradaic reactions compared to single-metal systems. Additionally, incorporating Mn in hydroxide or carbonate forms can further enhance the overall performance.

Morphological Benefits: The specific morphology of the Ni-Mn nanohybrids, as observed through techniques like FESEM (reference source needed), plays a crucial role. Features like interconnected ultrathin nanosheets or nanoneedles can provide efficient channels for mass transport of ions within the electrolyte. This efficient transport allows for better exposure of the active sites to the electrolyte, promoting more and faster electrochemical reactions.

Furthermore, the size and shape of the nanostructures can also influence their performance. For instance, the cubic nanostructures observed in some samples (e.g., 0/1 and 1/1 at 180°C) might experience surface compression of the crystal lattice due to their carbonate-based phases. This

compression, as demonstrated in previous studies on optical properties [132, 171], can lead to a significant increase in the band gap of the material. While the specific impact on CV behavior needs further investigation, it highlights the intricate interplay between various material properties.

These observations emphasize the importance of tailoring both the composition and morphology of Ni-Mn nanohybrids to achieve optimal performance for supercapacitor applications.

Probing Charge Storage Mechanism with Randles-Sevcik Analysis:

Understanding the charge storage mechanism within the Ni-Mn nanohybrids is crucial for optimizing their performance. Previous research of Wang, H, and Pilon, L, suggests that the relationship between peak current intensity (Ip) and scan rate (ν) can provide valuable insights into this mechanism.

Following this approach, the peak currents (both anodic, Ipa, and cathodic, Ipc) obtained from the cyclic voltammetry (CV) curves (refer to **Figure 19**) are plotted against the square root of the scan rate (ν^1/2) in **Figure 20 a,** and **20 b**. This plot is referred to as the Randles-Sevcik plot.

Interestingly, the plots in **Figure 20 a,** and **20 b** exhibit a linear relationship between the peak currents and the square root of the scan rate. This linearity is quantified by the R-squared (R^2) values, which are likely high in this case. This observed linear dependence suggests that the charge storage mechanism might be influenced by one or both of the following factors:

Diffusion-controlled process: The movement of protons within the electrode material or the transport of electrolyte ions could be a limiting factor in the overall charge storage process. This limitation arises from the need for these ions to neutralize the electronic charge accumulating on the electrode surface during the redox reactions.

Mass transfer limitations: The ability of the electrolyte ions to reach and interact with the active sites within the electrode material could be restricted. This limitation could be related to the fundamental electrochemistry of the system, where both electron transfer kinetics and ion diffusion within the electrode play a role [156, 172].

Further investigation is necessary to pinpoint the exact dominant mechanism. However, the Randles-Sevcik analysis provides a valuable starting point for understanding the charge storage behavior in the Ni-Mn nanohybrids.

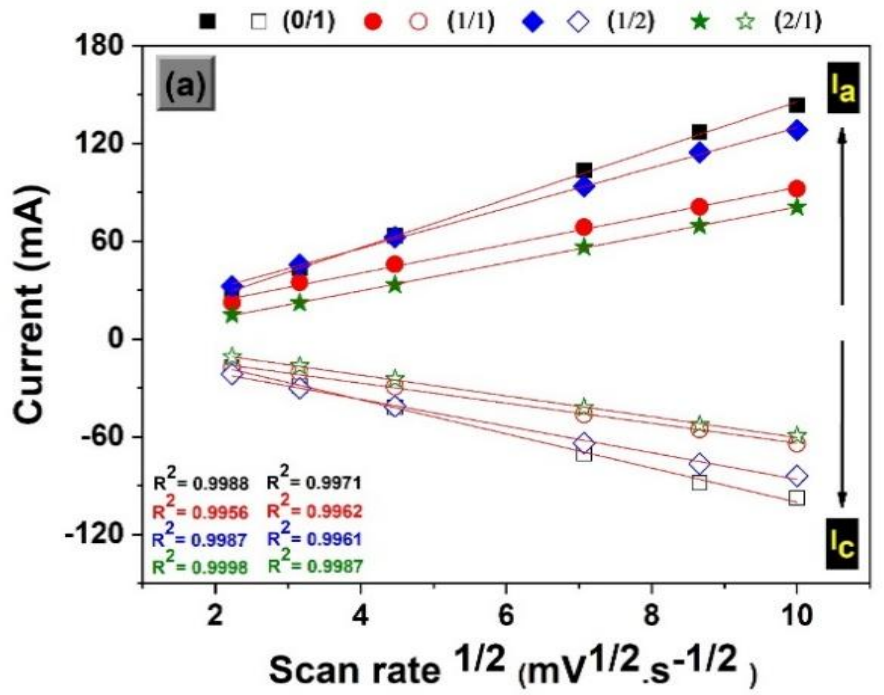
(0/1) (1/1) (1/2) (2/1)
(a)
I_a
I_c
Current (mA)
Scan rate $^{1/2}$ ($mV^{1/2}.s^{-1/2}$)
R^2= 0.9988 R^2= 0.9971
R^2= 0.9956 R^2= 0.9962
R^2= 0.9987 R^2= 0.9961
R^2= 0.9998 R^2= 0.9987

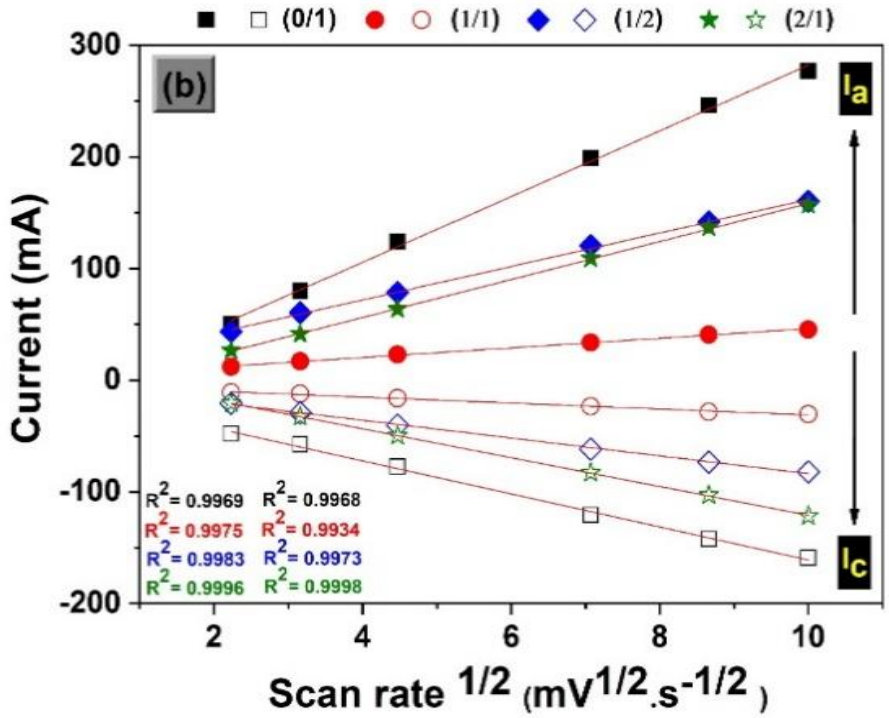
(0/1) (1/1) (1/2) (2/1)
(b)
I_a
I_c
Current (mA)
Scan rate $^{1/2}$ ($mV^{1/2}.s^{-1/2}$)
R^2= 0.9969 R^2= 0.9968
R^2= 0.9975 R^2= 0.9934
R^2= 0.9983 R^2= 0.9973
R^2= 0.9996 R^2= 0.9998

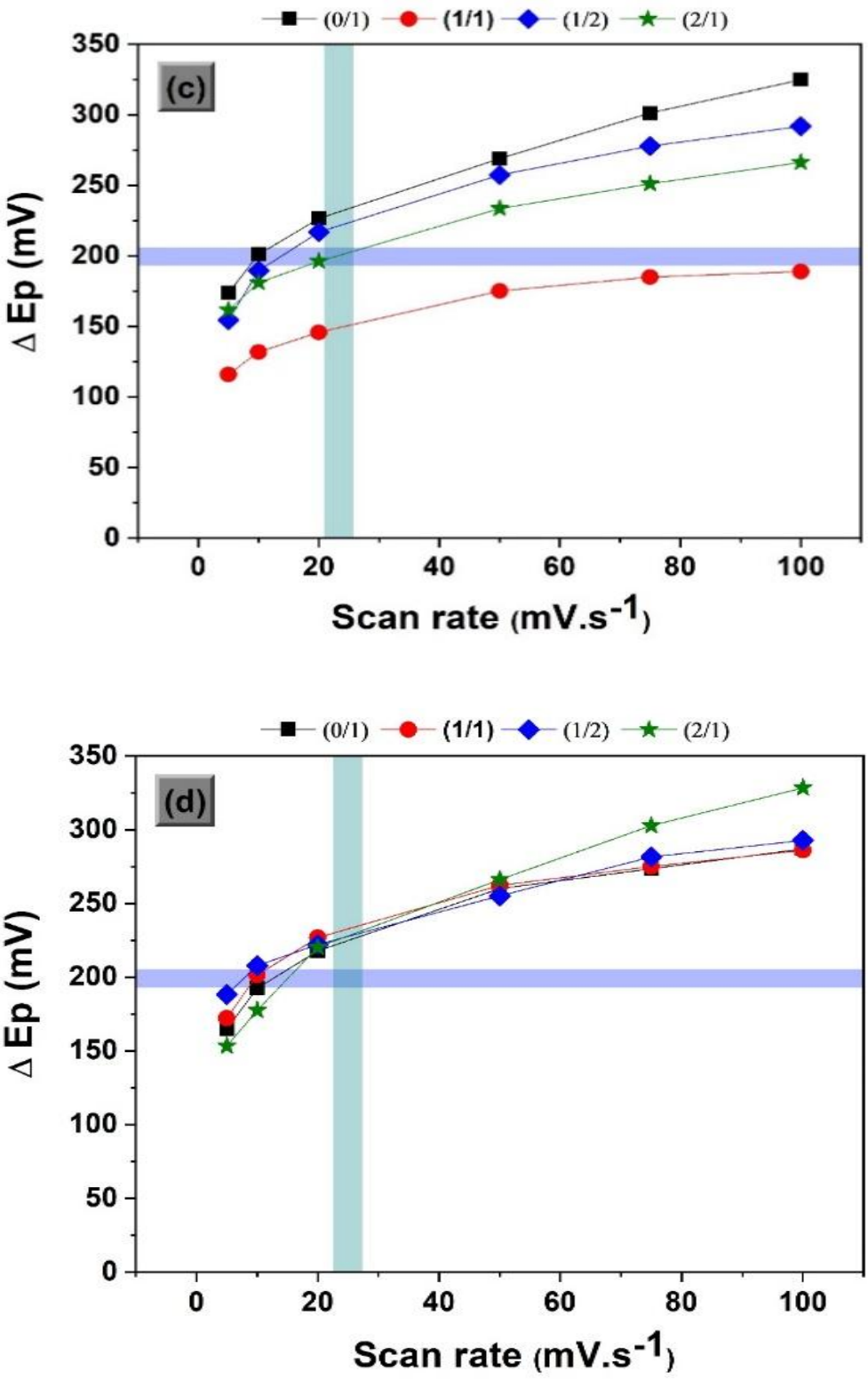

Figure 20: Correlation between peak current (Ip) and square root of scan rate, as well as the relationship between potential difference (ΔEp) and scan rate for synthesized Ni/Mn-based nanohybrids at 120 °C (a, c) and 180 °C (b, d).

Influence of Scan Rate on Peak Separation:

The Randles-Sevcik plots in **Figure 20** (**c** and **d**) reveal another interesting trend. As the scan rate increases, the potential difference (ΔEp) between the anodic and cathodic peaks in the CV curves (refer to **Figure 19**) also increases. This widening gap further supports the notion that both electrolyte ion diffusion and Faradaic redox processes play a crucial role in governing the overall electrochemical performance of the supercapacitor electrodes. These processes are directly involved in the charge storage and release mechanisms during charge and discharge cycles [108, 170].

Generally, a smaller ΔEp value signifies better reversibility of the redox reactions at the electrode surface. As an example, pure manganese carbonate (MnCO3) exhibits good reversibility at high scan rates but suffers from a poor current response (data not shown). This behavior could be attributed to the specific morphology of MnCO3, particularly its micro/nanocubic structures. These structures might not offer sufficient accessibility for electrolyte ions to reach and interact with the active sites within the material, particularly on the inward surfaces. This limitation hinders the overall electrochemical performance [141, 145].

In contrast, the bi-metallic hydroxide/carbonate materials with combined Ni^{2+} and Mn^{3+}/Mn^{4+} ions present a significant advantage. The presence of these multiple oxidation states creates a more electroactive material, leading to improved performance. This enhancement likely stems from the ability of these materials to accommodate changes in cation concentration within the electrode structure. Such changes can influence the charge state of the transition metal cations, ultimately affecting both the magnetic and electrical properties of the material [92, 173]. This interplay between composition, morphology, and charge state underscores the importance of optimizing these factors for superior supercapacitor performance.

3.3. Discharge Behavior Reflects Performance:

Figure 21 a and **b** presents the discharge curves obtained from charge-discharge tests of the synthesized Ni-Mn nanohybrids. These curves, measured at a current density of 1 A/g, exhibit a characteristic shape indicative of pseudocapacitive behavior. This behavior is evident from the presence of quasi-plateaus within a potential range of approximately 0.3 V to 0.5 V. This observation aligns well with the findings from the cyclic voltammetry (CV) curves (refer to **Figure 19**), further supporting the pseudocapacitive nature of the charge storage mechanism.

The discharge curves also highlight the significant influence of the preparation method on the final product's properties and performance. Variations in the Ni/Mn precursor ratio and growth temperature clearly affect the structural, morphological, and spectroscopic characteristics of the synthesized materials. This connection between synthesis parameters and material properties ultimately translates to differences in electrochemical performance, as evidenced by the varying discharge durations observed in **Figure 21**.

Interestingly, specific Ni/Mn molar ratios, namely 1:2 at 120°C and 2:1 at 180°C, exhibit the longest discharge durations among all samples – approximately 524 seconds and 1153 seconds, respectively (**Figure 21 c** and **d**). This extended discharge time suggests a higher capacitance for these compositions. Further analysis is needed to quantify the specific capacitance values.

These observations emphasize the importance of optimizing the synthesis process to control the material's properties and achieve superior performance in supercapacitor applications.

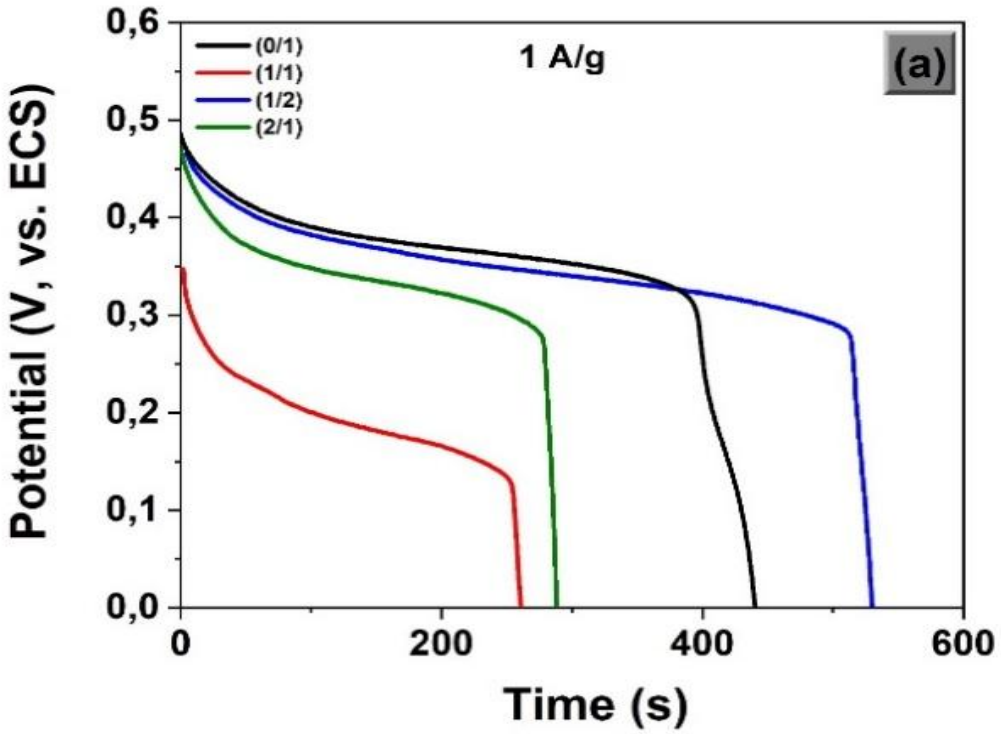

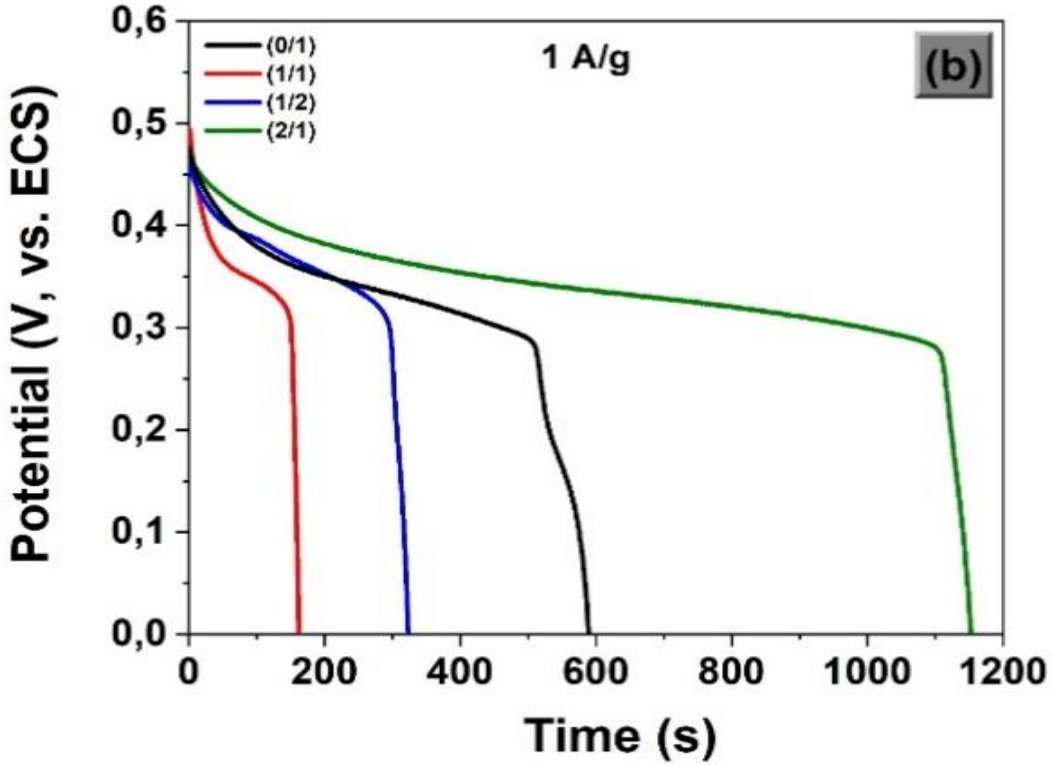
(b)
1 A/g
(0/1)
(1/1)
(1/2)
(2/1)
Potential (V, vs. ECS)
Time (s)
0,0
0,1
0,2
0,3
0,4
0,5
0,6
0
200
400
600
800
1000
1200

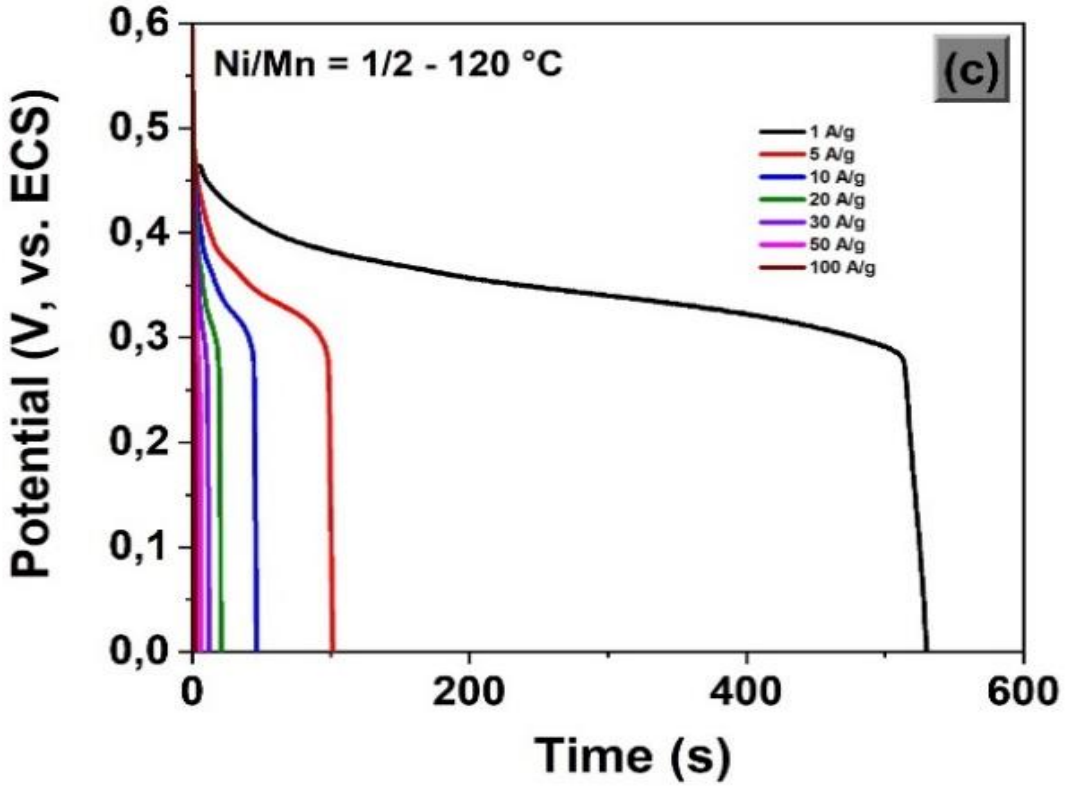
(c)
Ni/Mn = 1/2 - 120 °C
1 A/g
5 A/g
10 A/g
20 A/g
30 A/g
50 A/g
100 A/g
Potential (V, vs. ECS)
Time (s)
0,0
0,1
0,2
0,3
0,4
0,5
0,6
0
200
400
600

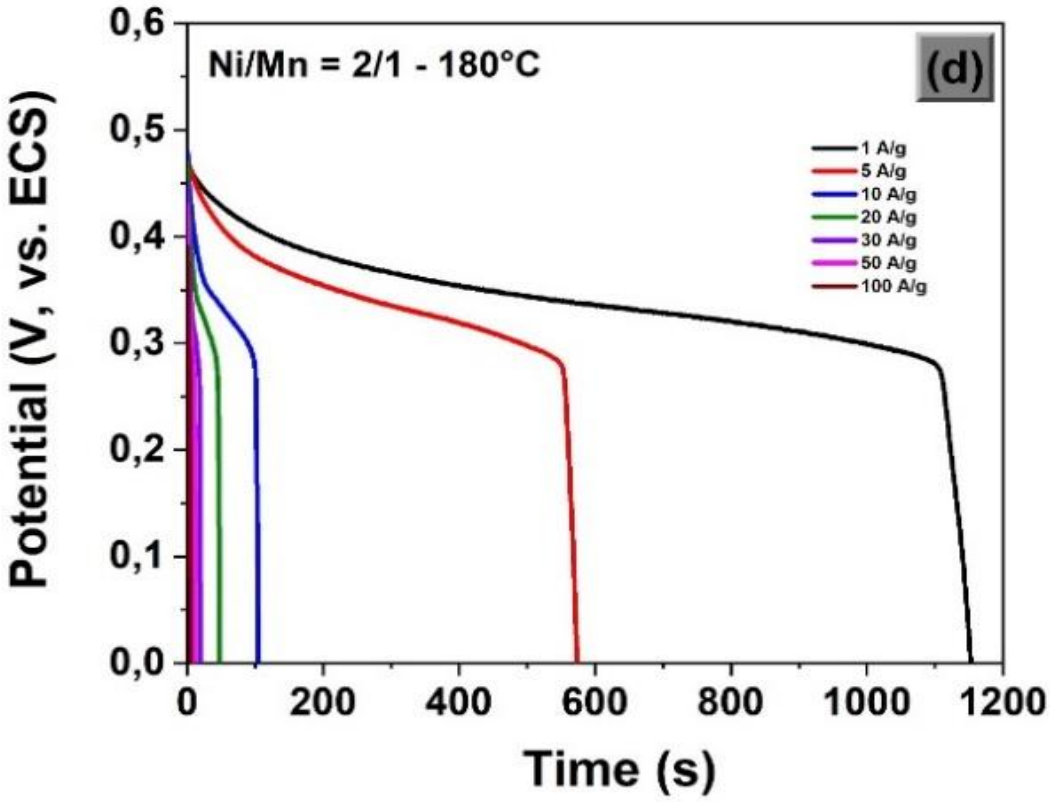

Figure 21: Discharge profiles of Ni/Mn-based nanohybrids synthesized at 120 °C (a) and 180 °C (b). Discharge capacity as a function of current density for the two optimal samples (c, d).

Capacitance Evaluation and Scan Rate Dependence:

The capacitance performance of the Ni-Mn nanohybrids was evaluated using both galvanostatic charge-discharge (GCD) and cyclic voltammetry (CV) techniques. **Figure 22** presents the calculated capacitance values derived from the CV data, measured at a slow scan rate of 5 mV/s. These values range from 1100 F/g to 2800 F/g, highlighting the dependence of capacitance on the specific physico-chemical properties of the electroactive materials, as previously discussed.

An important observation from **Figure 22** is the decreasing trend in capacitance with increasing scan rates, a phenomenon consistently reported in the literature [108, 116, 119]. This decrease can be explained by the limitations imposed by scan rate on the utilization of the electrode material.

At slower scan rates, the extended time window allows for a more complete electrochemical reaction to occur throughout the entire electrode volume, including both the inward and exterior surfaces of the electroactive material. This comprehensive reaction maximizes the utilization of available charge storage sites, leading to higher capacitance values.

In contrast, faster scan rates offer less time for diffusion and interaction of electrolyte ions within the electrode. Consequently, the charge storage process becomes primarily confined to the readily accessible surface sites of the electrode. This limited utilization translates to a decrease in the observed capacitance at high scan rates.

This relationship between scan rate and capacitance aligns well with the observations made from the CV curves in **Figure 19** (**a**, **b**). The high linearity of the redox peaks at slower scan rates suggests efficient utilization of the electrode material, whereas faster scan rates might restrict this utilization.

These findings underscore the importance of considering scan rate alongside other factors when evaluating the performance of supercapacitor electrode materials.

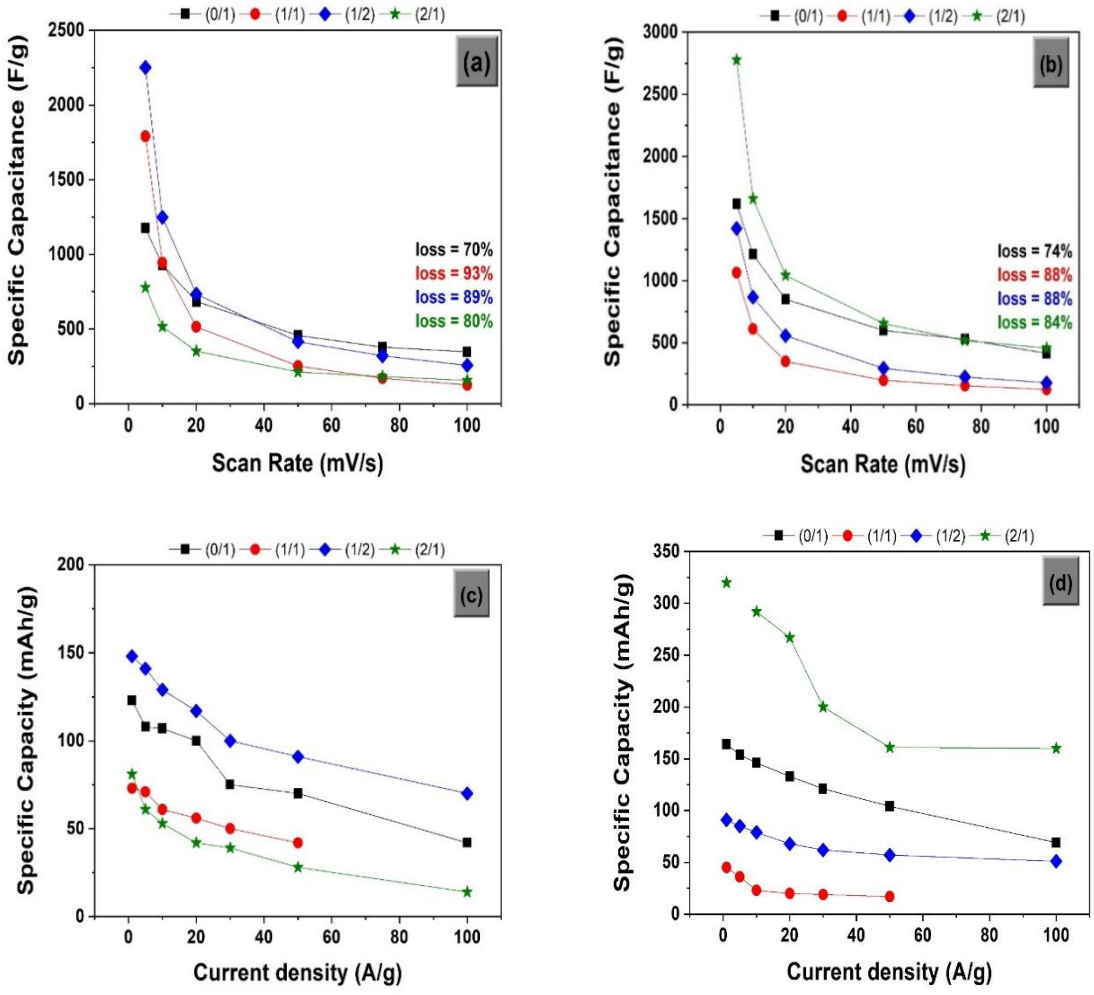

Figure 22: Variation of specific capacitance (Cs: a, b) and total capacitance (Qs: c, d) for the synthesized Ni/Mn nanohybrids with scan rate and current density, respectively.

Capacity Retention and Current Density:

The specific capacity values calculated from the discharge curves **Figure 21** exhibit a decreasing trend with increasing current density. This observation aligns with the notion that the diffusion of electrolyte ions within the electrode material can become a limiting factor at higher current densities. This limitation restricts the ability of ions to effectively reach and interact with all available charge storage sites, ultimately reducing the achievable capacity.

The specific capacities of the synthesized Ni-Mn nanohybrids range from approximately 50 mAh/g to 320 mAh/g at a current density of 1 A/g. Notably, the Ni/Mn (2/1) electrode prepared at 180°C stands out with the highest specific capacitance of around 2800 F/g at a slow scan rate of 5 mV/s (refer to **Figure 22**). This exceptional performance is further corroborated by its extended discharge time in the GCD measurements (**Figure 21**), signifying a superior capacity of 320 mAh/g.

This specific capacitance value surpasses those typically reported for pure manganese carbonate or nickel carbonate electrodes. The combination of Ni and Mn in this composition appears to be a key factor contributing to this remarkable improvement.

Potential Mechanisms for Enhanced Performance:

The synergistic effect of incorporating nickel alongside manganese likely offers several advantages:

Improved Electronic Conductivity: The presence of nickel can enhance the overall electronic conductivity of the electrode material. This improved conductivity facilitates faster electron transfer within the electrode, promoting efficient utilization of the active material during charge and discharge cycles.

Enhanced Electrical Contact: The specific morphology of the electrode, where MnCO3 nanocubes are supported on nickel foam, might contribute to better electrical contact between the active material and the current collector. This improved contact minimizes electrode polarization, further optimizing performance.

These combined effects likely play a crucial role in the outstanding performance observed for the Ni/Mn (2/1, 180°C) electrode, making it a promising candidate for supercapacitor applications [174].

Benefits of Hybrid Nanosheet Morphology:

The observed morphology of the Ni/Mn (2/1, 180°C) electrode, characterized by hybrid nanosheets, offers several potential advantages for supercapacitor applications:

Improved Electrolyte Accessibility: The nanosheet structure can act as an efficient scaffold, promoting the uniform distribution of $MnCO_3$ nanoparticles at a nanoscale. This fine distribution ensures that all $MnCO_3$ components are readily accessible to the electrolyte. This accessibility is crucial for efficient electrochemical reactions throughout the entire electrode volume.

Shorter Diffusion Paths: The nanosheet morphology also contributes to shorter diffusion lengths for both electrolyte ions and electrons within the electrode material. This reduction in distance minimizes the time required for ions and electrons to reach their respective reaction sites, facilitating faster charge and discharge processes.

These combined effects, as supported by previous research [121, 171], likely contribute to the enhanced diffusion and migration of electrolyte ions during rapid charge and discharge cycles. This efficient utilization of the electrode material ultimately translates to the impressive electrochemical performance observed for the Ni/Mn (2/1, 180°C) electrode.

The promising performance of the Ni/Mn (2/1, 180°C) electrode suggests its potential as a valuable electrode material for various energy storage applications. Beyond supercapacitors, this material could also be explored for its suitability in other electrochemical technologies like biosensing, where its unique properties might prove beneficial.

3.4. Electrochemical Impedance Spectroscopy (EIS) Analysis:

To gain further insight into the factors influencing the electrochemical performance of the synthesized Ni-Mn nanohybrids, electrochemical impedance spectroscopy (EIS) measurements were conducted at open circuit potential within a frequency range of 100 kHz to 1 Hz. The results presented in **Table 2** provide valuable information about the charge transfer kinetics and ionic transport within the electrode materials.

Table 2: The equivalent series resistance (RESR) of the as-prepared Ni/Mn nanohybrids was determined.

NanoProducts	R_{ESR}	
	120 °C	**180 °C**
Ni/Mn (0/1)	0.40	0.81
Ni/Mn (1/1)	0.64	0.69
Ni/Mn (1/2)	**0.31**	2.80
Ni/Mn (2/1)	0.65	**0.38**

Notably, the EIS data reveals that the Ni/Mn electrodes prepared with a molar ratio of 1:2 at 120°C and 2:1 at 180°C exhibit the lowest resistance (represented by RESR in the table). This low resistance signifies favorable charge transfer kinetics at the electrode-electrolyte interface.

Enhanced Performance with Higher Ni/Mn Ratio:

The observed trend suggests that increasing the molar ratio of Ni to Mn (up to a ratio of 2:1) leads to improved charge transfer kinetics. This enhancement can be attributed to two potential factors:

Mass Transport: The specific morphology and pore size distribution within the Ni-Mn nanohybrids likely play a crucial role in mass transport. The presence of an optimal pore structure might facilitate the efficient diffusion of electrolyte ions throughout the electrode material.

Electroactive Area: The nanostructured morphology of the electrodes also contributes to a larger electroactive area. This increased area provides more accessible sites for the electrochemical reactions to occur, promoting efficient utilization of the electrode material.

These combined effects, supported by the observed high specific capacity (mentioned earlier), suggest that the Ni/Mn (2/1) electrode synthesized at 180°C exhibits the most favorable overall electrochemical performance [175].

3.5. Long-Term Stability Evaluation:

To assess the practical viability of the synthesized Ni-Mn nanohybrids for supercapacitor applications, their long-term cycling performance was evaluated. Figure 23 presents the results of cyclic measurements, specifically showing the capacity retention of the best-performing

Ni/Mn electrode after subjecting it to galvanostatic charge-discharge (GCD) cycling for 2000 cycles at a high current density of 30 A/g.

These measurements reveal promising characteristics for the Ni-Mn nanohybrids. The electrodes exhibit excellent electrochemical stability throughout the extended cycling test, as evidenced by their high capacitance retention. Notably, the specific capacitance remains at approximately 99.63% of its initial value after 2000 cycles.

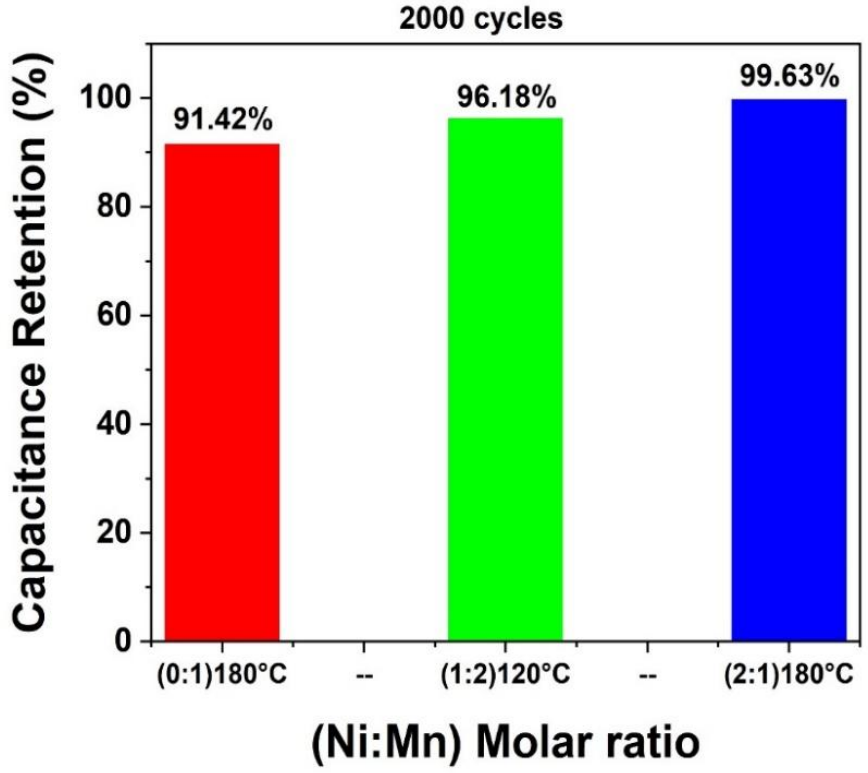

Figure 23: Capacitance stability of the optimal Ni/Mn nanohybrids over repeated charge-discharge cycles at a current density of 30 A/g.

Factors Contributing to Stability:

This impressive stability can be attributed to several factors:

Low Charge Transfer Resistance (Rct): The low Rct value suggests minimal resistance to electron transfer at the electrode-electrolyte interface. This efficient electron transfer is crucial for maintaining stable performance during charge and discharge cycles.

High Active Surface Area: The presence of a high active surface area within the Ni-Mn mesoporous nanohybrid structure provides ample space for the electrochemical reactions to

occur. This large surface area minimizes the stress experienced by the electrode material during cycling, contributing to improved stability.

Robust Nanohybrid Structure: The inherent robustness of the Ni-Mn nanohybrid structure likely plays a role in its long-term stability. This robustness allows the material to withstand the repeated structural changes that occur during charge and discharge cycles, minimizing performance degradation [176].

Promising Candidate for Supercapacitors:

The combination of excellent cycling stability and high capacitance retention observed for the Ni-Mn nanohybrids makes them highly promising candidates for use as electrode materials in supercapacitors. Their ability to maintain stable performance over extended cycling periods is crucial for real-world applications.

Table 3 summarizes the performance of various synthetic methods for mono and binary mixed transition metal hydroxides and carbonates. It highlights their specific capacitances, allowing for a comparison between different approaches. Notably, the work presented here achieves a highly competitive specific capacitance (2780 F g^{-1} / 320 mAh g^{-1})

.

Table. 3: A comparison of the electrochemical properties of transition metal hydroxide-based electrodes, tested in a three-electrode cell setup using an aqueous alkaline electrolyte, as presented in this study and in previously published data.

Synthesis method	Products	Cs ($F.g^{-1}$)	cycling Retention (%)	References.
Hydrothermal	Co, Mn-LDH@NF	2422 (1 $A.g^{-1}$)	86.5% (3000 cycles)	2018 [161]
Template-free solvothermal	$Ni(HCO_3)_2$	1797 (5 $A.g^{-1}$)	80% (5000 cycles)	2016 [86]
Hydrothermal chemical coprecipitation	NiMn-LDH/Graphene foam	2380 (1 $A.g^{-1}$)	94.9% (1000 cycles)	2020 [166]
Hydrothermal	NiMn-LDH@CuO/CF	2430 (0.8 $A.g^{-1}$)	89.22% (8000 cycles)	2020 [177]
Facile two-step hydrothermal	NiO/NiMn-LDH	937 (0.5 $A.g^{-1}$)	91% (1000 cycles)	2017 [173]
Hydrothermal	$Ni(OH)_2$	1111.3 (1 $A.g^{-1}$)	90.4% (1000 cycles)	2020 [178]
Hydrothermal	**$Ni(HCO_3)_2/MnCO_3$**	**2780 at 5 $mV.s^{-1}$ (320 mAh/g)**	**99.63% (2000 cycles)**	**This work**

Conclusion

This chapter presents a comprehensive analysis of Ni/Mn-based mono and bi hydroxides and or carbonates synthesized as mesoporous nanohybrids through a straightforward, expeditious, and economical template-free approach. The investigation delves into the correlation between experimental parameters and the resulting physicochemical attributes of these nanohybrids. These properties, in turn, significantly influence the electrochemical behavior and overall performance of the materials for a range of applications.

The study successfully produced novel micro/nanosystems exhibit exceptional structural, morphological, and textural characteristics leading to the impressive electrochemical performance of our Ni/Mn-based nanohybrids, engineered with a mesoporous architecture.

Among the materials synthesized in this study, the optimal product comprises a bicarbonate nanostructure of Ni(HCO3)2/Mn(CO3). Prepared at 180 °C for 6 hours with a Ni/Mn precursor ratio of 2/1, this material demonstrated superior electrochemical performance. Notably, it achieved a remarkable specific capacitance of approximately 2780 F g^{-1} at a scan rate of 5 mV s^{-1}, corresponding to 320 mAh g^{-1} at a current density of 1 A g^{-1}, while maintaining excellent rate capability. The optimized synthesis conditions have significantly impacted the structural and compositional attributes of the nanohybrids, directly influencing their electrochemical properties. Therefore, these electro-active nanocomposites hold great promise for the development of advanced supercapacitors.

General conclusion

Research in supercapacitors (SCs) primarily centers on augmenting energy density without compromising power or durability. Toward this goal, numerous nanostructured electrode materials and combinations of capacitive and faradic electrodes have been investigated.

Despite significant advancements in energy storage technology, a deeper understanding of charge storage mechanisms and related terminology is essential for achieving substantial improvements.

Pseudocapacitive materials store energy via rapid, battery-like redox reactions, yet exhibit charging speeds comparable to electrochemical double-layer capacitors. This unique combination presents an opportunity to develop devices with both high energy and power densities. To fulfill the growing demand for fast-charging energy storage solutions, materials capable of sustaining high power output over extended periods are essential.

This doctoral research focused on developing electroactive nanomaterials for supercapacitor applications. To this end, nickel-manganese mono and bi-nanostructures were synthesized via a facile, rapid, and economical hydrothermal approach. Experimental parameters, including precursor ratio and temperature, were systematically varied to determine the optimal conditions for achieving desired material properties. The resulting nanomaterials were comprehensively characterized to elucidate their structural, textural, and morphological features. Electrochemical performance was subsequently evaluated to assess their suitability as supercapacitor electrodes.

The Ni/Mn ratio and growth temperature influenced the synthesized nanohybrids. X-ray diffraction analysis revealed three distinct crystalline phases within both mono- and bi-nanostructures, corresponding to transition metal hydrotalcite or brucite structures.

Product displaying exceptional electrochemical performance. This bi-carbonate nanostructured $Ni(HCO_3)_2/Mn(CO_3)$ composite, prepared at 180°C for six hours with a Ni/Mn precursor ratio of 2:1, demonstrated a remarkable specific capacitance of approximately 2780 F g^{-1} at a scan rate of 5 mV s^{-1} (equivalent to 320 mAh g^{-1} at 1 A g^{-1}), coupled with excellent rate capability. The unique sea anemone-like hollow structure, adorned with perpendicularly aligned nanoneedles, forms a hierarchical 3D architecture with open spacing, rendering it a highly promising candidate for supercapacitor electrodes and even for other related applications.

Outlook

Building upon the promising results of this study, which demonstrated the critical influence of nanostructure and composition on a material's storage performance, future research will focus on advancing the entire class of transition metal-based nanohybrids. This understanding is crucial for optimizing electrode materials to achieve higher electrical conductivity and improved reversibility, which are essential for extending the overall material life. A key strategy for achieving these goals involves incorporating conductive additives such as graphene and conducting polymers. By creating composite electrodes, this approach aims to leverage the synergistic effect of these materials to further enhance electrical conductivity and surface area while also tailoring the pore structure to control pore size and volume. This control is vital for facilitating efficient ion transport and desolvation, paving the way for developing next-generation supercapacitors with even higher energy and power densities, addressing a crucial need in advanced energy storage applications.

References:

[01] L. Fagiolari, M. Sampo, ` A. Lamberti, J. Amici, C. Francia, S. Bodoardo, F. Bella, Energy Storage Mater. 51 (2022) 400–434. https://doi.org/10.1016/j. ensm.2022.06.051.

[02] Najib, S., & Erdem, E. (2019). Current progress achieved in novel materials for supercapacitor electrodes: Mini review. Nanoscale Advances, 1(8), 2817–2827. https://doi.org/10.1039/c9na00345b.

[03] Borenstein, A., Hanna, O., Attias, R., Luski, S., Brousse, T., & Aurbach, D. (2017). Carbon-based composite materials for supercapacitor electrodes: A review. *Journal of Materials Chemistry A*, *5*(25), 12653–12672. https://doi.org/10.1039/c7ta00863e.

[04] Kar, K. K. (n.d.). *Springer Series in Materials Science 313 Handbook of Nanocomposite*

Supercapacitor Materials III. https://doi.org/10.1007/978-3-030-68364-1.

[05] Wu, Y., & Cao, C. (2018). *The way to improve the energy density of supercapacitors : Progress and perspective*. *June*, 1–10. https://doi.org/10.1007/s40843-018-9290-y.

[06] Wang, X. (2015). *Recent advances on multi-component hybrid nanostructures for electrochemical capacitors*. *August*. https://doi.org/10.1016/j.jpowsour.2015.06.062.

[07] Raza, W., Ali, F., Raza, N., Luo, Y., Kim, K., & Yang, J. (2018). Nano Energy Recent advancements in supercapacitor technology. *Nano Energy*, *52*(August), 441–473. https://doi.org/10.1016/j.nanoen.2018.08.013.

[08] Lukatskaya, M. R., Dunn, B., & Gogotsi, Y. (2016). architectures for future hybrid energy storage. *Nature Communications*, *7*, 1–13. https://doi.org/10.1038/ncomms12647.

[09] Guan, L., Yu, L., & Chen, G. Z. (2016). Electrochimica Acta Capacitive and non-capacitive faradaic charge storage. *Electrochimica Acta*, *206*, 464–478. https://doi.org/10.1016/j.electacta.2016.01.213.

[10] Biesheuvel, P. M., Porada, S., & Dykstra, J. E. (n.d.). *The difference between Faradaic and non-Faradaic electrode processes*. 1–16. https://doi.org/10.48550/arXiv.1809.02930.

[11] Wang, H., & Pilon, L. (2011). *Accurate Simulations of Electric Double Layer Capacitance of Ultramicroelectrodes*. 16711–16719. https://doi.org/10.1021/jp204498e.

[12] Lindberg, S. (2020). Charge storage mechanisms and interactions of hybrid supercapacitor electrode materials with next-generation electrolytes [Doctoral Thesis, Chalmers University of Technology].

[13] Bouty, E., & Helmholtz, E. B. H. (1879). *H . HELMHOLTZ . - Studien über electrische Grenzschichten (Études sur les couches électriques limites); Ann . der Physik , nouvelle série , t . VII , p . 337 ; 1879 To cite this version : HAL Id : jpa-00237563*.

[14] *Zhang, L. L., & Zhao, X. S. (2009). Carbon-based materials as supercapacitor electrodes. Chemical Society Reviews, 38(9), 2520–2531. https://doi.org/10.1039/B813846J*.

[15] Allagui, A., Benaoum, H., & Olendski, O. (2021). On the Gouy – Chapman – Stern model of the electrical double-layer structure with a generalized Boltzmann factor. *Physica A, 582*, 126252. https://doi.org/10.1016/j.physa.2021.126252.

[16] Su, Y., Fu, Y., Wei, Y., Yan, J., & Mao, B. (2010). *The Electrode / Ionic Liquid Interface : Electric Double Layer and Metal Electrodeposition*. 2764–2778. https://doi.org/10.1002/cphc.201000278.

[17] Grahame, D. C. (1952). Mathematical Theory of the Faradaic Admittance: Pseudocapacity and Polarization Resistance. Journal of The Electrochemical Society, 99(9), 370C–370C. https://doi.org/10.1149/1.2779638.

[18] Lukatskaya, M. R., Dunn, B., & Gogotsi, Y. (2016). Multidimensional materials and device architectures for future hybrid energy storage. *Nature Communications*, *7*(September), 1–13. https://doi.org/10.1038/ncomms12647.

[19] Mathis, T. S., Kurra, N., Wang, X., Pinto, D., & Simon, P. (2019). *Energy Storage Data Reporting in Perspective — Guidelines for Interpreting the Performance of Electrochemical Energy Storage Systems*. *1902007*, 1–13. https://doi.org/10.1002/aenm.201902007.

[20] Lukatskaya, M. R., Dunn, B., & Gogotsi, Y. (2016). Multidimensional materials and device architectures for future hybrid energy storage. *Nature Communications*, *7*(September), 1–13. https://doi.org/10.1038/ncomms12647.

[21] Wang, Y., Song, Y., & Xia, Y. (2016). Chem Soc Rev systems , characterization and applications chemical functional materials. *Chemical Society Reviews*, *45*, 5925–5950. https://doi.org/10.1039/C5CS00580A.

[22] Gruz, E. (1947). *J* -. Kinetics of rapid electrode reactions.

https://doi.org/10.1039/DF9470100011.

[23] Brousse, T., Soc, J. E., Brousse, T., & Daniel, B. (2015). *To Be or Not To Be Pseudocapacitive ? JES FOCUS ISSUE ON ELECTROCHEMICAL CAPACITORS :*

FUNDAMENTALS TO A PPLICATIONS To Be or Not To Be Pseudocapacitive ? https://doi.org/10.1149/2.0201505jes.

[24] Halper, M. S., & Ellenbogen, J. C. (2006). Supercapacitors: A brief overview (Report No. MP 05W0000272; Case No. 06-0667). MITRE. https://www.mitre.org/sites/default/files/pdf/06_0667.pdf.

[25] Simon, P., Gogotsi, Y., & Dunn, B. (2014). Where Do Batteries End and Supercapacitors Begin? Science, 343(6176), 1210–1211. https://doi.org/10.1126/science.124962.

[26] Chen, G. Z. (2022). *Perception of Supercapacitor and Supercapattery ECS Meeting Abstracts Perception of Supercapacitor and Supercapattery*. *October*, 18–20. https://doi.org/10.1149/MA2011-02/11/559.

[27] Chen, G. Z., & Chen, G. Z. (2016). Supercapacitor and supercapattery as emerging electrochemical energy stores Supercapacitor and supercapattery as emerging electrochemical energy stores. *International Materials Reviews*, *0*(0), 1–30. https://doi.org/10.1080/09506608.2016.1240914.

[28] Babu, B., Simon, P., & Balducci, A. (2020). *Fast Charging Materials for High Power Applications*. *2001128*. https://doi.org/10.1002/aenm.202001128.

[29] Gidwani, M., Bhagwani, A., & Rohra, N. (2014). Supercapacitors: the near Future of Batteries. International Journal of Engineering Inventions, 4(5), 22–27.

[30] Wang, G., Zhang, L., & Zhang, J. (2012). A review of electrode materials for electrochemical supercapacitors. Energy & Environmental Science, 5(8), 6828–6850. https://doi.org/10.1039/C2EE21035F.

[31] Kar, K. K. (n.d.). *Springer Series in Materials Science 313 Handbook of Nanocomposite Supercapacitor Materials III*. https://doi.org/10.1007/978-3-030-68364-1.

[32] Edlc, C. (n.d.). *Supercapacitors Based on Carbon or Pseudocapacitive Materials*. 1–25. DOI:10.1002/9781119007333.

[33] Calcagno, G. (2019). Mesoporous Titania for high rate electrochemical energy storage

[Licentiate thesis, Chalmers University of Technology].

[34] Malmberg, H. (2007). Nanoscientific investigations of electrode materials for supercapacitors [Doctoral thesis, KTH Royal Institute of Technology].

[35] Najib, S., & Erdem, E. (2019). Current progress achieved in novel materials for supercapacitor electrodes: Mini review. *Nanoscale Advances*, *1*(8), 2817–2827. https://doi.org/10.1039/c9na00345b.

[36] Dubey, R., Guruviah, V. Review of carbon-based electrode materials for supercapacitor energy storage. Ionics 25, 1419–1445 (2019). https://doi.org/10.1007/s11581-019-02874-0

[37] Patrice Simon and Andrew Burke 2008 Electrochem. Soc. Interface 17 38. *Nanostructured Carbons: Double-Layer Capacitance and More*. https:// doi.org/10.1149/2.F05081IF

[38] Jurewicz, K., Vix-guterl, C., Frackowiak, E., Saadallah, S., & Reda, M. (2004). *Capacitance properties of ordered porous carbon materials prepared by a templating procedure*. *65*, 287–293. https://doi.org/10.1016/j.jpcs.2003.10.024.

[39] Lu, W., Qu, L., Henry, K., & Dai, L. (2009). *High performance electrochemical capacitors from aligned carbon nanotube electrodes and ionic liquid electrolytes*. *189*, 1270–1277. https://doi.org/10.1016/j.jpowsour.2009.01.009.

[40] Talapatra, S., Kar, S., Pal, S. K., Vajtai, R., Ci, L., Victor, P., Shaijumon, M. M., Kaur, S., Nalamasu, O., & Ajayan, P. M. (2006). *Direct growth of aligned carbon nanotubes on bulk metals*. *1*(November), 18–22. https://doi.org/10.1038/nnano.2006.56.

[41] Worsley, M. A., & Baumann, T. F. (n.d.). *Carbon Aerogels*. https://doi.org/10.1007/978-3-319-19454-7.

[42] Lee, J., & Park, S. (2020). Recent advances in preparations and applications of carbon aerogels : A review. *Carbon*, *163*, 1–18. https://doi.org/10.1016/j.carbon.2020.02.073.

[43] Xia, J., Chen, F., Li, J., & Tao, N. (2009). Measurement of the quantum capacitance of graphene. *Nature Nanotechnology*, *4*(8), 505–509. https://doi.org/10.1038/nnano.2009.177.

[44] Wu, Z., Zhou, G., Yin, L., & Ren, W. (2012). Graphene / metal oxide composite electrode materials for energy storage. *Nano Energy*, *1*(1), 107–131. https://doi.org/10.1016/j.nanoen.2011.11.001.

[45] Cui, M., & Meng, X. (2018). Overview of transition metal-based composite materials for supercapacitor electrodes. Journal of Energy Storage, 15, 247–259. https://doi.org/10.1039/D0NA00573H.

[46] Jensen, J. (2015). TRANSITION METAL LAYERED DOUBLE HYDROXIDES FOR ENERGY STORAGE [Master's thesis, Queensland University of Technology].

[47] Chodankar, N. R., Pham, H. D., Nanjundan, A. K., Fernando, J. F. S., Jayaramulu, K., Golberg, D., Han, Y., & Dubal, D. P. (2020). *True Meaning of Pseudocapacitors and Their Performance Metrics : Asymmetric versus Hybrid Supercapacitors*. *2002806*, 1–35. https://doi.org/10.1002/smll.202002806.

[48] Das, T. K., & Prusty, S. (2012). Review on Conducting Polymers and Their Applications. Polymer-Plastics Technology and Engineering, 51(14), 1487–1500. https://doi.org/10.1080/03602559.2012.710697.

[49] Namsheer, K., & Rout, C. S. (2021). *RSC Advances Conducting polymers : a comprehensive review on recent advances in synthesis , properties and*. 5659–5697. https://doi.org/10.1039/d0ra07800j.

[50] Vangari, M., Pryor, T., & Jiang, L. (2013). *Supercapacitors : Review of Materials and Fabrication Methods*. *139*(2), 72–79. https://doi.org/10.1061/(ASCE)EY.1943-7897.0000102.

[51] Lindberg, S. (2020). Charge storage mechanisms and interactions of hybrid supercapacitor electrode materials with next-generation electrolytes [Doctoral Thesis, Chalmers University of Technology].

[52] Sajjad, M., Ibrar, M., Cheng, F., & Lu, W. (2021). A review on selection criteria of aqueous electrolytes performance evaluation for advanced asymmetric supercapacitors. *Journal of Energy Storage*, *40*(May), 102729. https://doi.org/10.1016/j.est.2021.102729.

[53] Tripathi, A. K., & Singh, R. K. (2019). *Chapter 6 Application of Ionic Liquids as a Green Material in Electrochemical Devices* (Issue August). https://doi.org/10.21741/9781644900314-6.

[54] Abdisattar, A., Yeleuov, M., Daulbayev, C., & Askaruly, K. (2022). Electrochemistry Communications Recent advances and challenges of current collectors for supercapacitors. *Electrochemistry Communications*, *142*(September), 107373. https://doi.org/10.1016/j.elecom.2022.107373.

[55] Wang, Y., Song, Y., & Xia, Y. (2016). Chem Soc Rev systems , characterization and applications chemical functional materials. *Chemical Society Reviews*, *45*, 5925–5950. https://doi.org/10.1039/C5CS00580A.

[56] Babu, B., Simon, P., & Balducci, A. (2020). *Fast Charging Materials for High Power Applications*. *2001128*. https://doi.org/10.1002/aenm.202001128.

[57] Simon, P., & Gogotsi, Y. (2012). Capacitive Energy Storage in Nanostructured Carbon–Electrolyte Systems. Accounts of Chemical Research, 46(5), 1094–1103. https://doi.org/10.1021/ar200262k.

[58] Gogotsi, Y., & Penner, R. M. (2018). Energy Storage in Nanomaterials—Capacitive, Pseudocapacitive, or Battery-like? ACS Nano, 12(7), 6299–6302. https://doi.org/10.1021/acsnano.8b04907.

[59] Babu, B., Simon, P., & Balducci, A. (2020). *Fast Charging Materials for High Power Applications*. *2001128*. https://doi.org/10.1002/aenm.202001128.

[60] Deblock, R. H. (n.d.). Achieving high energy density and high power density with pseudocapacitive materials. *Nature Reviews Materials*. https://doi.org/10.1038/s41578-019-0142-z.

[61] Bekki, K., Star, M., Form, C., Lee, J., & Shin, E. (n.d.). *A review on Supercapacitors : types and components A review on Supercapacitors : types and components*. https://doi.org/10.1088/1742-6596/1973/1/012015.

[62] Gualous, H., & Gallay, R. (2007, 10 août). Applications des supercondensateurs. Techniques de l'Ingénieur. https://www.techniques-ingenieur.fr/base-documentaire/electrotechnique-electronique-th7/applications-des-supercondensateurs-ti724/applications-des-supercondensateurs-dossier-complet-e3355/.

[63] M.E. Şahin, F. Blaabjerg, A. Sangwongwanich. A review on supercapacitormaterials and developments. Turk. J. Mater. 5(2) (2020) 10-24.

[64] Miller, J. R., & Burke, A. (2008). Electrochemical Capacitors: Challenges and Opportunities for Real-World Applications. The Electrochemical Society Interface, 17(1), 53. https://doi.org/10.1149/2.F08081IF.

[65] Kar, K. K. (n.d.). *Springer Series in Materials Science 300 Handbook of Nanocomposite Supercapacitor Materials I*. https://doi.org/10.1007/978-3-030-43009-2.

[66] Fu, X., Cai, J., Zhang, X., Li, W., Ge, H., & Hu, Y. (2018). Top-down fabrication of shape-controlled , monodisperse nanoparticles for biomedical applications ☆. *Advanced Drug Delivery Reviews*. https://doi.org/10.1016/j.addr.2018.07.006.

[67] Mekuye, B. (2023). *Nanomaterials : An overview of synthesis , classification , characterization , and applications*. *March*, 486–501. https://doi.org/10.1002/nano.202300038.

[68] Mathew, E., Kumar, S., Purohit, R., Dhakad, S. K., & Rana, R. S. (2020). Materials Today : Proceedings Nanolithography and its current advancements. *Materials Today: Proceedings*, *xxxx*. https://doi.org/10.1016/j.matpr.2020.02.505.

[69] Yadav, T. P., Yadav, R. M., & Singh, D. P. (2012). *Mechanical Milling : a Top Down Approach for the Synthesis of Nanomaterials and Nanocomposites*. *2*(3), 22–48. https://doi.org/10.5923/j.nn.20120203.01.

[70] Gu, D. (2005). *Ball-milling in liquid media Applications to the preparation of anodic materials for lithium-ion batteries*. *50*, 1–92. https://doi.org/10.1016/S0079-6425(03)00050-1.

[71] Gorrasi, G., & Sorrentino, A. (2015). *Mechanical milling as a technology to produce structural and functional bio-nanocomposites*. https://doi.org/10.1039/c5gc00029g.

[72] Sergievskaya, A., Chauvin, A., & Konstantinidis, S. (2022). *Sputtering onto liquids : a critical review*. 10–53. https://doi.org/10.3762/bjnano.13.2.

[73] Wender, H., Migowski, P., Feil, A. F., Teixeira, S. R., & Dupont, J. (2013). Sputtering deposition of nanoparticles onto liquid substrates : Recent advances and future trends. *Coordination Chemistry Reviews*, *257*(17–18), 2468–2483. https://doi.org/10.1016/j.ccr.2013.01.013.

[74] Ayyub, P., Chandra, R., Taneja, P., Sharma, A. K., & Pinto, R. (2001). *Synthesis of nanocrystalline material by sputtering and laser ablation at low temperatures*. *June 2014*. https://doi.org/10.1007/s003390100833.

[75] Letters, G. C., Ijaz, I., Gilani, S. E., & Nazir, A. (2020). *Detail review on chemical , physical and green synthesis , classification , characterizations and applications of nanoparticles*. *July*. https://doi.org/10.1080/17518253.2020.1802517.

[76] Sun, L., & Hong, B. H. (2021). Chemical vapour deposition. *Nature Reviews Methods Primers*, *0123456789*. https://doi.org/10.1038/s43586-020-00005-y.

[77] Bokov, D., Jalil, A. T., Chupradit, S., Suksatan, W., Ansari, M. J., Shewael, I. H., Valiev, G. H., & Kianfar, E. (2021). *Nanomaterial by Sol-Gel Method : Synthesis and Application*. *2021*. https://doi.org/10.1155/2021/5102014.

[78] Pena-pereira, F., Duarte, R. M. B. O., & Duarte, A. C. (2012). Immobilization strategies and analytical applications for metallic and metal-oxide nanomaterials on surfaces. *Trends in Analytical Chemistry*, *40*, 90–105. https://doi.org/10.1016/j.trac.2012.07.015.

[79] Richetta, M., Pg, M., Mattoccia, A., Varone, A., & Pizzoferrato, R. (2017). *Journal of Material Sciences & Engineering Layered Double Hydroxides : Tailoring Interlamellar Nanospace for a Vast Field of Applications*. *6*(4). https://doi.org/10.4172/2169-0022.1000360.

[80] Habib, N. (2022). Nanohybrides à base des Hydroxydes et/ou MWNTs pour le Stockage d'Energie [Doctoral thesis, Badji Mokhtar-Annaba University].

[81] Wang, X., Zhang, J., Yang, S., Yan, H., Hong, X., Dong, W., Liu, Y., Zhang, B., & Wen, Z. (2018). Interlayer Space Regulating of NiMn Layered Double Hydroxides for Abstract : *Electrochimica Acta*. https://doi.org/10.1016/j.electacta.2018.10.021.

[82] Lee, I., Hwa, G., An, S., Kim, S., & Yoon, S. (2018). Applied Surface Science Facile synthesis of 3D MnNi-layered double hydroxides (LDH)/ graphene composites from directly graphites for pseudocapacitor and their electrochemical analysis. *Applied Surface Science*, *429*, 196–202. https://doi.org/10.1016/j.apsusc.2017.06.259.

[83] Chen, H., Ai, Y., Liu, F., Chang, X., Xue, Y., Huang, Q., Wang, C., Lin, H., & Han, S. (2016). Electrochimica Acta Carbon-coated Hierarchical Ni – Mn Layered Double Hydroxide Nanoarrays on Ni Foam for Flexible High-capacitance Supercapacitors. *Electrochimica Acta*, *213*, 55–65. https://doi.org/10.1016/j.electacta.2016.06.038.

[84] Habib, N., Guellati, O., Merzoug, A. H. A. N., Haskouri, J. El, & Manyala, D. M. N. (2019). Ni – Zn hydroxide - based bi - phase multiscale porous nanohybrids : physico - chemical properties. *Applied Nanoscience*, *0123456789*. https://doi.org/10.1007/s13204-019-01062-w.

[85] Mukherji, A., Saikia, L., & Srivastava, R. (2019). Few-layer MoS2 wrapped MnCO3 on graphite paper : A hydrothermally grown hybrid negative electrode for electrochemical energy storage Few-layer MoS 2 wrapped MnCO 3 on graphite paper : A hydrothermally grown hybrid negative electrode for electrochemical energy storage. *Chemical Engineering Journal*, *373*(May), 1233–1246. https://doi.org/10.1016/j.cej.2019.05.133.

[86] Zang, X., Dai, Z., Guo, J., Dong, Q., Yang, J., Huang, W., & Dong, X. (2016). *Controllable synthesis of triangular Ni (HCO 3) 2 nanosheets for supercapacitor*. https://doi.org/10.1007/s12274-016-1031-z.

[87] Adams, F. (2005). X-ray absorption and diffraction—Overview. In P. J. Worsfold (Ed.), Encyclopedia of analytical science (2nd ed., Vol. 9, pp. 365–378). Elsevier. https://hdl.handle.net/10067/497110151162165141.

[88] Bergström, J. (2015). Experimental Characterization Techniques. In Mechanics of Solid Polymers (pp. 37–120). Elsevier. https://doi.org/10.1016/B978-0-323-31150-2.00002-9.

[89] Khan, S. A., Khan, S. B., Khan, L. U., & Farooq, A. (2018). *Fourier Transform Infrared Spectroscopy : Fundamentals and Application in Functional Groups and Nanomaterials Characterization Fourier Transform Infrared Spectroscopy : Fundamentals and Application in Functional Groups and Nanomaterials Characterization*. *July 2020*. https://doi.org/10.1007/978-3-319-92955-2.

[90] Veerasingam, S., Ranjani, M., Venkatachalapathy, R., Bagaev, A., Litvinyuk, D., Mugilarasan, M., Gurumoorthi, K., Guganathan, L., Aboobacker, V. M., & Vethamony, P. (2021). Technology Contributions of Fourier transform infrared spectroscopy in microplastic pollution research : A review. *Critical Reviews in Environmental Science and Technology*, *51*(22), 2681–2743. https://doi.org/10.1080/10643389.2020.1807450.

[91] Jones RR, Hooper DC, Zhang L, Wolverson D, Valev VK. Raman Techniques: Fundamentals and Frontiers. Nanoscale Res Lett. 2019 Jul 12;14(1):231. doi: 10.1186/s11671-019-3039-2. PMID: 31300945; PMCID: PMC6626094.

[92] Cong, X., Liu, X., Lin, M., & Tan, P. (2020). Application of Raman spectroscopy to probe fundamental properties of two-dimensional materials. *Npj 2D Materials and Applications*, 1–12. https://doi.org/10.1038/s41699-020-0140-4.

[93] Sci, J. V., Stevie, F. A., & Donley, C. L. (2020). *Introduction to x-ray photoelectron spectroscopy Introduction to x-ray photoelectron spectroscopy*. *063204*(August). https://doi.org/10.1116/6.0000412.

[94] Isaacs, M. A., Davies-jones, J., Davies, P. R., Guan, S., Lee, R., Morgan, J., Palgrave, R., & Davies-jones, J. (2021). *MATERIALS CHEMISTRY FRONTIERS Advanced XPS characterization : XPS-based multi-technique analyses for comprehensive understanding of functional materials*. https://doi.org/10.1039/d1qm00969a.

[95] Jaroniec, M., Kruk, M., & Sayari, A. (1998). Adsorption methods for characterization of surface and structural properties of mesoporous molecular sieves. In *Mesoporous molecular sieves 1998* (Vol. 117, Issue 100). Elsevier Masson SAS. https://doi.org/10.1016/S0167-2991(98)81008-2.

[96] Naderi, M. (2015). Surface Area: Brunauer–Emmett–Teller (BET). In Progress in Filtration and Separation (pp. 585–608). ScienceDirect. https://doi.org/10.1016/B978-0-12-384746-1.00014-8.

[97] Ambroz, F., Macdonald, T. J., Martis, V., & Parkin, I. P. (2018). *Evaluation of the BET Theory for the Characterization of Meso and Microporous MOFs*. *1800173*, 1–17. https://doi.org/10.1002/smtd.201800173.

[98] Vogt, C., Wondergem, C.S., Weckhuysen, B.M. (2023). Ultraviolet-Visible (UV-Vis) Spectroscopy. In: Wachs, I.E., Bañares, M.A. (eds) Springer Handbook of Advanced Catalyst Characterization. Springer Handbooks. Springer, Cham. https://doi.org/10.1007/978-3-031-07125-6_11.

[99] Akash, M. S. H., & Rehman, K. (2020). *Essentials of Pharmaceutical Analysis*. Springer Nature Singapore. https://doi.org/10.1007/978-981-96-5996-8.

[100] Vladár, A. E., & Hodoroaba, V. (2020). Characterization of nanoparticles by scanning electron microscopy. In *Characterization of Nanoparticles*. Elsevier Inc. https://doi.org/10.1016/B978-0-12-814182-3.00002-X.

[101] Akhtar, K., Khan, S.A., Khan, S.B., Asiri, A.M. (2018). Scanning Electron Microscopy: Principle and Applications in Nanomaterials Characterization. In: Sharma, S. (eds) Handbook of Materials Characterization. Springer, Cham. https://doi.org/10.1007/978-3-319-92955-2_4.

[102] Everhart, T. E., & Thornley, R. F. M. (1960). Wide-band detector for micro-microampere low-energy electron currents. Journal of Scientific Instruments, 37(7), 246–248. DOI 10.1088/0950-7671/37/7/307.

[103] Mast, J., Verleysen, E., Hodoroaba, V., & Kaegi, R. (2020). Characterization of nanomaterials by transmission electron microscopy : Measurement procedures. In *Characterization of Nanoparticles*. Elsevier Inc. https://doi.org/10.1016/B978-0-12-814182-3.00004-3.

[104] Franken, L. E., Grünewald, K., Boekema, E. J., & Stuart, M. C. A. (2020). *A Technical Introduction to Transmission Electron Microscopy for Soft-Matter : Imaging , Possibilities , Choices , and Technical Developments*. *1906198*. https://doi.org/10.1002/smll.201906198.

[105] Lin, Y., Zhou, M., Tai, X., Li, H., Han, X., & Yu, J. (2021). ll Review Analytical transmission electron microscopy for emerging advanced materials. *Matter*, 1–31. https://doi.org/10.1016/j.matt.2021.05.005.

[106] Ahmed Khan, I., Thekkekara, L., Waqar, S., Choudhry, N., & John, S. (2022). Supercapacitors Fabrication and Performance Evaluation Techniques. *Supercapacitors for the Next Generation*. https://doi.org/10.5772/intechopen.101748.

[107] Ying, X., Zhou, H., Hu, J., Xu, Y., Zeng, J., Chen, J., & Kuang, Y. (2009). Electrochemical behavior of K4Fe(CN)6 in [bmim]PF6/TX-100/H2O based microemulsions. *Journal of Applied Electrochemistry*, *39*(8), 1273–1278. https://doi.org/10.1007/s10800-009-9795-4.

[108] Li, Q., Horn, M., Wang, Y., MacLeod, J., Motta, N., & Liu, J. (2019). A review of supercapacitors based on graphene and redox-active organic materials. *Materials*, *12*(5). https://doi.org/10.3390/ma12050703.

[109] Zhao, Y., Hu, L., Zhao, S., & Wu, L. (2016). Preparation of MnCo2O4@Ni(OH)2 Core–Shell Flowers for Asymmetric Supercapacitor Materials with Ultrahigh Specific Capacitance. *Advanced Functional Materials*, *26*(23), 4085–4093. https://doi.org/10.1002/adfm.201600494.

[110] Xia, Q. X., San Hui, K., Hui, K. N., Kim, S. D., Lim, J. H., Choi, S. Y., Zhang, L. J., Mane, R. S., Yun, J. M., & Kim, K. H. (2015). Facile synthesis of manganese carbonate quantum dots/Ni(HCO3)2-MnCO3 composites as advanced cathode materials for high energy density asymmetric supercapacitors. *Journal of Materials Chemistry A*, *3*(44), 22102–22117. https://doi.org/10.1039/c5ta04005a.

[111] Zang, X., Dai, Z., Guo, J. et al. Controllable synthesis of triangular Ni(HCO3)2 nanosheets for supercapacitor. Nano Res. 9, 1358–1365 (2016). https://doi.org/10.1007/s12274-016-1031-z.

[112] Mukherji, A., Saikia, L., & Srivastava, R. (2019). Few-layer MoS2 wrapped MnCO3 on graphite paper : A hydrothermally grown hybrid negative electrode for electrochemical energy storage Few-layer MoS 2 wrapped MnCO 3 on graphite paper : A hydrothermally grown hybrid

negative electrode for electrochemical energy storage. *Chemical Engineering Journal*, *373*(May), 1233–1246. https://doi.org/10.1016/j.cej.2019.05.133.

[113] Adil, S. F., Assal, M. E., Kuniyil, M., Khan, M., Shaik, M. R., Alwarthan, A., Labis, J. P., & Siddiqui, M. R. H. (2017). Synthesis and comparative catalytic study of zinc oxide (ZnOx) nanoparticles promoted MnCO3, MnO2and Mn2O3for selective oxidation of benzylic alcohols using molecular oxygen. *Materials Express*, *7*(2), 79–92. https://doi.org/10.1166/mex.2017.1357.

[114] Chandra Sekhar, S., Nagaraju, G., & Yu, J. S. (2018). Ant-cave structured MnCO 3 /Mn 3 O 4 microcubes by biopolymer-assisted facile synthesis for high-performance pseudocapacitors. *Applied Surface Science*, *435*, 398–405. https://doi.org/10.1016/j.apsusc.2017.11.095.

[115] Cheng, D., Zhong, Q., Xiong, Y., Bu, Y., & Wang, J. (2020). Co(OH)2 particles decorated Ni3(NO3)1.6(CO3)0.2(OH)4 flower-like composite electrode for high-performance hybrid supercapacitors. *Journal of Alloys and Compounds*, *817*, 152689. https://doi.org/10.1016/j.jallcom.2019.152689.

[116] Feng, L., Sun, J., Liu, Y., Li, X., Ye, L., & Zhao, L. (2018). 3D sponge-like porous structure of Mn2O3 tiny nanosheets coated on Ni(OH)2/Mn2O3 nanosheet arrays for quasi-solid-state asymmetric supercapacitors with high performance. *Chemical Engineering Journal*, *339*(January), 61–70. https://doi.org/10.1016/j.cej.2018.01.123.

[117] Sreenavya, S. A., Baskaran, B. T., Ganesh, G. V., Sharma, S. D., Kulal, N., & Sakthivel, S. A. (2018). Framework of ruthenium-containing nickel hydrotalcite-type material: preparation, characterisation, and its catalytic application. *RSC Advances*, *8*(44), 25248–25257. https://doi.org/10.1039/c8ra03506g.

[118] Giovannelli, F., Zaghrioui, M., Autret-Lambert, C., Delorme, F., Seron, A., Chartier, T., & Pignon, B. (2012). Magnetic properties of Ni(II)-Mn(III) LDHs. *Materials Chemistry and Physics*, *137*(1), 55–60. https://doi.org/10.1016/j.matchemphys.2012.07.057.

[119] Abitkar, S. B., Dhas, S. D., Jadhav, N. P., Jadhav, P. R., Maldar, P. S., Patil, C. E., & Moholkar, A. V. (2021). Enhanced specific capacitance and electrochemical properties of nickel hydroxide-activated carbon (α-Ni(OH)2–AC) nanocomposite for pseudocapacitor electrode material. *Journal of Materials Science: Materials in Electronics*, *32*(7), 8657–8667. https://doi.org/10.1007/s10854-021-05529-x.

[120] Larbi, T., Ben Said, L., Ben Daly, A., Ouni, B., Labidi, A., & Amlouk, M. (2016). Ethanol sensing properties and photocatalytic degradation of methylene blue by Mn3O4, NiMn2O4 and alloys of Ni-manganates thin films. *Journal of Alloys and Compounds*, *686*, 168–175. https://doi.org/10.1016/j.jallcom.2016.06.001.

[121] Karuppaiah, M., Sakthivel, P., Asaithambi, S., Murugan, R., babu, G. A., Yuvakkumar, R., & Ravi, G. (2019). Solvent dependent morphological modification of micro-nano assembled Mn2O3/NiO composites for high performance supercapacitor applications. *Ceramics International*, *45*(4), 4298–4307. https://doi.org/10.1016/j.ceramint.2018.11.104.

[122] Bernard, M. C., & Goff, A. H. Le. (1993). Electrochemical science and technology: Electrochromic Reactions in Manganese Oxides: I. Raman Analysis. *Journal of the Electrochemical Society*, *140*(11), 3065–3070. DOI 10.1149/1.2220986.

[123] Hall, D. S., Lockwood, D. J., Bock, C., & MacDougall, B. R. (2015). Nickel hydroxides and related materials: A review of their structures, synthesis and properties. *Proceedings of the Royal Society A: Mathematical, Physical and Engineering Sciences*, *471*(2174). https://doi.org/10.1098/rspa.2014.0792.

[124] Du, J., Zou, Z., Yu, A., & Xu, C. (2018). Selenization of NiMn-layered double hydroxide with enhanced electrocatalytic activity for oxygen evolution. *Dalton Transactions*, *47*(22), 7492–7497. https://doi.org/10.1039/c8dt01372a.

[125] Naik, K. K., Bhuyan, R. K., & Mohapatra, A. K. (2020). Array of NiMn2O4 nanosheets for glucose sensing application. *Journal of Materials Science: Materials in Electronics*, *31*(22), 19691–19697. https://doi.org/10.1007/s10854-020-04495-0.

[126] Liu, G., Huang, C., Yang, Z., Su, J., & Zhang, W. (2021). Ultrathin NiMn-LDH nanosheet structured electrocatalyst for enhanced electrocatalytic urea oxidation. *Applied Catalysis A: General*, *614*(December 2020), 118049. https://doi.org/10.1016/j.apcata.2021.118049.

[127] Karuppaiah, M., Sakthivel, P., Asaithambi, S., Murugan, R., Yuvakkumar, R., & Ravi, G. (2019). Formation of one dimensional nanorods with microsphere of MnCO 3 using Ag as dopant to enhance the performance of pseudocapacitors. *Materials Chemistry and Physics*, *228*(January), 1–8. https://doi.org/10.1016/j.matchemphys.2019.02.034.

[128] Yu, M., Liu, R., Liu, J., Li, S., & Ma, Y. (2017). Polyhedral-Like NiMn-Layered Double Hydroxide/Porous Carbon as Electrode for Enhanced Electrochemical Performance Supercapacitors. *Small*, *13*(44), 1–9. https://doi.org/10.1002/smll.201702616.

[129] Rahman, M. M., Alam, M. M., & Asiri, A. M. (2019). Potential application of mixed metal oxide nanoparticle-embedded glassy carbon electrode as a selective 1,4-dioxane chemical sensor probe by an electrochemical approach. *RSC Advances*, *9*(72), 42050–42061. https://doi.org/10.1039/c9ra09118a.

[130] Vardhan Palem, V., Balarabe Idris, M., Subramaniam, T., & Sappani, D. (2020). The Charge Storage Mechanism of MnCO3 in Aqueous Electrolytes. *ChemistrySelect*, *5*(17), 5316–5322. https://doi.org/10.1002/slct.201904720.

[131] Zhou, J., Min, M., Liu, Y., Tang, J., & Tang, W. (2018). Layered assembly of NiMn-layered double hydroxide on graphene oxide for enhanced non-enzymatic sugars and hydrogen peroxide detection. *Sensors and Actuators, B: Chemical*, *260*, 408–417. https://doi.org/10.1016/j.snb.2018.01.072.

[132] Sun, M. H., Huang, S. Z., Chen, L. H., Li, Y., Yang, X. Y., Yuan, Z. Y., & Su, B. L. (2016). Applications of hierarchically structured porous materials from energy storage and conversion, catalysis, photocatalysis, adsorption, separation, and sensing to biomedicine. *Chemical Society Reviews*, *45*(12), 3479–3563. https://doi.org/10.1039/c6cs00135a.

[133] Vishnu Vardhan, P., Jothilakshmi, C., Kamachi Mudali, U., & Devaraj, S. (2017). The Effect of Carbonate Precursors on the Capacitance Properties of MnCO3. *Materials Today: Proceedings*, *4*(13), 12407–12415. https://doi.org/10.1016/j.matpr.2017.10.011.

[134] Singh, S., Shinde, N. M., Xia, Q. X., Gopi, C. V. V. M., Yun, J. M., Mane, R. S., & Kim, K. H. (2017). Tailoring the morphology followed by the electrochemical performance of NiMn-LDH nanosheet arrays through controlled Co-doping for high-energy and power asymmetric supercapacitors. *Dalton Transactions*, *46*(38), 12876–12883. https://doi.org/10.1039/c7dt01863k.

[135] Wang, S., Liu, H., Li, Z., & Zhu, J. (2019). Facile preparation of Ni-Mn layered double hydroxide nanosheets/carbon for supercapacitor. *Journal of Materials Science: Materials in Electronics*, *30*(8), 7524–7533. https://doi.org/10.1007/s10854-019-01066-w.

[136] Rajendiran, R., Muthuchamy, N., Park, K. H., Li, O. L., Kim, H. J., & Prabakar, K. (2020). Self-assembled 3D hierarchical MnCO3/NiFe layered double hydroxides as a superior electrocatalysts for the oxygen evolution reactions. *Journal of Colloid and Interface Science*, *566*, 224–233. https://doi.org/10.1016/j.jcis.2020.01.086.

[137] Tian, D., Lu, X., Nie, G., Gao, M., & Wang, C. (2018). Direct growth of Ni-Mn-O nanosheets on flexible electrospun carbon nanofibers for high performance supercapacitor applications. *Inorganic Chemistry Frontiers*, *5*(3), 635–642. https://doi.org/10.1039/c7qi00696a.

[138] Tang, Y., Shen, H., Cheng, J., Liang, Z., Qu, C., Tabassum, H., & Zou, R. (2020). Fabrication of Oxygen-Vacancy Abundant NiMn-Layered Double Hydroxides for Ultrahigh Capacity Supercapacitors. *Advanced Functional Materials*, *30*(11), 1–9. https://doi.org/10.1002/adfm.201908223.

[139] Chen, X., Paul, R., & Dai, L. (2017). Carbon-based supercapacitors for efficient energy storage. *National Science Review*, *4*(3), 453–489. https://doi.org/10.1093/nsr/nwx009.

[140] Pan, Z., Yang, J., Kong, J., Loh, X. J., Wang, J., & Liu, Z. (2022). "Porous and Yet Dense" Electrodes for High-Volumetric-Performance Electrochemical Capacitors: Principles, Advances, and Challenges. *Advanced Science*, *9*(4). https://doi.org/10.1002/advs.202103953.

[141] Nguyen Dinh, M. T., Nguyen, C. C., Truong Vu, T. L., Ho, V. T., & Truong, Q. D. (2020). Tailoring porous structure, reducibility and Mn4+ fraction of ε-MnO2 microcubes for the complete oxidation of toluene. *Applied Catalysis A: General*, *595*(October 2019), 117473. https://doi.org/10.1016/j.apcata.2020.117473.

[142] Chen, H., Zhou, W., Zhu, D., Liu, Z., Feng, Z., Li, J., & Chen, Y. (2020). Porous cube-like Mn3O4@C as an advanced cathode for low-cost neutral zinc-ion battery. *Journal of Alloys and Compounds*, *813*, 151812. https://doi.org/10.1016/j.jallcom.2019.151812.

[143] Ge, Y., Kan, K., Yang, Y., Zhou, L., Jing, L., Shen, P., Li, L., & Shi, K. (2014). Highly mesoporous hierarchical nickel and cobalt double hydroxide composite: Fabrication, characterization and ultrafast NOx gas sensors at room temperature. *Journal of Materials Chemistry A*, *2*(14), 4961–4969. https://doi.org/10.1039/c3ta14607c.

[144] Boufas, M., Guellati, O., Harat, A., Momodu, D., Dangbegnon, J., Manyala, N., & Guerioune, M. (2020). Optical and electrochemical properties of iron oxide and hydroxide nanofibers synthesized using new template-free hydrothermal method. *Journal of Nanostructure in Chemistry*, *10*(4), 275–288. https://doi.org/10.1007/s40097-020-00348-8.

[145] Makuła, P., Pacia, M., & Macyk, W. (2018). How To Correctly Determine the Band Gap Energy of Modified Semiconductor Photocatalysts Based on UV-Vis Spectra. *Journal of Physical Chemistry Letters*, *9*(23), 6814–6817. https://doi.org/10.1021/acs.jpclett.8b02892.

[146] Kareem Jassem, E., Mustafa Abdul Majeed, A., & Mossa Umran, N. (2019). The Effect of Temperature on Structural and optical properties of Manganese Oxide Nanoparticles. *Journal of Physics: Conference Series*, *1279*(1). https://doi.org/10.1088/1742-6596/1279/1/012004.

[147] Konopka, S. J., & McDuffie, B. (1970). Diffusion Coefficients of Ferri- and Ferrocyanide Ions in Aqueous Media, Using Twin-Electrode Thin-Layer Electrochemistry. *Analytical Chemistry*, *42*(14), 1741–1746. https://doi.org/10.1021/ac50160a042.

[148] Gan, Y. X., Jayatissa, A. H., Yu, Z., Chen, X., & Li, M. (2020). Hydrothermal Synthesis of Nanomaterials. *Journal of Nanomaterials*, *2020*. https://doi.org/10.1155/2020/8917013.

[149] Bazán, J. C., & Arvia, A. J. (1965). The diffusion of ferro- and ferricyanide ions in aqueous solutions of sodium hydroxide. *Electrochimica Acta*, *10*(10), 1025–1032. https://doi.org/10.1016/0013-4686(65)80014-7.

[150] Brett, A., Maria, A. N. A., & Ra, O. (1994). *Book Reviews Electrochemistry. Principles, Methods, and Applications*. *39*(6), 854. https://doi.org/10.1002/anie.199419892.

[151] Zhu, P., & Zhao, Y. (2019). Cyclic voltammetry measurements of electroactive surface area of porous nickel: Peak current and peak charge methods and diffusion layer effect. *Materials Chemistry and Physics*, *233*(May), 60–67. https://doi.org/10.1016/j.matchemphys.2019.05.034.

[152] Paixão, T. R. L. C. (2020). Measuring Electrochemical Surface Area of Nanomaterials versus the Randles−Ševčík Equation. *ChemElectroChem*, *7*(16), 3414–3415. https://doi.org/10.1002/celc.202000633.

[153] Yuan, Y., Zhou, J., Rafiq, M. I., Dai, S., Tang, J., & Tang, W. (2019). Growth of Ni–Mn layered double hydroxide and polypyrrole on bacterial cellulose nanofibers for efficient supercapacitors. In *Electrochimica Acta* (Vol. 295). Elsevier Ltd. https://doi.org/10.1016/j.electacta.2018.10.090.

[154] Devaraj, S., Vardhan, P. V., Liu, H. Y., & Balaya, P. (2016). Metal carbonates: alternative to metal oxides for supercapacitor applications? A case study of MnCO3 vs MnO2. *Journal of Solid State Electrochemistry*, *20*(7), 1877–1883. https://doi.org/10.1007/s10008-015-2972-y.

[155] L. Soserov, A. Stoyanova, T. Boyadzhieva, V. Koleva, M. Kalapsazova, R. Stoyanova, Nickel-manganese structured and multiphase composites as electrodes for hybrid supercapacitors, Electrochimica Acta (2018), doi: 10.1016/j.electacta.2018.06.191.

[156] Wang, F., Wu, X., Yuan, X., Liu, Z., Zhang, Y., Fu, L., Zhu, Y., Zhou, Q., Wu, Y., & Huang, W. (2017). Latest advances in supercapacitors: From new electrode materials to novel device designs. *Chemical Society Reviews*, *46*(22), 6816–6854. https://doi.org/10.1039/c7cs00205j.

[157] Yuan, Y., Liu, Z., Wei, B., Yang, Z., Wang, L., & Fei, W. (2020). Effects of high-shear mixing and the graphene oxide weight fraction on the electrochemical properties of the GO/Ni(OH)2 electrode. *Dalton Transactions*, *49*(6), 1752–1764. https://doi.org/10.1039/c9dt04525b.

[158] Kettaf, S., Guellati, O., Harat, A., Kennaz, H., Momodu, D., Dangbegnon, J., Manyala, N., & Guerioune, M. (2019). Electrochemical measurements of synthesized nanostructured β-Ni(OH)2 using hydrothermal process and activated carbon based nanoelectroactive materials. *SN Applied Sciences*, *1*(1). https://doi.org/10.1007/s42452-018-0038-3.

[159] Karthik, R., Sukanya, R., Chen, S. M., Hasan, M., Dhakal, G., Shafi, P. M., & Shim, J. J. (2023). Development of an Amorphous Nickel Boride/Manganese Molybdate Heterostructure as an Efficient Electrode Material for a High-Performance Asymmetric Supercapacitor. *ACS Applied Materials and Interfaces*, *15*(9), 11927–11939. https://doi.org/10.1021/acsami.3c00013.

[160] Yu, S., Zhang, Y., Lou, G., Wu, Y., Zhu, X., Chen, H., Shen, Z., Fu, S., Bao, B., & Wu, L. (2018). Synthesis of NiMn-LDH Nanosheet@Ni3S2 Nanorod Hybrid Structures for Supercapacitor Electrode Materials with Ultrahigh Specific Capacitance. *Scientific Reports*, *8*(1), 1–12. https://doi.org/10.1038/s41598-018-23642-6.

[161] Su, D., Tang, Z., Xie, J., Bian, Z., Zhang, J., Yang, D., Zhang, D., Wang, J., Liu, Y., Yuan, A., & Kong, Q. (2019). Co, Mn-LDH nanoneedle arrays grown on Ni foam for high performance supercapacitors. *Applied Surface Science*, *469*, 487–494. https://doi.org/10.1016/j.apsusc.2018.10.276.

[162] Wu, Q., He, T., Zhang, Y., Zhang, J., Wang, Z., Liu, Y., Zhao, L., Wu, Y., & Ran, F. (2021). Cyclic stability of supercapacitors: materials, energy storage mechanism, test methods,

and device. *Journal of Materials Chemistry A*, *9*(43), 24094–24147. https://doi.org/10.1039/d1ta06815f.

[163] Simon, P., & Gogotsi, Y. (2011). *Carbon À Electrolyte Systems*. *XXX*(Xx).

[164] Najib, S., & Erdem, E. (2019). Current progress achieved in novel materials for supercapacitor electrodes: Mini review. *Nanoscale Advances*, *1*(8), 2817–2827. https://doi.org/10.1039/c9na00345b.

[165] Wu, Q., He, T., Zhang, Y., Zhang, J., Wang, Z., Liu, Y., Zhao, L., Wu, Y., & Ran, F. (2021). Cyclic stability of supercapacitors: materials, energy storage mechanism, test methods, and device. *Journal of Materials Chemistry A*, *9*(43), 24094–24147. https://doi.org/10.1039/d1ta06815f.

[166] Li, W., Li, Y., Meng, Q., Xu, Y., Yang, B., & Li, T. (2020). Facile Preparation of a Ni/Mn-LDH Nanosheet @Graphene Foam Hierarchical Structure for High-performance Flexible Supercapacitors. *Materials Research Bulletin*, *129*(September 2019), 110889. https://doi.org/10.1016/j.materresbull.2020.110889.

[167] Wang, S., Li, Q., Pu, W., Wu, Y., & Yang, M. (2016). Development of monodispersed MnCO3/graphene nanosheet composite as anode for lithium-ion battery by hydrothermal synthesis. *Ionics*, *22*(6), 771–778. https://doi.org/10.1007/s11581-015-1615-8.

[168] Naik, K. K., Bhuyan, R. K., & Mohapatra, A. K. (2020). Array of NiMn2O4 nanosheets for glucose sensing application. *Journal of Materials Science: Materials in Electronics*, *31*(22), 19691–19697. https://doi.org/10.1007/s10854-020-04495-0.

[169] Elkholy, A. E., El-Taib Heakal, F., & Allam, N. K. (2019). A facile electrosynthesis approach of amorphous Mn-Co-Fe ternary hydroxides as binder-free active electrode materials for high-performance supercapacitors. *Electrochimica Acta*, *296*, 59–68. https://doi.org/10.1016/j.electacta.2018.11.038.

[170] Guo, Y., Hong, X., Wang, Y., Li, Q., Meng, J., Dai, R., Liu, X., He, L., & Mai, L. (2019). Multicomponent Hierarchical Cu-Doped NiCo-LDH/CuO Double Arrays for Ultralong-Life Hybrid Fiber Supercapacitor. *Advanced Functional Materials*, *29*(24), 1–11. https://doi.org/10.1002/adfm.201809004.

[171] Habib, N., Guellati, O., Merzoug, A. H. A. N., Haskouri, J. El, & Manyala, D. M. N. (2019). Ni – Zn hydroxide - based bi - phase multiscale porous nanohybrids : physico - chemical properties. *Applied Nanoscience*, *0123456789*. https://doi.org/10.1007/s13204-019-01062-w.

[172] Zhang, B., Li, X., Zou, J., & Kim, F. (2020). MnCO3on Graphene Porous Framework via Diffusion-Driven Layer-by-Layer Assembly for High-Performance Pseudocapacitor. *ACS Applied Materials and Interfaces*, *12*(42), 47695–47703. https://doi.org/10.1021/acsami.0c15511.

[173] Liu, P. F., Zhou, J. J., Li, G. C., Wu, M. K., Tao, K., Yi, F. Y., Zhao, W. N., & Han, L. (2017). A hierarchical NiO/NiMn-layered double hydroxide nanosheet array on Ni foam for high performance supercapacitors. *Dalton Transactions*, *46*(23), 7388–7391. https://doi.org/10.1039/c7dt00932a.

[174] Gonçalves, J. M., da Silva, M. I., Toma, H. E., Angnes, L., Martins, P. R., & Araki, K. (2020). Trimetallic oxides/hydroxides as hybrid supercapacitor electrode materials: a review. *Journal of Materials Chemistry A*, *8*(21), 10534–10570. https://doi.org/10.1039/d0ta02939d.

[175] Chen, Y. S., Dominko, R., Marczewski, M., & Wieczorek, W. (2024). Optimizing high-energy lithium-ion batteries: a review of single crystalline and polycrystalline nickel-rich layered cathode materials: performance, synthesis and modification. *Applied Physics A: Materials Science and Processing*, *130*(10). https://doi.org/10.1007/s00339-024-07897-7.

[176] Wu, Q., He, T., Zhang, Y., Zhang, J., Wang, Z., Liu, Y., Zhao, L., Wu, Y., & Ran, F. (2021). Cyclic stability of supercapacitors: materials, energy storage mechanism, test methods, and device. *Journal of Materials Chemistry A*, *9*(43), 24094–24147. https://doi.org/10.1039/d1ta06815f.